Ultra-Fast Multi-Organ Proteomics Unveils Tissue-Specific Mechanisms of Drug Efficacy and Toxicity

Yun Xiong[1,2,3,#], Lin Tan[1,2,3,#], Wai-kin Chan[1,3,#], Eric S. Yin[1,3], Sri Ramya Donepudi[1,4], Jibin Ding[1,2,3], Bo Wei[1,3], Bao Tran[1,3], Sara Martinez[1,3], Iqbal Mahmud[1,3], Hamish I. Stewart[5], Daniel J. Hermanson[5], John N. Weinstein[1,2,3], Philip L. Lorenzi[1,2,3,*]

Affiliations

[1]Department of Bioinformatics and Computational Biology, The University of Texas MD Anderson Cancer Center (MDACC), Houston, TX 77030, USA

[2]Proteomics Core Facility, Department of Bioinformatics and Computational Biology, The University of Texas MD Anderson Cancer Center (MDACC), Houston, TX 77030, USA

[3]Metabolomics Core Facility, Department of Bioinformatics and Computational Biology, The University of Texas MD Anderson Cancer Center (MDACC), Houston, TX 77030, USA

[4]University of Pittsburgh, Department of Pharmacology and Chemical Biology

[5]Thermo Fisher Scientific GmbH, Bremen, 28199, Germany

[#]These authors contributed equally to this work.

*Lead contact and corresponding author. Please address correspondence to PLLorenzi@mdanderson.org

Abstract

Rapid and comprehensive analysis of complex proteomes across large sample sets is vital for unlocking the potential of systems biology. We present UFP-MS, an ultra-fast mass spectrometry (MS) proteomics method that integrates narrow-window data-independent acquisition (nDIA) with short-gradient micro-flow chromatography, enabling profiling of >240 samples per day. This optimized MS approach identifies 6,201 and 7,466 human proteins with 1- and 2-min gradients, respectively. Our streamlined sample preparation workflow features high-throughput homogenization, adaptive focused acoustics (AFA)-assisted proteolysis, and Evotip-accelerated desalting, allowing for the processing of up to 96 tissue samples in 5 h. As a practical application, we analyzed 507 samples from 13 mouse tissues treated with the enzyme-drug L-asparaginase (ASNase) or its glutaminase-free Q59L mutant, generating a quantitative profile of 11,472 proteins following drug treatment. The MS results confirmed the impact of ASNase on amino acid metabolism in solid tissues. Further analysis revealed broad suppression of anticoagulants and cholesterol metabolism and uncovered numerous tissue-specific dysregulated pathways. In summary, the UFP-MS method greatly accelerates the generation of biological insights and clinically actionable hypotheses into tissue-specific vulnerabilities targeted by ASNase.

Introduction

The past decade witnessed remarkable technological and scientific strides that paved the way for advances in systems biology(*1, 2*). Innovations in genome sequencing have enabled the generation of large molecular datasets spanning a range of biological systems and matrices, from cells to tissues to biological fluids(*3, 4*). Concurrently, mass spectrometry (MS)-based proteomics has emerged as an essential tool for high-throughput protein-level measurements, becoming indispensable for functional genomics and systems biology(*5-7*).

MS-based proteomics studies can typically be divided into three major steps: sample preparation, MS data acquisition, and data analysis. Whereas data analysis tools have improved significantly in recent years(*8-12*), sample pretreatment and MS-based data acquisition remain limiting steps in proteomics investigation. A variety of sample preparation workflows have been developed for proteomic studies with specific sample types and experimental goals(*13, 14*). However, most workflows are limited in the number of samples that can be processed simultaneously, precluding their application to larger systems biology studies. For MS data acquisition, proteome coverage is a critical challenge due to the wide dynamic range of protein expression levels in cells, ranging from tens to over a million copies per cell. The most common approach to address that complexity has been multi-shot proteomics with offline peptide fractionation(*15-17*), but this approach necessitates extensive instrument time and large sample volumes. Prompted by those limitations, ongoing effort has been allocated to the development of improved single-shot strategies. Recently, narrow-window DIA (nDIA) was reported to achieve the identification of ~10,000 proteins within 1 h, and ~7,000 proteins in a 5-min gradient on the Orbitrap Astral MS(*18*).

Here, building on recent advances with nDIA, we introduce a workflow that combines an optimized nDIA-MS method with high-throughput sample preparation to facilitate rapid and in-depth proteome profiling. The method employs 1-Th quadrupole isolation windows and achieves identification of 6,201 and 7,466 proteins with 1- and 2-min LC gradients, respectively. Our streamlined sample preparation incorporates high-throughput tissue homogenization, adaptive focused acoustics (AFA)-assisted proteolysis, and Evotip-accelerated desalting, enabling the processing of up to 96 tissue samples within 5 h. To demonstrate the utility of our approach, we conducted a systems proteomics analysis of 507 biological samples across 13 tissue types to examine the systems pharmacology of L-Asparaginase (ASNase). The results provided a quantitative landscape of 11,472 proteins, uncovering distinct tissue-specific responses that shed new light on mechanisms of ASNase sensitivity, resistance, and toxicity.

Results

Identification of 6,201 proteins per minute with UFP-MS

The Orbitrap Astral MS system combines a modified Orbitrap Exploris 480 MS with the asymmetric track lossless (Astral) analyzer(*19*) (Fig. 1a). The Astral analyzer supports parallel MS2 scanning and achieves MS acquisition rates of up to 200 Hz, making it well suited for ultra-high-throughput proteomics analysis(*20, 21*).

As a benchmark for ultra-high-throughput analysis, the Evosep One system (Evosep, #AN-024A-500SPD) coupled with a timsTOF Pro 2 identifies 2,500 proteins with a 2.2-min LC gradient, achieving a protein identification rate of over 1,000 proteins per min (Supplementary Fig. 1). Based on that, we first coupled an Evosep One system with an Orbitrap Astral MS (Fig. 1b). Using a similar LC gradient and nDIA MS method, we identified an average of 5,160 proteins and 34,173 peptides from 200 ng of HeLa digest (Fig. 1c). To further improve proteome coverage, we modified the LC system by transferring the Evosep endurance column (Evosep, #EV1107, 4 cm x 150 µm, 1.9 µm particle size) and stainless-steel emitter (Evosep, #EV1086, ID 30 µm) to a Vanquish Neo UHPLC system. This modification permitted greater LC gradient flexibility. With an optimized 2-min gradient, proteome coverage was improved to an average of 6,549 proteins and 54,306 peptides (Fig. 1c).

Thereafter, we evaluated various MS data acquisition parameters (Fig. 1b). Consistent with previous studies(*18*), decreasing MS2 maximum injection time (IT) from 3.5 ms to 2.5 ms improved peptide detection (Fig. 1d). Further decreases below 2 ms led to decreased identifications. We next investigated the impact of mass range (MR) on duty cycle, comparing mass ranges of 380-980, 400-800, and 495-745 Th with corresponding isolation windows (Fig. 1e). The 495-745 Th mass range with a 1 Th isolation window delivered optimal results at the protein level. Further exploration of isolation windows from 0.8 to 2.0 Th confirmed that a 1 Th isolation window yielded the highest number of protein identifications (Fig. 1f). Automatic gain control (AGC) target values ranging from 100 to 600 produced similar results, with an AGC of 500 marginally improving precursor ion detection (Fig. 1g). Based on the evaluations, we established a modified nDIA method with an injection time of 2.5 ms, mass range of 495-745, 1 Th isolation window, and an AGC value of 500.

We next assessed the performance across LC gradients from 1 to 5 min. Notably, even with a 1-min gradient, we still identified ~6,201 human proteins from 1 ug HeLa digest, albeit with a decrease in peptide number (Fig. 1h). A 2-min gradient yielded 7,466 proteins and 59,919 peptides. Proteome coverage remained at nearly 8,000 proteins with gradients from 3 to 5 min. The protein identification rate of up to 6,201 proteins per min greatly exceeds that of previous reports(*22-24*) (Supplementary Fig. 1a, b).

To evaluate the quantitative performance of the new method, we analyzed proteome samples from three species (human, yeast, and *Escherichia coli*) mixed in various ratios. Overall, an average of 9,434 proteins were identified in each mixed sample (Fig. 1i). Quantitative analysis demonstrated accurate protein quantitation across six different ratios (1:9, 1:4, 2:3, 3:2, 4:1, and 9:1) (Fig. 1j). By comparing the different mixtures, we found that the total MS intensities of yeast and *Escherichia coli peptides* increase linearly with respect to sample input (Fig. 1k).

High-throughput sample preparation accelerates large-scale tissue proteomics

To address the next rate-limiting step, sample preparation, we developed a rapid workflow integrating high-throughput tissue homogenization, adaptive focused acoustic (AFA)-

accelerated proteolysis, and Evotip desalting (Fig. 2a). The Precellys Evolution tissue homogenizer performs bead-based protein extraction for up to 24 samples simultaneously, achieving thorough homogenization in less than 1 min. Protein digestion is accelerated using a Covaris R230 Focused-Ultrasonicator, which can handle 96 samples concurrently. Peptide desalting with racked Evotips enabled simultaneous cleaning of up to 96 peptide samples in 30 min.

We next compared proteolytic digestion performance with and without sonication across durations from 30 min to 15 h (Fig. 2b-d). MS results showed that 4-h digestion with AFA-assisted sonication provided the highest number of peptides and proteins, although minor differences were observed across conditions (Fig. 2b, c). Over 90% of peptides had only one or no missed cleavage sites across all conditions (Fig. 2d), with AFA-assisted digestion exhibiting slightly better performance in all scenarios. We ultimately chose 4-h digestion to maximize protein recovery, which translates to a total of ~5 h to process 96 samples (Fig. 2a).

We next analyzed three mouse tissues (brain, kidney, and lung) to compare the output obtained from a standard workflow and the optimized high-throughput workflow (Fig. 2e, Supplementary Fig. 1c). The high-throughput method identified an average of 6,976, 5,665, and 6,355 proteins from brain, kidney, and lung, respectively, which was comparable to the results from the standard workflow. Pairwise comparisons of protein abundance ratios between two tissues at a time demonstrated Pearson correlation coefficients consistently exceeding 0.83 (Fig. 2f-h), indicating comparable quantitative performance between the two methods.

We next estimated the sample preparation time required to process 507 tissue samples (Fig. 2i, j). The standard workflow requires 369 work hours, equivalent to 46.1 x 8-h workdays. The high-throughput workflow, however, needs only 46.9 work hours (5.9 workdays), providing more than seven times higher throughput for large-scale studies.

Multi-organ quantitative profiling of 11,472 proteins following ASNase treatment

L-Asparaginase (ASNase) is a critical component of the standard of care for pediatric acute lymphoblastic leukemia (ALL). However, its application to adult leukemias and solid tumors is hindered by significant side effects and drug resistance(*25*). ASNase toxicity is attributed in part to its glutaminase co-activity(*25*). There has been interest in engineering glutaminase-free variants that decrease side effects while maintaining efficacy(*26*). We previously demonstrated the anticancer activity of the glutaminase-free Q59L mutant ($ASNase^{Q59L}$) against ASNS-negative cell lines(*27-29*), but those findings failed to translate to a preclinical mouse model(*28*), suggesting that ASNase glutaminase activity is necessary for its anticancer efficacy (Fig. 3a). To aid in the development of new ASNase-based therapeutic strategies, it is essential to gain a systems-level understanding of the mechanisms through which ASNase mediates anticancer activity and toxicity.

To that end, we applied the optimized method to analyze tissue samples from NSG mice treated with PBS (vehicle control), 20,000 U/kg $ASNase^{WT}$ (Spectrila®), or 20,000 U/kg $ASNase^{Q59L}$ for 0, 1, 3, 5, and 8 d (Fig. 3b). At each time point, mice were euthanized, and 13 tissues were collected, including subcutaneous white adipose tissue (SQWAT), gonadal adipose tissue (GAT), lung, spleen, stomach, small and large intestine, liver, kidney, heart, leg muscle, brain, and bone marrow (Fig. 3c). Analysis of a total of 507 collected tissue samples yielded 11,472 proteins and 104,784 peptides across all samples (Fig 3d, Supplementary Fig. 1d). The highest numbers of proteins and peptides were observed in the brain, followed by the large intestine, stomach, lung, spleen, GAT, bone marrow, and SQWAT. The lowest identifications were found in leg muscle and heart. As anticipated, the correlation matrix displayed strong associations

between the two fat depots, SQWAT and GAT (Fig. 3e). Lung protein expression correlated strongly with that of spleen, bone marrow, and kidney. Large intestine protein expression was more strongly correlated with that of stomach than with small intestine (Fig. 3e). Unsupervised clustering using t-SNE confirmed the similarity of stomach and large intestine (Fig. 3f). We then used heatmaps to illustrate the quantitative overview of protein expression following ASNase treatment in each tissue (Fig. 3g). In most organs, we observed significant differences in protein expression between ASNase^{WT} and PBS treatments, whereas ASNase^{Q59L} yielded only minor differences compared to PBS (Fig. 3g). For example, we saw notable changes in the spleen, but ASNase^{Q59L} also induced unique changes in the bone marrow, kidney, and GAT. These results suggest organ-specific drug effects. We next mined these data to generate new insights into the mechanisms of ASNase efficacy and toxicity across different tissues.

Amino acid metabolodynamics in whole blood confirm the efficacy of ASNase

To confirm the efficacy of ASNase^{WT}, we measured the levels of asparagine (ASN) and aspartic acid (ASP) in whole blood samples (Fig. 4a). Consistent with our previous results(*28, 29*), ASN reached a trough level after one day of treatment with ASNase^{WT} and remained at trough level throughout the 8-day time course, while ASP levels were essentially unaffected (Fig. 4b, c). In contrast, treatment with ASNase^{Q59L} yielded only partial and transient depletion of ASN followed by rapid restoration, suggesting that the body mounted resistance by up-regulating production of ASN.

Our previous studies observed that ASNase^{WT} and ASNase^{Q59L} had subtly different effects on glutamine (GLN) and glutamic acid (GLU) levels in a 24-h time course(*28, 29*). In this study, the extended 8-d time course revealed significant increases of both GLN and GLU levels following ASNase^{WT} but not ASNase^{Q59L} treatment (Fig. 4d, e), consistent with the reported up-regulation of glutamine synthetase (GLUL) and glutaminases (GLS, GLS2) following ASNase^{WT} treatment *in vitro(30, 31)*. These data confirm the *in vivo* efficacy of ASNase^{WT} and highlight key differences between ASNase^{WT} and ASNase^{Q59L}.

Organ-specific resistance and vulnerability to ASNase

To assess the system-wide pharmacodynamic and metabolodynamic effects of ASNase in solid tissues, we monitored ASN, ASP, GLN, and GLU levels across six tissues: SQWAT, lung, spleen, liver, brain, and bone marrow (Fig. 4f). Consistent with observations in blood, ASNase^{WT} treatment resulted in a sustained depletion of ASN in all six tissues, whereas ASNase^{Q59L} initially decreased ASN levels but subsequently up-regulated ASN at these sites (Fig. 4f). We did not observe significant changes in ASP, GLN, or GLU levels after drug treatment in most tissues, except in the liver, where ASNase^{WT} induced increases in all three amino acids after prolonged treatment. Notably, we observed a decrease in ASP levels in the spleen following ASNase^{WT} but not ASNase^{Q59L} treatment. These findings contrast with the observed blood effects, highlighting spleen-specific suppression of ASP metabolism as a targeted vulnerability of ASNase^{WT} treatment.

Asparagine synthetase (ASNS) is a well-established mediator of resistance to ASNase(*25, 27, 28, 32, 33*). However, multiple reports have also described ASNS-low cancer cells exhibiting resistance to ASNase *in vivo(28, 34, 35)*. In assessing ASNS expression levels we observed rapid and extensive up-regulation in the lung, small intestine, large intestine, liver, and kidney following both ASNase^{WT} and ASNase^{Q59L} treatments (Fig. 4g), suggesting that broad ASNS up-regulation could potentially explain the resistance of low-ASNS tumors to ASNase treatment. In

contrast, both ASNase variants suppressed ASNS up-regulation in brain, bone marrow, heart, and muscle. Strikingly, only spleen exhibited down-regulation of ASNS following ASNase^{WT} but not ASNase^{Q59L} treatment. The spleen, a vital organ in the immune system, filters and stores blood and produces white blood cells that protect the body from infection. Given the association of the spleen with blood cells, our findings prompt the hypothesis that spleen-specific suppression of ASNS is a feature of the ASNase mechanism of action against ALL. If future experiments confirm that to be true, combination therapy with an ASNS inhibitor could present a path for extending ASNase treatment to solid tumors.

In addition to ASNS, we examined the effects of ASNase on the broad network of proteins associated with ASN, ASP, GLN, and GLU metabolism (Supplementary Fig. 2a, b). Many of the observed changes suggested adaptive responses to ASNase^{WT}. Specifically, we observed up-regulation of: GLUL in spleen, stomach, small intestine, kidney, and heart; GLS in SQWAT, lung, spleen, stomach, small intestine, and kidney; GLUD1 in spleen, stomach, and bone marrow; at least one transaminase (GOT1, GOT2, GPT, GPT2) in all 13 tissues; at least one glutamine transporter (SLC1A5, SLC38A3) in stomach, and liver; and at least one glutathione metabolism component (GCLC, GCLM) in SQWAT, GAT, small intestine, large intestine, brain, and bone marrow. Up-regulation of those glutamine metabolism sub-pathways at the indicated organ sites suggests adaptive resistance mechanisms (i.e., compensatory mechanisms to maintain levels of the four amino acids during nutrient stress).

Nevertheless, five organs exhibited down-regulation of glutamine metabolism in response to ASNase^{WT} treatment (Supplementary Figure 2a, b). SQWAT exhibited down-regulation of CPQ, FOLH1, GOT1, GOT2, and SLC25A22. Spleen exhibited down-regulation of ALDH18A1, CAD, CTPS1, DARS2, GCLM, GMPS, PAICS, PFAS, PPAT, and SLC1A5. Liver exhibited down-regulation of ABAT, CPQ, GGCX, GLS, GLS2, GLUL, GOT2, and NADSYN1. Kidney exhibited down-regulation of ACY1, ACY3, BCAT1, CAD, CTPS1, GATB, GCLC, GPT, and SLC25A22. And muscle exhibited down-regulation of ABAT, ASNS, ASPA, ASS1, BCAT2, CAD, CPQ, DARS2, GCLC, GCLM, GLS, GLUD1, GMPS, GOT1, GOT2, GPT, NARS2, OPLAH, PAICS, PFAS, SLC1A5, and SLC25A22.

Overall, these analyses indicate that most organ sites mount an adaptive response to ASNase^{WT}. Nevertheless, potentially vulnerable organs include spleen, SQWAT, liver, kidney, and muscle (Fig. 4g). Among those, spleen uniquely exhibited suppression of ASNS protein (Fig. 4g). No clinical toxicities of ASNase have been associated specifically with spleen, muscle, or kidney, suggesting that using ASNase to treat tumors arising from or supported by those tissues may be safe. Liver and SQWAT were vulnerable organs that have been linked to clinical toxicities.

System-wide suppression of anticoagulants and cholesterol metabolism as likely drivers of ASNase toxicity

To explore other coordinated stress responses following drug treatment across tissues, we next compared protein expression profiles between ASNase-treated and PBS-treated samples at the pathway level. Proteins with an average fold change in expression greater than 2 or less than 0.5 and a p-value < 0.05 were classified as differentially modulated (Fig. 5a-d, Supplementary Fig. 3-15). ASNase^{WT} treatment significantly modulated (positively or negatively) the vast majority of proteins in liver and spleen (Fig. 5a, b). ASNase^{Q59L} treatment mainly up-regulated proteins in the liver, GAT, and small intestine, while down-regulating proteins in kidney, bone marrow, stomach, liver, and brain (Fig. 5c, d).

KEGG pathway enrichment analysis provided several notable insights (Supplementary Fig. 8-12). First, the suppressive effects of ASNase^{WT} were highly consistent across organ sites, with pathways such as "complement and coagulation cascades," cholesterol metabolism, and coronavirus disease being nearly uniformly downregulated in all tissues (Fig. 5e). No pathways were uniformly up-regulated across all tissues (Fig. 5e), indicating that the up-regulated pathways are highly tissue-specific. Similarly, ASNase^{Q59L} also did not uniformly modulate any pathways across organ sites (Fig. 5f).

Closer inspection of the MS proteomic data confirmed that most identified proteins in the complement and coagulation cascade and cholesterol metabolism pathways were down-regulated across all 13 tissue types following ASNase^{WT} but not ASNase^{Q59L} treatment (Fig. 6a). Focusing on proteins that were consistently dysregulated across multiple tissues, 28 proteins were commonly up-regulated, and 68 proteins were commonly down-regulated across at least three tissues following ASNase^{WT} treatment (Fig. 6b, c). ASNase^{Q59L} treatment up- or down-regulated 56 and 24 shared proteins, respectively (Fig. 6d, e). Around 50% of all proteins commonly down-regulated by ASNase^{WT} were involved in cholesterol metabolism or the complement and coagulation cascades (Fig. 6f-h). Together, these results suggested that well-known ASNase toxicities—hypertriglyceridemia and venous thromboembolism (VTE)—result from system-wide down-regulation of cholesterol metabolism and the complement and coagulation pathways.

ASNase^{WT} modulation of metabolites and proteins converge on inhibition of DNA replication and activation of ferroptosis in spleen

Although down-regulation of cholesterol metabolism and the complement and coagulation pathways was observed in nearly all tissues tested, this was not the case in the spleen (Fig. 5e). As noted previously, spleen uniquely exhibited decreased ASP levels (Fig. 4f) and decreased ASNS protein levels following ASNase^{WT} treatment (Fig. 4g). Considering the strong association between spleen and blood cells, we next analyzed the quantitative MS proteome profiles of the spleen following drug treatment. We compared PBS- and ASNase^{WT}-treated spleen proteomes and subjected differentially modulated proteins with a p-value < 0.05 and fold change > 2 or < 0.5 to functional clustering against the KEGG pathways database (Fig. 6a-c)(*36*). Since no dysregulated pathways were enriched prior to 3 d of treatment, we focused on effects at 3, 5, and 8 d. Notably, proteins associated with the "lysosome" pathway were significantly up-regulated at all time points, and DNA replication was significantly down-regulated at all time points (Fig.7a-c). At 8 d, "glutathione metabolism" and "ferroptosis" were significantly up-regulated (Fig. 7c). ASNase^{Q59L} did not affect those pathways (Supplementary Fig. 5).

Consistent with previous reports of ASNase-induced autophagy (a lysosome-driven process)(*37*), our data showed up-regulation of: i) lysosomal cysteine proteases CTSA, CTSB, CTSD, CTSF, and CTSZ; ii) lysosomal glycosidases GLA, GLB1, GNS, GUSB, HEXB, and NAGA; and iii) lysosomal phosphatases ACP2 and ACP5 following treatment of ASNase^{WT} (Fig. 7d). ASNase^{Q59L} did not significantly modulate lysosomal proteins. The induction of lysosomal proteins may be a consequence of decreased ASP and ASN, since lysosome-driven autophagy plays an important role in producing amino acids via recycling of proteins(*38*).

Prolonged ASNase^{WT} treatment also up-regulated glutathione (GSH) metabolism and ferroptosis (Fig.7c). In parallel, our metabolomic data revealed that GSH was decreased by ASNase^{WT} and significantly increased by ASNase^{Q59L} in the spleen (Fig. 7e). Most up-regulated GSH metabolism proteins were catalytic enzymes (Fig. 7d), including glutathione peroxidase 3 (GPX3), glutathione hydrolase 5 heavy chain (GGT5), and glutathione transferases (GSTA3, GSTK1, and MGST1). Their up-regulation following ASNase^{WT} treatment was consistent with

305 the decrease of GSH level (Fig. 7e). Since GSH is a key reducing equivalent and negative
306 modulator of ferroptosis, its concurrent down-regulation with the up-regulation of ferroptosis was
307 mechanistically consistent(*39*). The up-regulated ferroptosis pathway encompassed four
308 proteins including CYBB, FTH1, FTL1, and HMOX1 (Fig. 7d). We also observed down-
309 regulation of porphyrin metabolism following ASNase^{WT} for 3 and 8 days (Fig. 7a, c), prompting
310 the hypothesis that down-regulation of porphyrin metabolism permits accumulation of free iron,
311 which is required for ferroptosis (Fig.7c).

312 A number of DNA replication proteins were down-regulated by ASNase^{WT} treatment (Fig. 7a-d):
313 a) DNA polymerases POLA1, POLA2, POLD1, POLD3, and POLE; b) components of the
314 MCM2-7 complex MCM2, MCM3, MCM4, MCM5, MCM6, and MCM7; c) DNA primases PRIM1
315 and PRIM2; d) ribonuclease H2 subunits RNASEH2A and RNASEH2B; and e) other DNA
316 replication-associated proteins PCNA, RPA1/3, RFC2/5, FEN1, and LIG1 (Fig. 7d). Down-
317 regulation of DNA replication may be associated with the decrease of ASP (Fig. 4f), which
318 contributes to *de novo* synthesis of purine and pyrimidine nucleotides(*40*). Interestingly, of all
319 amino acids in spleen following ASNase treatment, only ASP and ASN were clearly down-
320 regulated (Fig. 7f, Supplementary Fig. 16). Correspondingly, metabolomics indicated significant
321 decrease of several deoxyribonucleotides, including dTDP, dUMP, dTMP, dCDP, dCTP, and
322 dGTP (Fig.7g), further supporting the observed down-regulation of nucleotide synthesis at the
323 protein and pathway levels.

324 Spleen-specific down-regulation of ASNS may be associated with up-regulation of
325 aminopeptidases LAP3 and ANPEP (Fig. 7d) and down-regulation of ribosome and translation
326 pathways (Fig. 7a, b, d, Supplementary Fig 17a, b). A number of mitochondrial proteins that
327 were specifically down-regulated in spleen (Fig. 7d, Supplementary Fig.17a, b), which is
328 consistent with previous reports that mitochondrial electron transport chain enables synthesis of
329 ASP(*41*). To note, in addition to the deoxyribonucleotides that described above, adenosine
330 triphosphate (ATP) was also decreased in spleen following ASNase^{WT} treatment
331 (Supplementary Fig 17c).

332 Collectively, integrated analysis of proteomic and metabolomic data implicates the spleen as a
333 highly vulnerable target of ASNase^{WT}. That vulnerability is potentially explained by signaling
334 cascades that modulate amino acid metabolism, energy metabolism, redox metabolism, and
335 global protein synthesis converging on inhibition of DNA replication and induction of cell death
336 (ferroptosis) (Fig. 7h), suggesting a plausible mechanism supported by our findings: 1)
337 ASNase^{WT} decreases ASN and ASP in spleen (Fig. 7f); 2) endoplasmic reticulum stress and
338 protein misfolding are up-regulated(*42, 43*)); 3) lysosomal enzymes are activated (Fig. 7d); 4)
339 reactive oxygen species (ROS) accumulate; 5) GSH is consumed (Fig. 7d, e); 6) damaged
340 mitochondria accumulate; 7) mitophagy clears damaged mitochondria (Fig. 7d) and further
341 decreases ASP production and nucleotide synthesis (Fig. 7f, g) and ATP levels (Supplementary
342 Fig 17c); 8) DNA replication is suppressed (Fig. 7a-d); 9) recycling of damaged RBCs together
343 with suppression of porphyrin synthesis leads to accumulation of free iron (Fig. 7a, c); and 10)
344 ferroptosis is activated (Fig. 7c, d). The observed decrease of ASNS expression is likely due to
345 the combined impairment of protein synthesis (Fig. 7d), decrease of ASP (substrate of ASNS)
346 availability (Fig. 7f), and increased lysosomal degradation (Fig. 7d).

347

348 ***ASNase dysregulates system-wide and tissue-specific pathways***

349 In addition to findings in spleen, our analysis revealed numerous tissue-specific dysregulated
350 pathways in other tissues following ASNase treatment. These observations offer further insights
351 into the effects of ASNase^{WT} at the system-wide and tissue-specific levels. Those results are
352 discussed in the Supplementary Information.

Discussion

MS-based proteomics has become an essential tool for high-throughput investigation of cellular proteins. While RNA sequencing technologies are adept at quantifying gene expression levels, the direct analysis of proteins—the principal executors of cellular functions—remains indispensable in biological research.

To improve upon the latest advances of ultra-high-throughput LC (Evosep, #AN-024A-500SPD) and MS (nDIA on Orbitrap Astral MS(*44*)) technologies, we present a novel LC-MS approach that integrates optimized nDIA with short-gradient micro-flow chromatography, yielding identification of 6,201 and 7,466 proteins with 1- or 2-min LC gradients, respectively. The achieved protein identification rate of up to 6,201 proteins per min represents more than a two-fold improvement over previously reported cutting-edge methods (Supplementary Fig. 1a, b)(*18, 22-24, 45*).

Sample preparation also represents a critical rate-limiting step for large-scale proteomics experiments. To address this, we designed a rapid tissue proteomics workflow capable of processing up to 96 tissue samples within 5 h, including a 4 h proteolysis step. We used the workflow to obtain more than seven-fold increased throughput (Fig. 2i) in a multi-organ systems proteomics project involving 507 tissue samples (Fig. 2i). Decreasing the protein digestion time to 30 min increases overall processing speed to 96 samples per hour but results in a marginal decrease (2.2%) in protein identification (Supplementary Table 8). Our chosen application was tissue proteomics, but the workflow can be adapted to other biological matrices.

We chose the systems pharmacology of ASNase as an application primarily because its toxicity has prevented application to adult patients and cancers beyond pediatric ALL(*25*). Additionally, despite >50 years of research, the effects of its glutaminase activity and the mechanistic underpinnings of ASNase sensitivity and resistance are poorly understood.

The quantitative profile of 11,472 proteins provides a detailed multi-organ roadmap of dysregulated cellular pathways following ASNase treatment. New insights regarding ASNase toxicities included the association of VTE with suppression of the complement and coagulation system, and association of hypertriglyceridemia with widespread suppression of cholesterol metabolism.

The complement and coagulation pathways are crucial for host defense against pathogen infection and injury, involving blood-based defense systems that are proteolytically activated to produce active molecules crucial for immunity and clotting(*46*). Genes associated with the coronavirus disease pathway also include complement factors and immune response elements. Within the 44 down-regulated proteins associated with the complement and coagulation cascades, 11 have anti-coagulant function (CPB2, KNG1, KNG2, PLG, PROC, SERPINA1B, SERPINA1D, SERPINC1, SERPIND1, SERPINF2, SPERING1), and the remaining 33 have pro-coagulant function. Most of the 11 anti-coagulant proteins were down-regulated in up to 9 of the 13 tissue types (Fig. 6a). Similarly, previous research on the VTE side effects of ASNase identified down-regulation of plasminogen (PLG), antithrombin III (SERPINC1), and fibrinogen (FGA, FGB, FGG) (*47, 48*). SERPINC1 is of primary interest in current clinical practice; guidance recommends weekly monitoring of SERPINC1 levels in patients and administration of recombinant SERPINC1 when levels fall below 60% with a repletion target of 80% to 120%(*49*). Our findings reveal that SERPINC1 was widely down-regulated in most of the 13 tissues (Fig. 6a) and exhibited a significant decrease in three specific tissues including stomach, liver, and kidney (Fig. 6h). Additionally, PLG, SERPINA1B (human homolog SERPINA1), SERPINA1D (human homolog SERPINA1), and SERPIND1 were even more significantly down-regulated than SERPINC1 (Fig. 6g), representing potentially more impactful targets for mitigating ASNase-induced VTE. Although no recombinant variants of PLG or SERPIND1 exist yet,

401 INBRX-101, a recombinant Fc fusion protein of SERPINA1 (alpha-1 antitrypsin) is entering
402 Phase 2/3 testing(*50*). Given that only 60% of patients with VTE respond to SERPINC1
403 repletion, our results provide a rationale for testing INBRX-101 for further mitigation of ASNase-
404 induced VTE. All in all, our data confirm previous findings and identify additional changes in
405 complement and coagulation cascade proteins following ASNase treatment, further linking the
406 down-regulation of these pathways to VTE.

407 Within the 17 down-regulated proteins in the cholesterol metabolism pathway, 6 (APOA1,
408 APOA2, APOA4, APOC2, LCAT, and SORT1) are negative modulators of triglyceride levels,
409 and their down-regulation potentially explains ASNase-induced hypertriglyceridemia(*51, 52*). It
410 has been hypothesized that ASNase-induced hypertriglyceridemia, which occurs in up to 50% of
411 patients, is the result of very low-density lipoprotein (VLDL) up-regulation(*53, 54*). That
412 hypothesis is not sufficiently granular, though, because VLDL components can be positive or
413 negative modulators of triglyceride levels based on whether they facilitate secretion or uptake of
414 triglycerides. Considering VLDL components as a whole, our data revealed prominent down-
415 regulation of APOA4, APOC1, APOC2, APOE, and APOH in SQWAT, lung, liver, large intestine,
416 and heart tissues (Fig. 5e, Fig. 6a, c, h). All of those except APOE are negative modulators of
417 triglyceride levels; their down-regulation could potentially explain ASNase-induced
418 hypertriglyceridemia. In four tissues we also observed a notable increase in adiponectin
419 (ADIPOQ), which promotes the catabolism of VLDL triglycerides and may explain the observed
420 down-regulation of VLDL apolipoproteins (Fig. 6b)(*55*). Together, these findings support the
421 following mechanistic hypothesis to explain ASNase-induced hypertriglyceridemia: i) nutrient
422 stress triggers lipogenic processes culminating in triglyceride synthesis; ii) ASNase suppresses
423 the capacity of organs (primarily the liver) to assemble triglyceride-VLDL complexes, and/or
424 ASNase-induced ADIPOQ rapidly catabolizes such complexes before they can be exported;
425 and iii) free triglycerides are secreted into systemic circulation without a mechanism to distribute
426 them into tissues (mainly fat), leading to triglyceride accumulation in the blood.

427 In considering therapeutic strategies to mitigate ASNase-induced hypertriglyceridemia, our
428 results identify ADIPOQ as one potential target, but no inhibitors are currently available.
429 Additional candidate targets include the two known positive modulators of triglyceride levels—
430 APOC3 and APOE. Indeed, our data indicates that APOC3 was maintained near baseline levels
431 or elevated in SQWAT, spleen, stomach, large intestine, kidney, muscle, brain, and bone
432 marrow (Fig. 6a). APOC3 was recently identified as a target for lowering triglycerides by up to
433 77% using the antisense inhibitor volanesorsen(*56*). APOE, as noted previously, was down-
434 regulated in most tissues, but it was strikingly up-regulated in the small intestine by ASNase.
435 Since APOE-targeted drugs (pioglitazone, rosiglitazone) are available, our findings provide a
436 rationale for testing these and volanesorsen for mitigation of ASNase-induced
437 hypertriglyceridemia.

438 New insights regarding ASNase efficacy suggested that the spleen and kidney may represent
439 targetable organ vulnerabilities. In response to $ASNase^{WT}$ treatment, spleen exhibited
440 suppression of ASNS, suppressed glutamine metabolism including ASP production, impaired
441 DNA replication, and induction of ferroptosis. Those observations prompt the hypothesis that
442 ASNase may be effective against a broad range of hematological-related malignancies.
443 Although kidney exhibited up-regulation of ASNS, it remains a potential target due to broad
444 suppression of glutamine metabolism induced by $ASNase^{WT}$ treatment. Future work will be
445 required to test the hypothesis that ASNase is effective for treating renal cancers.

446 New insights regarding ASNase resistance identified system-wide up-regulation of ASNS as a
447 key resistance factor, building upon the reported association between the tumor
448 microenvironment and ASNase resistance(*25, 57*). The observed up-regulation of liver protein
449 synthesis may also contribute to ASNase resistance. Importantly, our findings explain how low-

ASNS tumors can still be resistant to ASNase; if ASNase dosage is insufficient to maintain durable depletion of ASN, tumor proliferation can continue. Because virtually every organ throughout the body up-regulates ASNS to produce ASN following ASNase treatment, the battle between the drug and the body can only be won if ASN depletion is sustained. These findings highlight the critical need for new therapeutic drug monitoring protocols focused on ASN measurement in whole blood, rather than relying on methods that measure only enzyme activity levels.

The use of ASNS as a predictive biomarker of response to ASNase therapy presents complex considerations. Our findings indicate that ASNase suppresses ASNS up-regulation in selected tissue types, and tumors that exhibit that phenotype are likely to respond well to ASNase. However, because most tissue types exhibit significant up-regulation of ASNS in response to ASNase treatment, tumor-specific ASNS expression may play a relatively minor role in ASNase resistance. Until further clarity is achieved, efforts to extend ASNase therapy to new indications should continue to prioritize testing against tumors with low ASNS expression.

Finally, we hasten to emphasize that integrated analysis of amino acids—particularly ASN, ASP, GLU, and GLN—and their associated proteins proved to be particularly valuable for characterizing organ-level nutrient dependencies.(*58*)

In summary, ultra-fast, quantitative proteome profiling enabled deep analysis of the systems pharmacology of ASNase, facilitating the generation of novel insights into the enzyme-drug's efficacy and toxicity. This work highlights the transformative potential of nDIA-based ultra-fast proteomics and demonstrates its applicability to a broad range of life science investigations, including the systems biology of dietary interventions, exercise interventions, environmental factors, genetics, and beyond.

References

1. H. M. J. Werner, G. B. Mills, P. T. Ram, Cancer Systems Biology: a peek into the future of patient care? *Nature Reviews Clinical Oncology* **11**, 167-176 (2014).
2. B. M. Kuenzi, T. Ideker, A census of pathway maps in cancer systems biology. *Nat Rev Cancer* **20**, 233-246 (2020).
3. S. Goodwin, J. D. McPherson, W. R. McCombie, Coming of age: ten years of next-generation sequencing technologies. *Nat Rev Genet* **17**, 333-351 (2016).
4. J. Shendure, H. Ji, Next-generation DNA sequencing. *Nat Biotechnol* **26**, 1135-1145 (2008).
5. F. Meissner, J. Geddes-McAlister, M. Mann, M. Bantscheff, The emerging role of mass spectrometry-based proteomics in drug discovery. *Nat Rev Drug Discov* **21**, 637-654 (2022).
6. R. Aebersold, M. Mann, Mass-spectrometric exploration of proteome structure and function. *Nature* **537**, 347-355 (2016).
7. J. M. Bader, V. Albrecht, M. Mann, MS-Based Proteomics of Body Fluids: The End of the Beginning. *Mol Cell Proteomics* **22**, 100577 (2023).
8. V. Demichev, C. B. Messner, S. I. Vernardis, K. S. Lilley, M. Ralser, DIA-NN: neural networks and interference correction enable deep proteome coverage in high throughput. *Nature methods* **17**, 41-44 (2020).
9. M. Mann, C. Kumar, W. F. Zeng, M. T. Strauss, Artificial intelligence for proteomics and biomarker discovery. *Cell Syst* **12**, 759-770 (2021).
10. S. Gessulat *et al.*, Prosit: proteome-wide prediction of peptide tandem mass spectra by deep learning. *Nat Methods* **16**, 509-518 (2019).
11. A. Martinez-Val, D. B. Bekker-Jensen, A. Hogrebe, J. V. Olsen, Data Processing and Analysis for DIA-Based Phosphoproteomics Using Spectronaut. *Proteomics Data Analysis* **2361**, 95-107 (2021).
12. R. Lou *et al.*, Benchmarking commonly used software suites and analysis workflows for DIA proteomics and phosphoproteomics. *Nat Commun* **14**, 94 (2023).
13. A. Shevchenko, H. Tomas, J. Havlis, J. V. Olsen, M. Mann, In-gel digestion for mass spectrometric characterization of proteins and proteomes. *Nat Protoc* **1**, 2856-2860 (2006).
14. J. R. Wisniewski, A. Zougman, N. Nagaraj, M. Mann, Universal sample preparation method for proteome analysis. *Nat Methods* **6**, 359-362 (2009).
15. J. Adachi *et al.*, Improved Proteome and Phosphoproteome Analysis on a Cation Exchanger by a Combined Acid and Salt Gradient. *Anal Chem* **88**, 7899-7903 (2016).
16. Y. Wang *et al.*, Reversed-phase chromatography with multiple fraction concatenation strategy for proteome profiling of human MCF10A cells. *Proteomics* **11**, 2019-2026 (2011).
17. K. Horie *et al.*, Hydrophilic interaction chromatography using a meter-scale monolithic silica capillary column for proteomics LC-MS. *Anal Chem* **86**, 3817-3824 (2014).
18. U. H. Guzman *et al.*, Ultra-fast label-free quantification and comprehensive proteome coverage with narrow-window data-independent acquisition. *Nat Biotechnol*, (2024).
19. H. I. Stewart *et al.*, Parallelized Acquisition of Orbitrap and Astral Analyzers Enables High-Throughput Quantitative Analysis. *Anal Chem* **95**, 15656-15664 (2023).
20. L. R. Heil *et al.*, Evaluating the Performance of the Astral Mass Analyzer for Quantitative Proteomics Using Data-Independent Acquisition. *Journal of Proteome Research* **22**, 3290-3300 (2023).
21. L. R. Serrano *et al.*, The One Hour Human Proteome. *Mol Cell Proteomics* **23**, 100760 (2024).
22. C. B. Messner *et al.*, Ultra-fast proteomics with Scanning SWATH. *Nat Biotechnol* **39**, 846-854 (2021).

519 23. L. Szyrwiel, C. Gille, M. Mulleder, V. Demichev, M. Ralser, Fast proteomics with dia-PASEF and
520 analytical flow-rate chromatography. *Proteomics* **24**, e2300100 (2024).
521 24. M. Ishikawa *et al.*, Optimization of Ultrafast Proteomics Using an LC-Quadrupole-Orbitrap Mass
522 Spectrometer with Data-Independent Acquisition. *J Proteome Res* **21**, 2085-2093 (2022).
523 25. M. Van Trimpont *et al.*, Novel Insights on the Use of L-Asparaginase as an Efficient and Safe Anti-
524 Cancer Therapy. *Cancers* **14**, (2022).
525 26. H. A. Nguyen, Y. Su, A. Lavie, Design and Characterization of Erwinia Chrysanthemi L-
526 Asparaginase Variants with Diminished L-Glutaminase Activity. *J Biol Chem* **291**, 17664-17676
527 (2016).
528 27. W. K. Chan *et al.*, The glutaminase activity of L-asparaginase is not required for anticancer
529 activity against ASNS-negative cells. *Blood* **123**, 3596-3606 (2014).
530 28. W. K. Chan *et al.*, Glutaminase Activity of L-Asparaginase Contributes to Durable Preclinical
531 Activity against Acute Lymphoblastic Leukemia. *Mol Cancer Ther* **18**, 1587-1592 (2019).
532 29. T. D. Horvath *et al.*, Assessment of l-Asparaginase Pharmacodynamics in Mouse Models of
533 Cancer. *Metabolites* **9**, (2019).
534 30. J. Blachier *et al.*, L-asparaginase anti-tumor activity in pancreatic cancer is dependent on its
535 glutaminase activity and resistance is mediated by glutamine synthetase. *Experimental cell*
536 *research* **426**, 113568 (2023).
537 31. G. Pathria, S. Verma, J. Yin, D. A. Scott, Z. A. Ronai, MAPK signaling regulates c-MYC for
538 melanoma cell adaptation to asparagine restriction. *EMBO Rep* **22**, e51436 (2021).
539 32. P. L. Lorenzi *et al.*, Asparagine synthetase as a causal, predictive biomarker for L-asparaginase
540 activity in ovarian cancer cells. *Mol Cancer Ther* **5**, 2613-2623 (2006).
541 33. P. L. Lorenzi *et al.*, Asparagine synthetase is a predictive biomarker of L-asparaginase activity in
542 ovarian cancer cell lines. *Mol Cancer Ther* **7**, 3123-3128 (2008).
543 34. V. Apfel *et al.*, Therapeutic Assessment of Targeting ASNS Combined with l-Asparaginase
544 Treatment in Solid Tumors and Investigation of Resistance Mechanisms. *ACS Pharmacol Transl*
545 *Sci* **4**, 327-337 (2021).
546 35. M. Grima-Reyes *et al.*, Tumoral microenvironment prevents de novo asparagine biosynthesis in
547 B cell lymphoma, regardless of ASNS expression. *Sci Adv* **8**, eabn6491 (2022).
548 36. M. Kanehisa, S. Goto, KEGG: kyoto encyclopedia of genes and genomes. *Nucleic Acids Res* **28**,
549 27-30 (2000).
550 37. M. Yu *et al.*, L-asparaginase inhibits invasive and angiogenic activity and induces autophagy in
551 ovarian cancer. *J Cell Mol Med* **16**, 2369-2378 (2012).
552 38. R. Higuchi-Sanabria *et al.*, Lysosomal recycling of amino acids affects ER quality control. *Sci Adv* **6**,
553 eaaz9805 (2020).
554 39. S. J. Dixon, D. A. Pratt, Ferroptosis: A flexible constellation of related biochemical mechanisms.
555 *Mol Cell* **83**, 1030-1042 (2023).
556 40. L. B. Sullivan *et al.*, Supporting Aspartate Biosynthesis Is an Essential Function of Respiration in
557 Proliferating Cells. *Cell* **162**, 552-563 (2015).
558 41. K. Birsoy *et al.*, An Essential Role of the Mitochondrial Electron Transport Chain in Cell
559 Proliferation Is to Enable Aspartate Synthesis. *Cell* **162**, 540-551 (2015).
560 42. I. A. Nikonorova *et al.*, Obesity challenges the hepatoprotective function of the integrated stress
561 response to asparaginase exposure in mice. *J Biol Chem* **292**, 6786-6798 (2017).
562 43. M. Garcia-Montojo *et al.*, TDP-43 proteinopathy in ALS is triggered by loss of ASRGL1 and
563 associated with HML-2 expression. *Nat Commun* **15**, 4163 (2024).
564 44. U. H. Guzman *et al.*, Ultra-fast label-free quantification and comprehensive proteome coverage
565 with narrow-window data-independent acquisition. *Nat Biotechnol*, (2024).

566 45. C. B. Messner *et al.*, Ultra-fast proteomics with Scanning SWATH. *Nat Biotechnol* **39**, 846-854
567 (2021).
568 46. M. Heurich, G. McCluskey, Complement and coagulation crosstalk - Factor H in the spotlight.
569 *Immunobiology* **228**, (2023).
570 47. J. R. Priest, N. K. Ramsay, A. J. Bennett, W. Krivit, J. R. Edson, The effect of L-asparaginase on
571 antithrombin, plasminogen, and plasma coagulation during therapy for acute lymphoblastic
572 leukemia. *J Pediatr* **100**, 990-995 (1982).
573 48. G. Goyal, V. R. Bhatt, L-asparaginase and venous thromboembolism in acute lymphocytic
574 leukemia. *Future Oncol* **11**, 2459-2470 (2015).
575 49. J. I. Zwicker *et al.*, The prevention and management of asparaginase-related venous
576 thromboembolism in adults: Guidance from the SSC on Hemostasis and Malignancy of the ISTH.
577 *J Thromb Haemost* **18**, 278-284 (2020).
578 50. M. L. Brantly *et al.*, Recombinant Alpha-1 Antitrypsin-Fc Fusion Protein INBRX-101 in Adults With
579 Alpha-1 Antitrypsin Deficiency: A Phase 1 Study. *Chronic Obstr Pulm Dis* **11**, 282-292 (2024).
580 51. S. K. Parsons *et al.*, Asparaginase-associated lipid abnormalities in children with acute
581 lymphoblastic leukemia. *Blood* **89**, 1886-1895 (1997).
582 52. K. R. Juluri, C. Siu, R. D. Cassaday, Asparaginase in the Treatment of Acute Lymphoblastic
583 Leukemia in Adults: Current Evidence and Place in Therapy. *Blood Lymphat Cancer* **12**, 55-79
584 (2022).
585 53. S. K. Parsons *et al.*, Asparaginase-associated lipid abnormalities in children with acute
586 lymphoblastic leukemia. *Blood* **89**, 1886-1895 (1997).
587 54. K. Schmiegelow, C. U. Rank, W. Stock, E. Dworkin, I. van der Sluis, SOHO State of the Art Updates
588 and Next Questions: Management of Asparaginase Toxicity in Adolescents and Young Adults
589 with Acute Lymphoblastic Leukemia. *Clin Lymphoma Myeloma Leuk* **21**, 725-733 (2021).
590 55. L. Qiao, C. Zou, D. R. van der Westhuyzen, J. Shao, Adiponectin reduces plasma triglyceride by
591 increasing VLDL triglyceride catabolism. *Diabetes* **57**, 1824-1833 (2008).
592 56. E. Gagnon, B. J. Arsenault, Drug target Mendelian randomization supports apolipoprotein C3-
593 lowering for lipoprotein-lipid levels reductions and cardiovascular diseases prevention.
594 *Atherosclerosis* **391**, 117501 (2024).
595 57. M. Grima-Reyes *et al.*, Tumoral microenvironment prevents de novo asparagine biosynthesis in
596 B cell lymphoma, regardless of ASNS expression. *Sci Adv* **8**, (2022).
597 58. Y. A. Yoo *et al.*, Asparagine Dependency is a Targetable Metabolic Vulnerability in TP53-Altered
598 Castration-Resistant Prostate Cancer. *Cancer Res*, (2024).

599

Acknowledgments

We thank all members of MD Anderson Proteomics Core Facility and Metabolomics Core Facility for their help and constructive discussions.

Funding

This work was supported by NIH grant number 1S10OD012304-01, NIH/NCI grant number P30CA016672, and The University of Texas MD Anderson Cancer Center.

Author contributions

Y.X., W.K.C., and P.L.L. conceived the project. Y.X. performed all experiments with assistance from L.T., W.K.C., E.S.Y., S.R.D., J.D., B.W., B.T., S.M., I.M., H.I.S., and D.J.H. L.T., B.T., and S.M. conducted the metabolomics analysis. W.K.C., E.S.Y., and S.R.D. carried out the mouse experiments. Y.X. handled data analysis and figure preparation. Y.X. wrote the manuscript, while P.L.L. and J.N.W. revised it with input from all authors. P.L.L. and J.N.W. supervised the study.

Competing interests

The authors declare that they have no conflicts of interest.

Data and materials availability

All data are available in the main text or the supplementary materials. The mass spectrometry proteomics data have been deposited to the ProteomeXchange Consortium via the PRIDE partner repository with the dataset identifier PXD055919 and PXD055590.

Supplementary Materials

Supplementary Results

Supplementary Discussion

Online methods

Supplementary Figs. 1 to 19

Supplementary Tables 1 to 27

References (1-35)

Figure legends

Fig. 1 | Ultra-fast nDIA enables identification of 6,201 proteins with a one-minute LC gradient

a, Schematic overview of the Orbitrap Astral MS instrument. **b,** The optimization process of the nDIA method used in this study. **c,** Comparison of the number of identified protein groups and peptides using Evosep-Astral and Neo-Evosep-Astral methods. **d,** Comparison of the number of identified protein groups and peptides with indicated maximum injection time (IT) ranging from 1 ms to 3.5 ms. **e,** Comparison of the number of identified protein groups and peptides with different combinations of mass range (MR) and isolation window (IW). **f,** Comparison of the number of identified protein groups and peptides with MS2 IW ranging from 0.8 Th to 2.0 Th. **g,** Comparison of the number of identified protein groups and peptides with automatic gain control (AGC) value ranging from 100 to 600. **h,** Number of the identified protein groups and peptides using the refined nDIA method with 1- to 5-min LC gradients. **i,** Protein groups identified from mixed samples containing protein digests from *E. coli* (E), human (H), or yeast (Y) in various ratios (E5H50Y45, E10H50Y40, E20H50Y30, E30H50Y20, E40H50Y10 and E45H50Y5). **j,** Peptide Ion intensity as a function of ratio for all runs in (**i**). Dashed lines represent expected log2(A/B) values for proteins from humans (green), yeast (purple) and *E. coli* (orange). FC_9, FC_4, and FC_1.5 are calculated from log2(E45H50Y5/E5H50Y45), log2(E40H50Y10/E10H50Y40), and log2(E30H50Y20/E20H50Y30), respectively. **k,** Correlation between MS intensity and peptide input for *E. coli* and yeast from runs performed in (**i**).

Fig. 2 | High-throughput sample preparation accelerates large-scale tissue proteomics

a, Workflows for standard and high-throughput sample preparation for large-scale tissue proteomics. **b,c,** Number of identified peptides (**b**) and proteins groups (**c**) using indicated proteolytic digestion durations with or without adaptive focused acoustics (AFA)-assisted proteolysis. **d,** Percentages of identified peptides with 0, 1, 2, or 3 missed cleavage sites for indicated proteolytic digestion durations with or without AFA-assisted proteolysis. **e,** Number of identified protein groups with samples prepared from brain, kidney, and lung tissues using the standard and high-throughput workflows. **f-h,** Correlation analysis of the pairwise ratios among three mouse tissues (brain, lung, and kidney) calculated using the data generated by standard and high-throughput workflows. **i,j,** Comparison of the estimated time cost for the standard and high-throughput workflows.

Fig. 3 | Tissue proteomic landscape of ASNase treatment

a, Biochemical reactions catalyzed by $ASNase^{WT}$ and $ASNase^{Q59L}$. **b,** Schematic overview of the experimental design. **c,** Overview of the mouse tissues collected for mass spectrometry proteomic analysis. **d,** Total number of proteins identified in each tissue across all treatment groups. **e,** Correlation matrix heatmap of the data generated from 13 mouse tissues. The heatmap was generated using Python. The Pearson correlation coefficient values were calculated based on the MS intensities of each protein in certain samples. **f,** Unsupervised clustering of tissue proteomics data via t-SNE. **g,** Protein abundance in 13 tissues over an 8-d time course of PBS, $ASNase^{WT}$, or $ASNase^{Q59L}$ treatments. t, time.

Fig. 4 | Validation of ASNase efficacy on amino acid metabolism

a, System environment architecture of asparaginase (ASNase). **b-e,** The metabolodynamics of asparagine (ASN) (**b**), aspartic acid (ASP) (**c**), glutamine (GLN) (**d**), and glutamic acid (GLU) (**e**)

673 in blood following either PBS, ASNase^{WT}, or ASNase^{Q59L} treatment. **f,** The metabolodynamics
674 of ASN, ASP, GLN, and GLU in the six indicated solid tissues following either PBS, ASNase^{WT},
675 or ASNase^{Q59L} treatment. **g,** The dynamic protein levels of ASNS in thirteen indicated solid
676 tissues following either PBS, ASNase^{WT}, or ASNase^{Q59L} treatment.

677

678 **Fig. 5 | Statistical overview and KEGG pathway enrichment analysis of proteins**
679 **modulated by ASNase treatment**

680 **a,** Protein expression levels following ASNase^{WT} treatment were compared with PBS-treated
681 controls. Proteins with a fold change greater than 2 and a p-value less than 0.05 were classified
682 as up-regulated. Data from all the time points (1d, 3d, 5d, and 8d) were grouped together. **b,**
683 Same as (**a**) except proteins with a fold change less than 0.5 and a p-value less than 0.05 were
684 classified as down-regulated. **c,** Same as (**a**) except ASNase^{Q59L} compared to PBS treatment. **d,**
685 Same as (**b**) except ASNase^{Q59L} compared to PBS treatment. **e,** KEGG pathway analysis of the
686 up- or down-regulated proteins following ASNase^{WT} treatment in the indicated tissues. **f,** Same
687 as (**e**) except ASNase^{Q59L} treatment.

688

689 **Fig. 6 | ASNase dysregulates a common set of proteins across multiple tissue types**

690 **a,** Heatmap overview of the dynamic protein levels change of proteins involved in the
691 complement and coagulation cascades (top) and the cholesterol metabolism pathway (bottom)
692 following ASNase^{WT} or ASNase^{Q59L} treatment across all the tested tissues. Protein expression
693 levels following ASNase^{WT} or ASNase^{Q59L} treatment were compared to PBS-treated controls,
694 with the Log2 fold change values presented. **b-e,** Statistical summary of the dysregulated
695 proteins that were common in certain number of tissues. Dysregulation proteins were filtered
696 with a p-value < 0.05 and fold change > 2 or < 0.5. Proteins commonly dysregulated in at least
697 three tissues were colored in red (up-regulation) or blue (down-regulation). **f,** Venn diagram of
698 proteins downregulated by ASNase^{WT}, proteins involved in the complement system, and
699 proteins involved in cholesterol metabolism. **g,h,** Downregulated proteins involved in (**g**)
700 complement system or (**h**) cholesterol metabolism following ASNase^{WT} treatment. Only proteins
701 significantly modulated in at least three tissues are displayed.

702

703 **Fig. 7 | Modulation of the spleen proteome by ASNase. a-c,** KEGG pathway analysis of the
704 upregulated or downregulated proteins following 3 days (**a**), 5 days (**b**), and 8 days (**c**)
705 ASNase^{WT} treatment in the spleen. **d**, Heatmap overview of the dynamic protein levels change
706 of proteins involved in lysosome, glutathione metabolism, ferroptosis, DNA replication, ribosome
707 and translation, and mitochondria following ASNase^{WT} or ASNase^{Q59L} treatment across all the
708 tested tissues. Protein expression levels following ASNase^{WT} or ASNase^{Q59L} treatment were
709 compared to PBS-treated controls, with the Log2 fold change values presented. **e,** Glutathione
710 levels in spleen samples from mice treated with PBS, ASNase^{WT}, or ASNase^{Q59L} for 8 d. **f,** The
711 dynamic regulation of indicated amino acid levels following 8 days treatment with ASNase^{WT} or
712 ASNase^{Q59L} treatment in the spleen. **g,** Polar metabolite levels in spleen samples from mice
713 treated with ASNase^{WT} for 8d. **h,** Model of spleen vulnerability to ASNase^{WT} treatment.

714

715

Figure 1

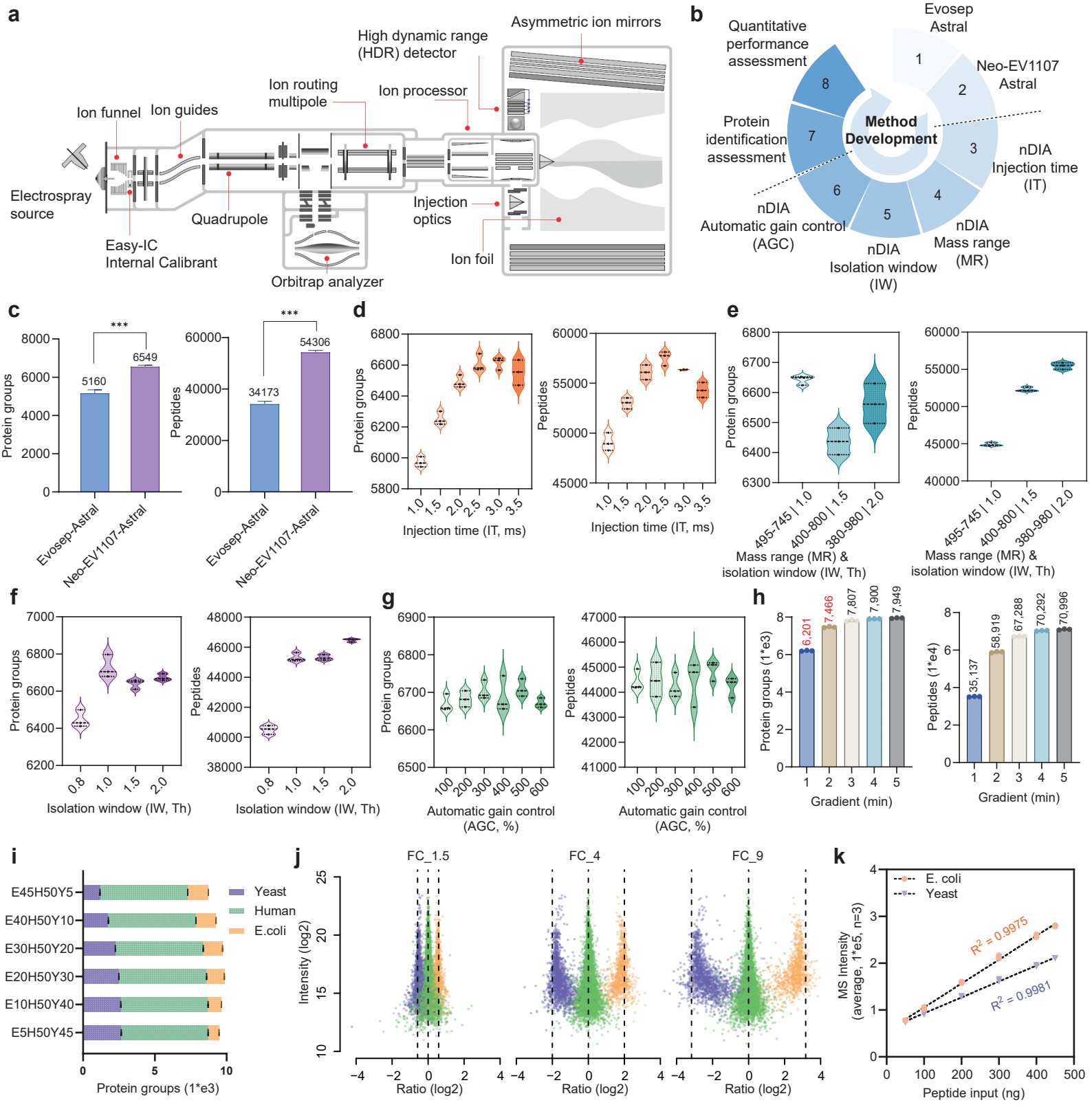
a
Asymmetric ion mirrors
High dynamic range (HDR) detector
Ion routing multipole
Ion processor
Ion funnel
Ion guides
Electrospray source
Quadrupole
Injection optics
Easy-IC Internal Calibrant
Ion foil
Orbitrap analyzer
b
Evosep Astral
Neo-EV1107 Astral
nDIA Injection time (IT)
nDIA Mass range (MR)
nDIA Isolation window (IW)
nDIA Automatic gain control (AGC)
Protein identification assessment
Quantitative performance assessment
Method Development
c
Protein groups
Peptides
Evosep-Astral
Neo-EV1107-Astral
d
Injection time (IT, ms)
e
Mass range (MR) & isolation window (IW, Th)
f
Isolation window (IW, Th)
g
Automatic gain control (AGC, %)
h
Protein groups (1*e3)
Peptides (1*e4)
Gradient (min)
i
Yeast
Human
E.coli
Protein groups (1*e3)
j
FC_1.5
FC_4
FC_9
Intensity (log2)
Ratio (log2)
k
E. coli
Yeast
MS Intensity (average, 1*e5, n=3)
Peptide input (ng)

Figure 2

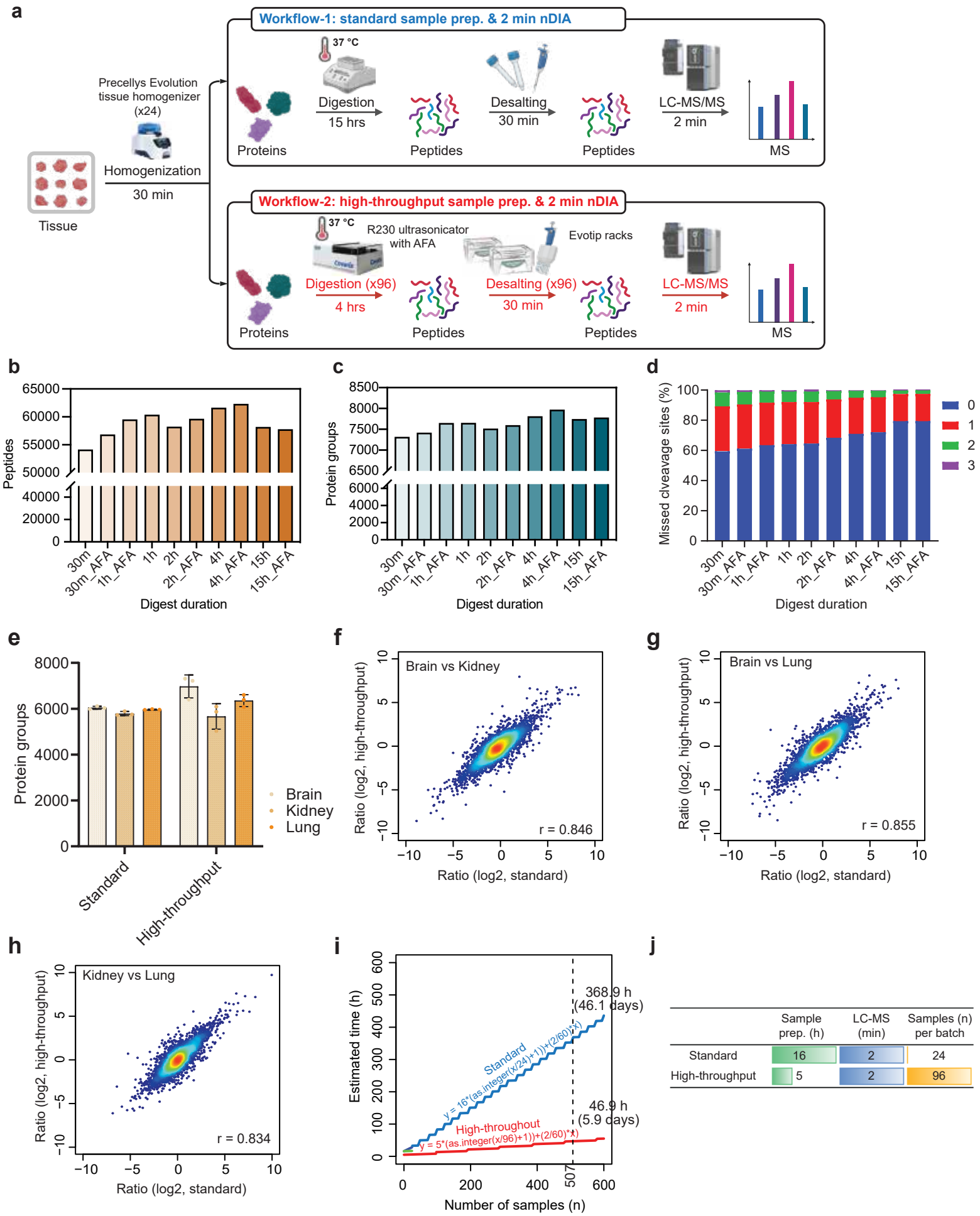
a
Workflow-1: standard sample prep. & 2 min nDIA
37 °C
Digestion
15 hrs
Desalting
30 min
LC-MS/MS
2 min
Proteins
Peptides
Peptides
MS
Precellys Evolution tissue homogenizer (x24)
Homogenization
30 min
Tissue
Workflow-2: high-throughput sample prep. & 2 min nDIA
37 °C
R230 ultrasonicator with AFA
Evotip racks
Digestion (x96)
4 hrs
Desalting (x96)
30 min
LC-MS/MS
2 min
Proteins
Peptides
Peptides
MS
b
Peptides
Digest duration
c
Protein groups
Digest duration
d
Missed clveavage sites (%)
Digest duration
e
Protein groups
Brain
Kidney
Lung
Standard
High-throughput
f
Brain vs Kidney
r = 0.846
Ratio (log2, high-throughput)
Ratio (log2, standard)
g
Brain vs Lung
r = 0.855
Ratio (log2, high-throughput)
Ratio (log2, standard)
h
Kidney vs Lung
r = 0.834
Ratio (log2, high-throughput)
Ratio (log2, standard)
i
Estimated time (h)
368.9 h
(46.1 days)
46.9 h
(5.9 days)
Standard
y = 16*(as.integer(x/24)+1))+(2/60)*x)
High-throughout
y = 5*(as.integer(x/96)+1))+(2/60)*x)
507
Number of samples (n)
j
Sample prep. (h)
LC-MS (min)
Samples (n) per batch
Standard 16 2 24
High-throughput 5 2 96

Figure 3

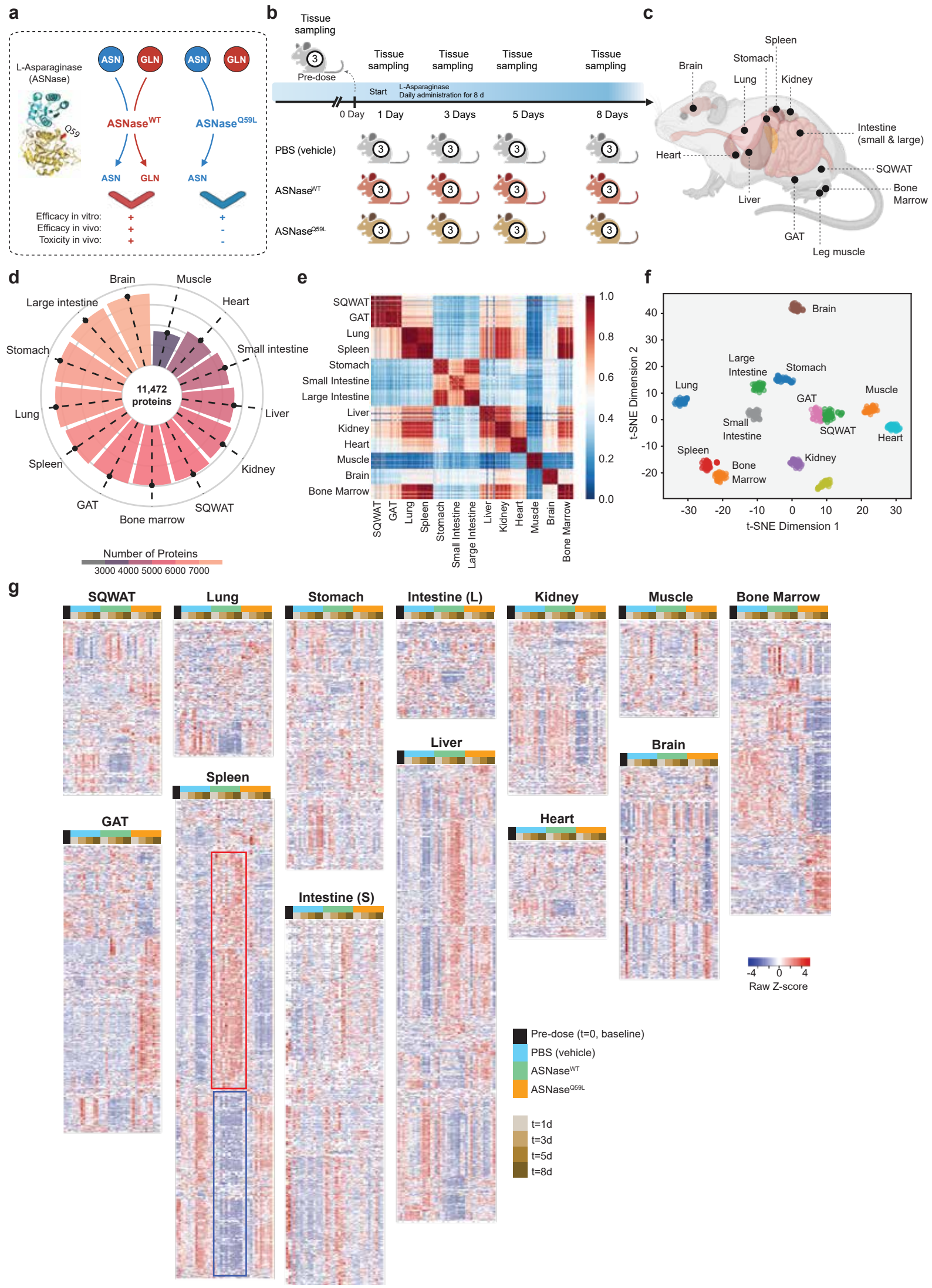
a
L-Asparaginase (ASNase)
ASN
GLN
ASNase^WT
ASNase^Q59L
Q59
Efficacy in vitro:
Efficacy in vivo:
Toxicity in vivo:
b
Tissue sampling
Pre-dose
Start
L-Asparaginase Daily administration for 8 d
0 Day
1 Day
3 Days
5 Days
8 Days
PBS (vehicle)
ASNase^WT
ASNase^Q59L
c
Spleen
Stomach
Brain
Lung
Kidney
Intestine (small & large)
Heart
SQWAT
Bone Marrow
Liver
GAT
Leg muscle
d
Brain
Muscle
Large intestine
Heart
Stomach
Small intestine
11,472 proteins
Lung
Liver
Spleen
Kidney
GAT
SQWAT
Bone marrow
Number of Proteins
3000 4000 5000 6000 7000
e
SQWAT
GAT
Lung
Spleen
Stomach
Small Intestine
Large Intestine
Liver
Kidney
Heart
Muscle
Brain
Bone Marrow
1.0
0.8
0.6
0.4
0.2
0.0
f
t-SNE Dimension 1
t-SNE Dimension 2
Brain
Large Intestine
Stomach
Lung
Muscle
GAT
Small Intestine
SQWAT
Heart
Spleen
Kidney
Bone Marrow
g
SQWAT
Lung
Stomach
Intestine (L)
Kidney
Muscle
Bone Marrow
Spleen
Liver
Brain
GAT
Heart
Intestine (S)
Raw Z-score
Pre-dose (t=0, baseline)
PBS (vehicle)
ASNase^WT
ASNase^Q59L
t=1d
t=3d
t=5d
t=8d

Figure 4

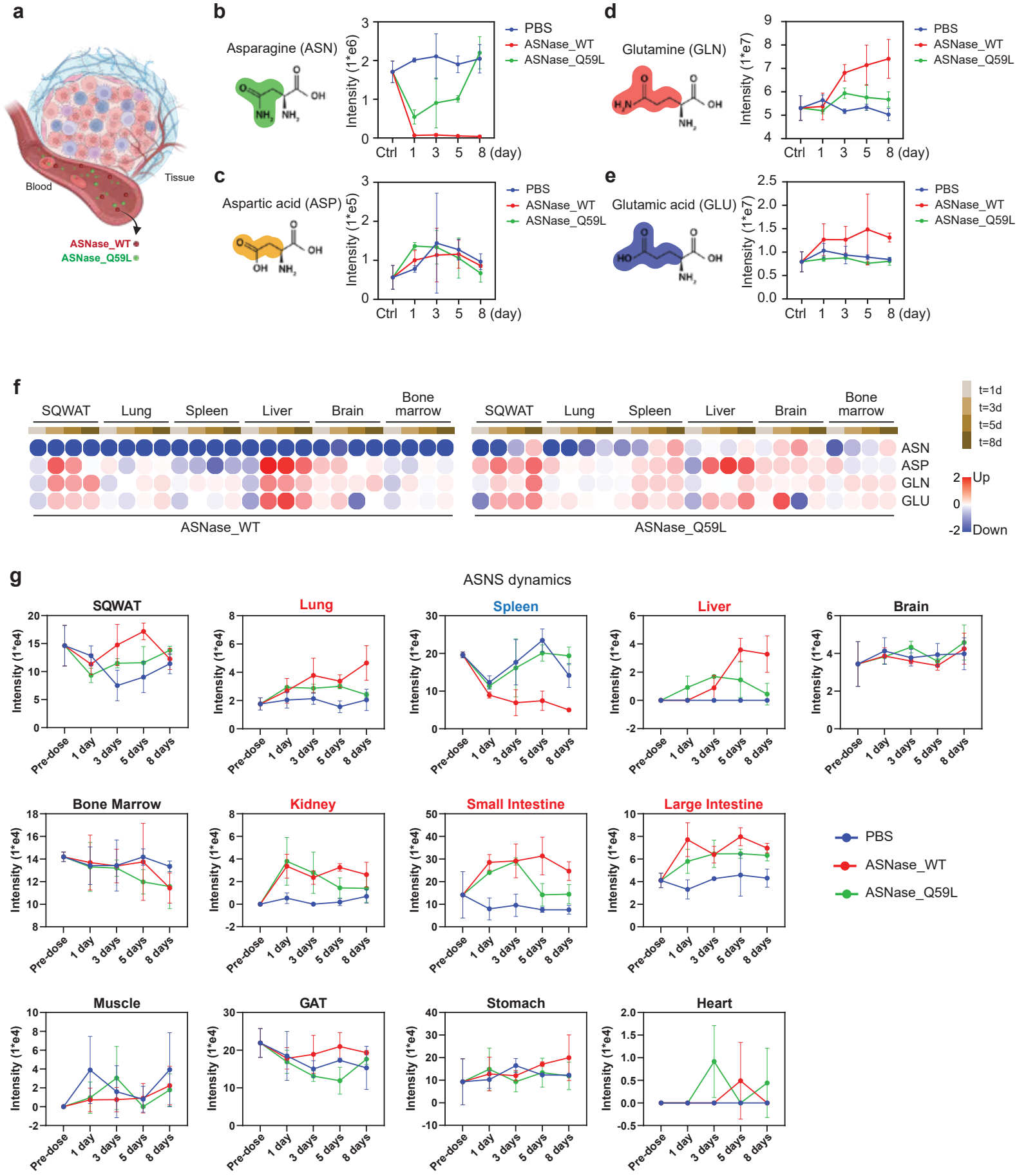
a
Blood
Tissue
ASNase_WT
ASNase_Q59L
b
Asparagine (ASN)
Intensity (1*e6)
PBS
ASNase_WT
ASNase_Q59L
Ctrl 1 3 5 8 (day)
c
Aspartic acid (ASP)
Intensity (1*e5)
d
Glutamine (GLN)
Intensity (1*e7)
e
Glutamic acid (GLU)
Intensity (1*e7)
f
SQWAT
Lung
Spleen
Liver
Brain
Bone marrow
ASN
ASP
GLN
GLU
ASNase_WT
ASNase_Q59L
t=1d
t=3d
t=5d
t=8d
Up
Down
g
ASNS dynamics
SQWAT
Lung
Spleen
Liver
Brain
Bone Marrow
Kidney
Small Intestine
Large Intestine
Muscle
GAT
Stomach
Heart
Intensity (1*e4)
Pre-dose
1 day
3 days
5 days
8 days
PBS
ASNase_WT
ASNase_Q59L

Figure 5

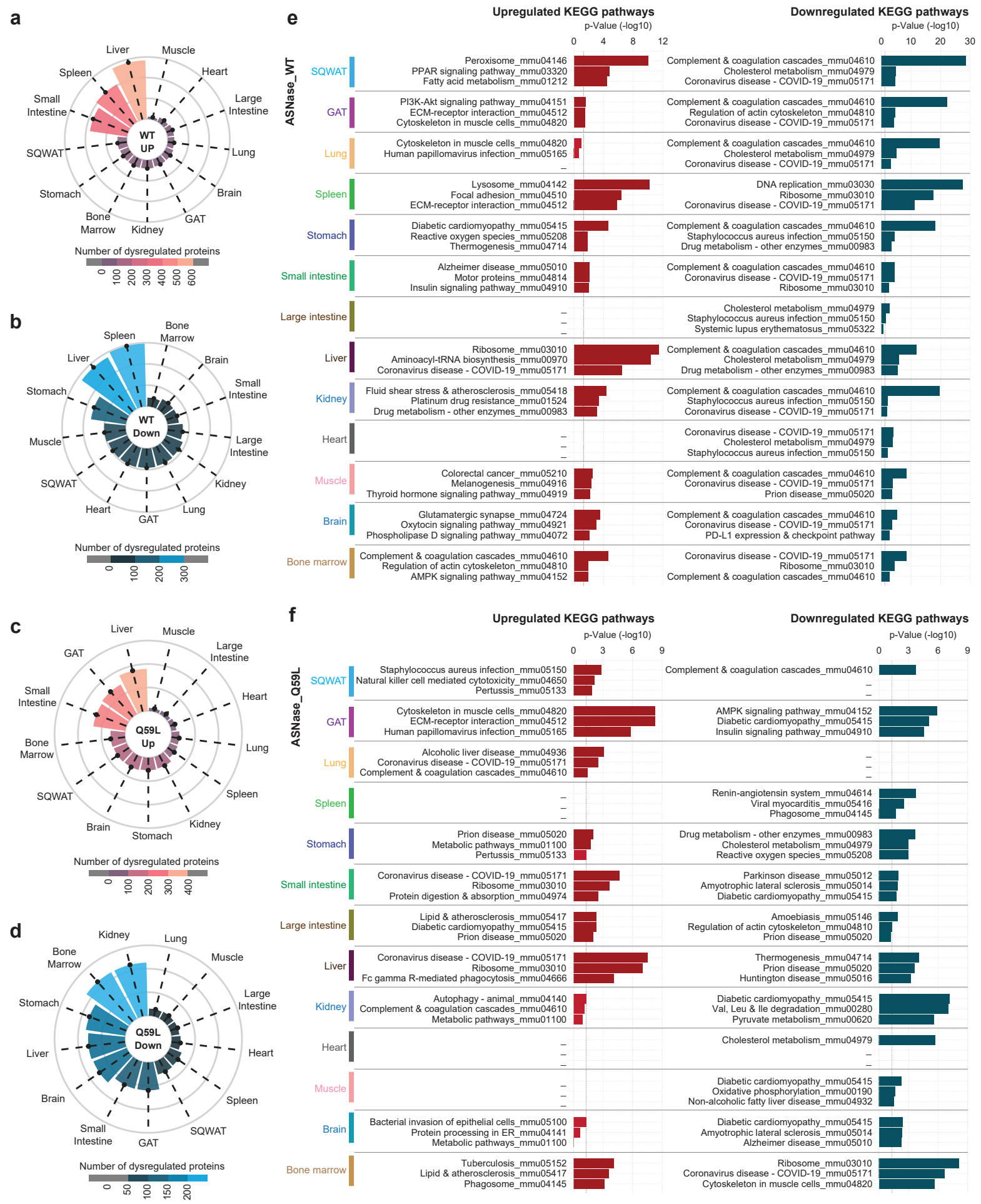
a
Liver
Muscle
Heart
Large Intestine
Lung
Brain
GAT
Kidney
Bone Marrow
Stomach
SQWAT
Small Intestine
Spleen
WT UP
Number of dysregulated proteins
0 100 200 300 400 500 600
b
Bone Marrow
Brain
Small Intestine
Large Intestine
Kidney
Lung
GAT
Heart
SQWAT
Muscle
Stomach
Liver
Spleen
WT Down
Number of dysregulated proteins
0 100 200 300
c
Liver
Muscle
Large Intestine
Heart
Lung
Spleen
Kidney
Stomach
Brain
SQWAT
Bone Marrow
Small Intestine
GAT
Q59L Up
Number of dysregulated proteins
0 100 200 300 400
d
Kidney
Lung
Muscle
Large Intestine
Heart
Spleen
SQWAT
GAT
Small Intestine
Brain
Liver
Stomach
Bone Marrow
Q59L Down
Number of dysregulated proteins
0 50 100 150 200
e
Upregulated KEGG pathways
p-Value (-log10)
0 4 8 12
Downregulated KEGG pathways
p-Value (-log10)
0 10 20 30
ASNase_WT
SQWAT
Peroxisome_mmu04146
PPAR signaling pathway_mmu03320
Fatty acid metabolism_mmu01212
Complement & coagulation cascades_mmu04610
Cholesterol metabolism_mmu04979
Coronavirus disease - COVID-19_mmu05171
GAT
PI3K-Akt signaling pathway_mmu04151
ECM-receptor interaction_mmu04512
Cytoskeleton in muscle cells_mmu04820
Complement & coagulation cascades_mmu04610
Regulation of actin cytoskeleton_mmu04810
Coronavirus disease - COVID-19_mmu05171
Lung
Cytoskeleton in muscle cells_mmu04820
Human papillomavirus infection_mmu05165
Complement & coagulation cascades_mmu04610
Cholesterol metabolism_mmu04979
Coronavirus disease - COVID-19_mmu05171
Spleen
Lysosome_mmu04142
Focal adhesion_mmu04510
ECM-receptor interaction_mmu04512
DNA replication_mmu03030
Ribosome_mmu03010
Coronavirus disease - COVID-19_mmu05171
Stomach
Diabetic cardiomyopathy_mmu05415
Reactive oxygen species_mmu05208
Thermogenesis_mmu04714
Complement & coagulation cascades_mmu04610
Staphylococcus aureus infection_mmu05150
Drug metabolism - other enzymes_mmu00983
Small intestine
Alzheimer disease_mmu05010
Motor proteins_mmu04814
Insulin signaling pathway_mmu04910
Complement & coagulation cascades_mmu04610
Coronavirus disease - COVID-19_mmu05171
Ribosome_mmu03010
Large intestine
Cholesterol metabolism_mmu04979
Staphylococcus aureus infection_mmu05150
Systemic lupus erythematosus_mmu05322
Liver
Ribosome_mmu03010
Aminoacyl-tRNA biosynthesis_mmu00970
Coronavirus disease - COVID-19_mmu05171
Complement & coagulation cascades_mmu04610
Cholesterol metabolism_mmu04979
Drug metabolism - other enzymes_mmu00983
Kidney
Fluid shear stress & atherosclerosis_mmu05418
Platinum drug resistance_mmu01524
Drug metabolism - other enzymes_mmu00983
Complement & coagulation cascades_mmu04610
Staphylococcus aureus infection_mmu05150
Coronavirus disease - COVID-19_mmu05171
Heart
Coronavirus disease - COVID-19_mmu05171
Cholesterol metabolism_mmu04979
Staphylococcus aureus infection_mmu05150
Muscle
Colorectal cancer_mmu05210
Melanogenesis_mmu04916
Thyroid hormone signaling pathway_mmu04919
Complement & coagulation cascades_mmu04610
Coronavirus disease - COVID-19_mmu05171
Prion disease_mmu05020
Brain
Glutamatergic synapse_mmu04724
Oxytocin signaling pathway_mmu04921
Phospholipase D signaling pathway_mmu04072
Complement & coagulation cascades_mmu04610
Coronavirus disease - COVID-19_mmu05171
PD-L1 expression & checkpoint pathway
Bone marrow
Complement & coagulation cascades_mmu04610
Regulation of actin cytoskeleton_mmu04810
AMPK signaling pathway_mmu04152
Coronavirus disease - COVID-19_mmu05171
Ribosome_mmu03010
Complement & coagulation cascades_mmu04610
f
Upregulated KEGG pathways
p-Value (-log10)
0 3 6 9
Downregulated KEGG pathways
p-Value (-log10)
0 3 6 9
ASNase_Q59L
SQWAT
Staphylococcus aureus infection_mmu05150
Natural killer cell mediated cytotoxicity_mmu04650
Pertussis_mmu05133
Complement & coagulation cascades_mmu04610
GAT
Cytoskeleton in muscle cells_mmu04820
ECM-receptor interaction_mmu04512
Human papillomavirus infection_mmu05165
AMPK signaling pathway_mmu04152
Diabetic cardiomyopathy_mmu05415
Insulin signaling pathway_mmu04910
Lung
Alcoholic liver disease_mmu04936
Coronavirus disease - COVID-19_mmu05171
Complement & coagulation cascades_mmu04610
Spleen
Renin-angiotensin system_mmu04614
Viral myocarditis_mmu05416
Phagosome_mmu04145
Stomach
Prion disease_mmu05020
Metabolic pathways_mmu01100
Pertussis_mmu05133
Drug metabolism - other enzymes_mmu00983
Cholesterol metabolism_mmu04979
Reactive oxygen species_mmu05208
Small intestine
Coronavirus disease - COVID-19_mmu05171
Ribosome_mmu03010
Protein digestion & absorption_mmu04974
Parkinson disease_mmu05012
Amyotrophic lateral sclerosis_mmu05014
Diabetic cardiomyopathy_mmu05415
Large intestine
Lipid & atherosclerosis_mmu05417
Diabetic cardiomyopathy_mmu05415
Prion disease_mmu05020
Amoebiasis_mmu05146
Regulation of actin cytoskeleton_mmu04810
Prion disease_mmu05020
Liver
Coronavirus disease - COVID-19_mmu05171
Ribosome_mmu03010
Fc gamma R-mediated phagocytosis_mmu04666
Thermogenesis_mmu04714
Prion disease_mmu05020
Huntington disease_mmu05016
Kidney
Autophagy - animal_mmu04140
Complement & coagulation cascades_mmu04610
Metabolic pathways_mmu01100
Diabetic cardiomyopathy_mmu05415
Val, Leu & Ile degradation_mmu00280
Pyruvate metabolism_mmu00620
Heart
Cholesterol metabolism_mmu04979
Muscle
Diabetic cardiomyopathy_mmu05415
Oxidative phosphorylation_mmu00190
Non-alcoholic fatty liver disease_mmu04932
Brain
Bacterial invasion of epithelial cells_mmu05100
Protein processing in ER_mmu04141
Metabolic pathways_mmu01100
Diabetic cardiomyopathy_mmu05415
Amyotrophic lateral sclerosis_mmu05014
Alzheimer disease_mmu05010
Bone marrow
Tuberculosis_mmu05152
Lipid & atherosclerosis_mmu05417
Phagosome_mmu04145
Ribosome_mmu03010
Coronavirus disease - COVID-19_mmu05171
Cytoskeleton in muscle cells_mmu04820

Figure 6

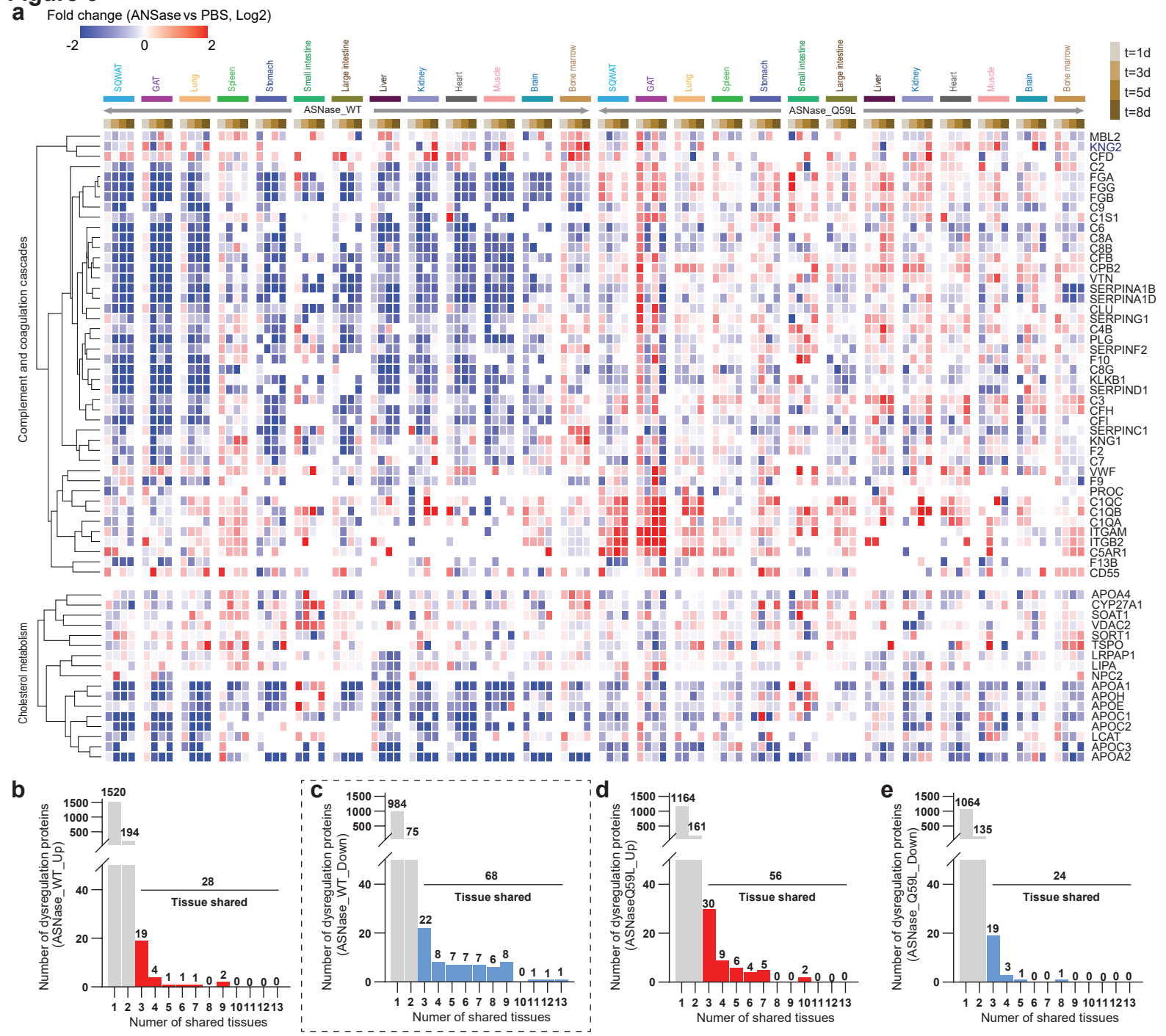
a
Fold change (ANSase vs PBS, Log2)
-2
0
2
SQWAT
GAT
Lung
Spleen
Stomach
Small intestine
Large intestine
Liver
Kidney
Heart
Muscle
Brain
Bone marrow
ASNase_WT
ASNase_Q59L
t=1d
t=3d
t=5d
t=8d
Complement and coagulation cascades
MBL2
KNG2
CFD
C2
FGA
FGG
FGB
C9
C1S1
C6
C8A
C8B
CFB
CPB2
VTN
SERPINA1B
SERPINA1D
CLU
SERPING1
C4B
PLG
SERPINF2
F10
C8G
KLKB1
SERPIND1
C3
CFH
CFI
SERPINC1
KNG1
F2
C7
VWF
F9
PROC
C1QC
C1QB
C1QA
ITGAM
ITGB2
C5AR1
F13B
CD55
Cholesterol metabolism
APOA4
CYP27A1
SOAT1
VDAC2
SORT1
TSPO
LRPAP1
LIPA
NPC2
APOA1
APOH
APOE
APOC1
APOC2
LCAT
APOC3
APOA2

b
Number of dysregulation proteins (ASNase_WT_Up)
1520
194
28
Tissue shared
Numer of shared tissues
c
Number of dysregulation proteins (ASNase_WT_Down)
984
75
68
Tissue shared
Numer of shared tissues
d
Number of dysregulation proteins (ASNaseQ59L_Up)
1164
161
56
Tissue shared
Numer of shared tissues
e
Number of dysregulation proteins (ASNase_Q59L_Down)
1064
135
24
Tissue shared
Numer of shared tissues

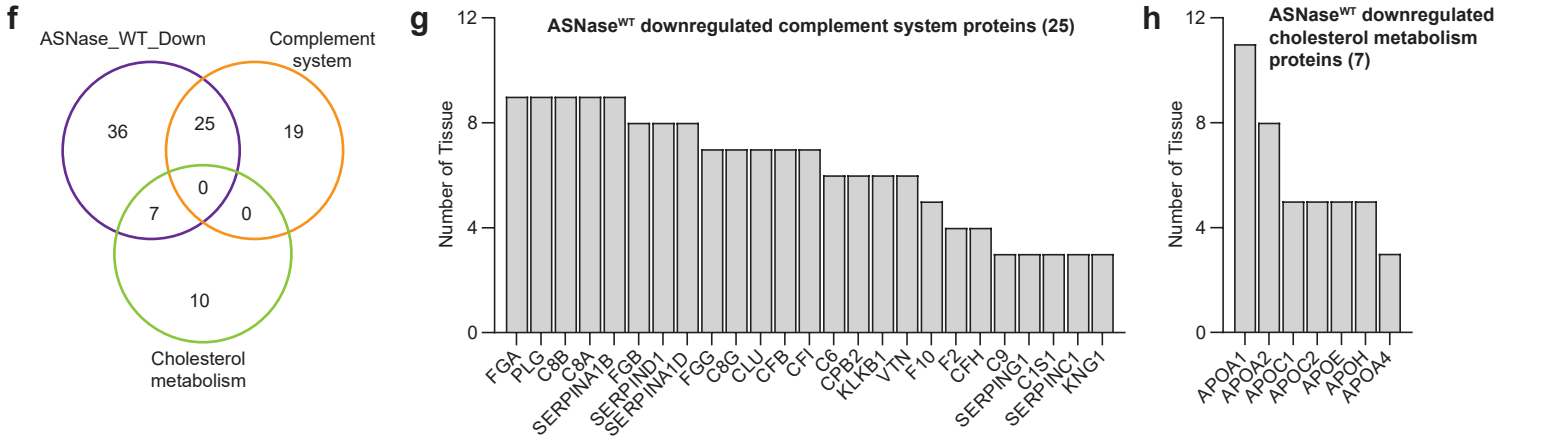
f
ASNase_WT_Down
Complement system
Cholesterol metabolism
36
25
19
0
7
0
10
g
ASNase^WT downregulated complement system proteins (25)
Number of Tissue
FGA
PLG
C8B
C8A
SERPINA1B
FGB
SERPIND1
SERPINA1D
FGG
C8G
CLU
CFB
CFI
C6
CPB2
KLKB1
VTN
F10
F2
CFH
C9
SERPING1
C1S1
SERPINC1
KNG1
h
ASNase^WT downregulated cholesterol metabolism proteins (7)
Number of Tissue
APOA1
APOA2
APOC1
APOC2
APOE
APOH
APOA4

Figure 7

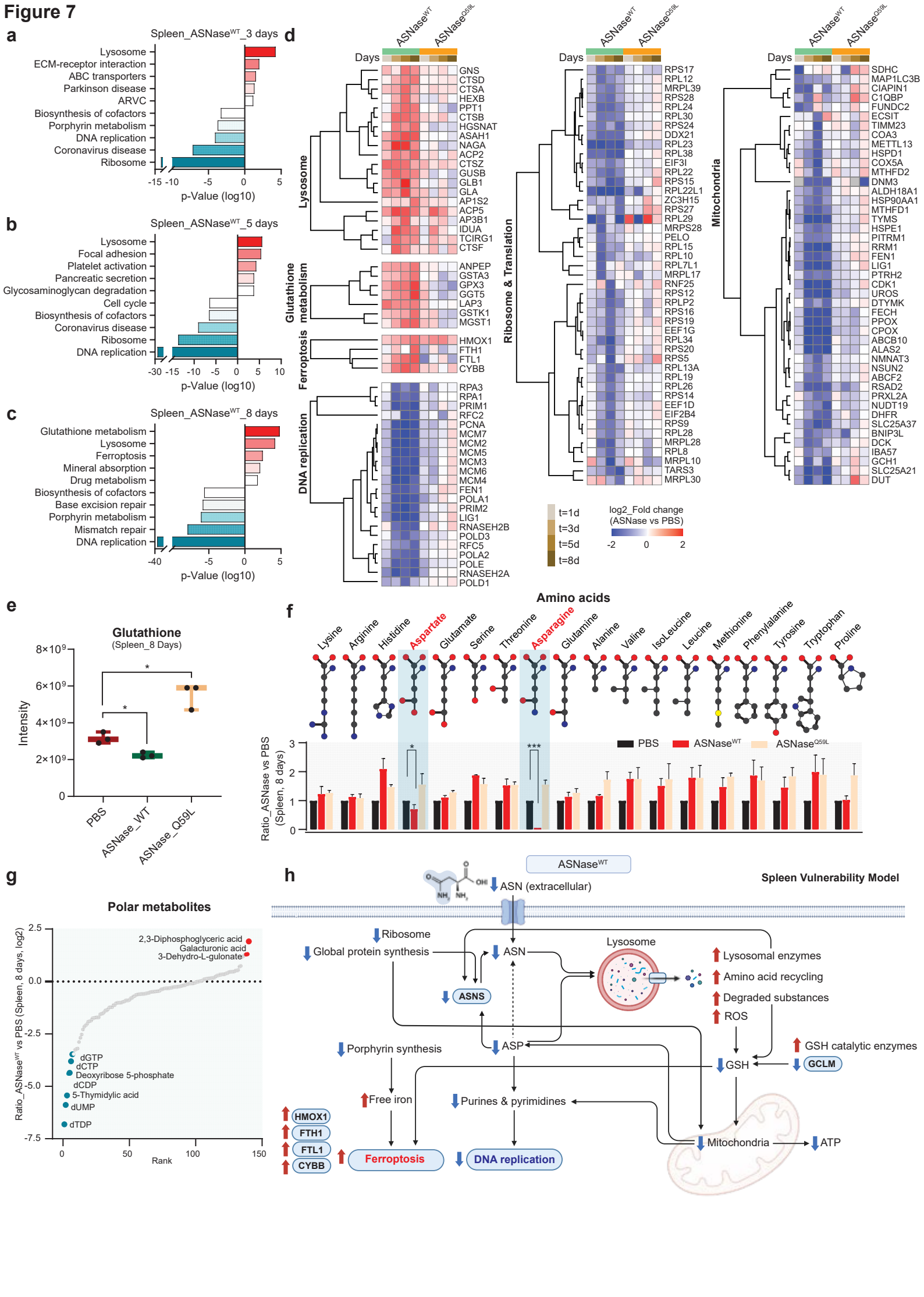
a
Spleen_ASNase^{WT}_3 days
Lysosome
ECM-receptor interaction
ABC transporters
Parkinson disease
ARVC
Biosynthesis of cofactors
Porphyrin metabolism
DNA replication
Coronavirus disease
Ribosome
p-Value (log10)
b
Spleen_ASNase^{WT}_5 days
Lysosome
Focal adhesion
Platelet activation
Pancreatic secretion
Glycosaminoglycan degradation
Cell cycle
Biosynthesis of cofactors
Coronavirus disease
Ribosome
DNA replication
p-Value (log10)
c
Spleen_ASNase^{WT}_8 days
Glutathione metabolism
Lysosome
Ferroptosis
Mineral absorption
Drug metabolism
Biosynthesis of cofactors
Base excision repair
Porphyrin metabolism
Mismatch repair
DNA replication
p-Value (log10)
d
ASNase^{WT}
ASNase^{Q59L}
Days
Lysosome
GNS
CTSD
CTSA
HEXB
PPT1
CTSB
HGSNAT
ASAH1
NAGA
ACP2
CTSZ
GUSB
GLB1
GLA
AP1S2
ACP5
AP3B1
IDUA
TCIRG1
CTSF
Glutathione metabolism
ANPEP
GSTA3
GPX3
GGT5
LAP3
GSTK1
MGST1
Ferroptosis
HMOX1
FTH1
FTL1
CYBB
DNA replication
RPA3
RPA1
PRIM1
RFC2
PCNA
MCM7
MCM2
MCM5
MCM3
MCM6
MCM4
FEN1
POLA1
PRIM2
LIG1
RNASEH2B
POLD3
RFC5
POLA2
POLE
RNASEH2A
POLD1
Ribosome & Translation
RPS17
RPL12
MRPL39
RPS28
RPL24
RPL30
RPS24
DDX21
RPL23
RPL38
EIF3I
RPL22
RPS15
RPL22L1
ZC3H15
RPS27
RPL29
MRPS28
PELO
RPL15
RPL10
RPL7L1
MRPL17
RNF25
RPS12
RPLP2
RPS16
RPS19
EEF1G
RPL34
RPS20
RPS5
RPL13A
RPL19
RPL26
RPS14
EEF1D
EIF2B4
RPS9
RPL28
MRPL28
RPL8
MRPL10
TARS3
MRPL30
Mitochondria
SDHC
MAP1LC3B
CIAPIN1
C1QBP
FUNDC2
ECSIT
TIMM23
COA3
METTL13
HSPD1
COX5A
MTHFD2
DNM3
ALDH18A1
HSP90AA1
MTHFD1
TYMS
HSPE1
PITRM1
RRM1
FEN1
LIG1
PTRH2
CDK1
UROS
DTYMK
FECH
PPOX
CPOX
ABCB10
ALAS2
NMNAT3
NSUN2
ABCF2
RSAD2
PRXL2A
NUDT19
DHFR
SLC25A37
BNIP3L
DCK
IBA57
GCH1
SLC25A21
DUT
t=1d
t=3d
t=5d
t=8d
log2_Fold change
(ASNase vs PBS)
-2
0
2
e
Glutathione
(Spleen_8 Days)
Intensity
PBS
ASNase_WT
ASNase_Q59L
f
Amino acids
Lysine
Arginine
Histidine
Aspartate
Glutamate
Serine
Threonine
Asparagine
Glutamine
Alanine
Valine
IsoLeucine
Leucine
Methionine
Phenylalanine
Tyrosine
Tryptophan
Proline
PBS
ASNase^{WT}
ASNase^{Q59L}
Ratio_ASNase vs PBS
(Spleen, 8 days)
g
Polar metabolites
2,3-Diphosphoglyceric acid
Galacturonic acid
3-Dehydro-L-gulonate
dGTP
dCTP
Deoxyribose 5-phosphate
dCDP
5-Thymidylic acid
dUMP
dTDP
Ratio_ASNase^{WT} vs PBS (Spleen, 8 days, log2)
Rank
h
Spleen Vulnerability Model
ASNase^{WT}
ASN (extracellular)
Ribosome
Global protein synthesis
ASN
Lysosome
Lysosomal enzymes
Amino acid recycling
Degraded substances
ROS
ASNS
ASP
Porphyrin synthesis
GSH catalytic enzymes
GSH
GCLM
Free iron
Purines & pyrimidines
HMOX1
FTH1
FTL1
CYBB
Ferroptosis
DNA replication
Mitochondria
ATP

Supplementary Materials for

Ultra-Fast Multi-Organ Proteomics Unveils Tissue-Specific Mechanisms of Drug Efficacy and Toxicity

Yun Xiong[1,2,3,#], Lin Tan[1,2,3,#], Wai-kin Chan[1,3,#], Eric S. Yin[1,3], Sri Ramya Donepudi[1,4], Jibin Ding[1,2,3], Bo Wei[1,3], Bao Tran[1,3], Sara Martinez[1,3], Iqbal Mahmud[1,3], Hamish I. Stewart[5], Daniel J. Hermanson[5], John N. Weinstein[1,2,3], Philip L. Lorenzi[1,2,3,*]

Corresponding author: PLLorenzi@mdanderson.org

The PDF file includes:

Supplementary Results
Supplementary Discussion
Online methods
References
Supplementary figure 1 to 19

Other Supplementary Materials for this manuscript include the following:

Supplementary Tables 1 to 27

Supplementary Results

ASNase dysregulates system-wide and tissue-specific pathways

In addition to its broad impact on lipid metabolism and the complement system, ASNase^{WT} induces specific dysregulation of various pathways in different tissues. Notably, while ribosomal proteins were reduced in the spleen, small intestine, and bone marrow, ASNase^{WT} treatment led to a significant increase in proteins associated with 'ribosome,' 'ribosome biogenesis,' and 'aminoacyl-tRNA synthesis' in the liver (Supplementary Fig. 18a). In parallel, drug-treated liver exhibited significant up-regulation of amino acids (Supplementary Fig. 16b). This suggests heightened protein biosynthesis activity in the liver. Furthermore, purine metabolism and RNA polymerases were also upregulated by ASNase^{WT} at 8 d (Supplementary Fig. 18a), indicating elevated gene expression in the drug-treated liver. These observations are consistent with the well-known function of liver in synthesizing plasma proteins(*1*), and it is not surprising to see evidence of the liver remaining a protein synthesis factory in the presence of significant nutrient stress.

Bone marrow serves as the microenvironment for leukemias and is known to protect leukemia cells against ASNase by secreting ASN to feed the cancer cells or lysosomal cysteine proteases to degrade and clear ASNase(*2*). We observed significant bone marrow up-regulation of cysteine proteases including CTSC, CTSG, and CTSL after 8 d of ASNase^{WT} treatment (Supplementary Fig. 18b). ASNase^{Q59L} also induced up-regulation of CTSC and CTSG (Supplementary Table 11). KEGG pathway enrichment analysis revealed up-regulation of the “complement and coagulation cascades” pathway in the bone marrow—the opposite direction observed in other tissues. Additionally, proteins involved in “AMPK signaling” and “PPAR signaling” were also induced, including ADIPOQ, SCD1, PCK1, and PIK3R2. These observations are consistent with previous reports that ASNase treatment or ASNS knockdown activated AMPK(*3*), which is a negative modulator of TORC1 and a positive modulator of autophagy, which connects to the observed up-regulation of lysosomal proteases.

ASNase^{WT} treatment induced distinct responses in the two adipose tissue depots, The gonadal adipose tissue (GAT) exhibited induction of “PI3K-Akt signaling,” “ECM-receptor interaction,” and “Focal adhesion” pathways (Supplementary Fig. 18d). The proteins in those pathways are largely overlapping, including COL4A6, COL6A5, TEK, THBS1, and MCL1. TEK, THBS1, and COL4A6 have also been categorized under “PI3K-Akt-mTOR signaling” according to WikiPathways(*4*). The subcutaneous white adipose tissue (SQWAT) exhibited up-regulation of multiple proteins involved in PPAR signaling, including SLC27A1, SLC27A4, ACAA1A, ACAA1B, ACSL1, EHHADH, and PCK1 (Supplementary Fig. 18c), which are primarily associated with fatty acid metabolism. SQWAT is the largest fat depot in most individuals, a critical energy storage depot, and, consequently, known to be more metabolically active than GAT. Hence, the up-regulation of fatty acid metabolism likely represents an adaptive response to nutrient stress induced by ASNase^{WT}.

Notably, the "ECM-receptor interaction" and "Focal adhesion" pathways were up-regulated in several tissues, including GAT, lung, stomach, spleen, and liver (Supplementary Fig. 18e). These pathways involve various collagen subunits (COL1A1, COL1A2, COL4A2, COL4A6, COL6A1, COL6A2, COL6A3, and COL6A5) and integrins (ITGA1, ITGA7, ITGA8, ITGAV, ITGB4). ASNase has been reported to disrupt glycosylation, affecting interactions between microvascular endothelial cells, ovarian cancer cells, and ECM components, thereby inhibiting cancer-induced angiogenesis and cancer invasion of surrounding tissues(*5*). In another study, PEGylated ASNase was associated with liver fibrosis due to excessive extracellular matrix (ECM) accumulation(*6*). In ASNase-treated liver, our metabolomic data revealed an increase in 4-hydroxyproline, a major component of collagen that plays a key role in collagen stability(*7*)

(Supplementary Fig. 19). Modulation of ECM components may also be associated with inhibition of metastasis by ASNase treatment and ASNS knockdown(*8*).

Another side effect of ASNase is abdominal or stomach pain. Our proteomic data showed up-regulation of “reactive oxygen species (ROS)” and “oxidation phosphorylation” in stomach (Supplementary Fig. 18f). Proteins associated with these categories include mitochondrial inner membrane proteins, such as NADH dehydrogenase subunits (NDUFB3 and NDUFB6), cytochrome c oxidase subunit 6C (COX6C), ATP synthase subunit f (ATP5MF), voltage-dependent anion-selective channel protein 2 (VDAC2), and GTPase NRAS (NRAS).

Like the situation in spleen, glutathione metabolism-related proteins, including various glutathione S-transferases (GSTA1, GSTA3, GSTO1, and GSTT2), were up-regulated in the kidney (Supplementary Fig. 18g). These GSTs are included in the top-3 KEGG pathways induced by ASNase^{WT} in the kidney (Supplementary Fig. 9). ASNS was increased by both ASNase variants in kidney, alongside an increase of several other proteins (PSAT1, GPT2, and PHGDH) involved in amino acid biosynthesis (Supplementary Fig. 18g).

The mTOR signaling pathway was notably induced in ASNase^{WT}-treated small intestine (Supplementary Fig. 18h), with key proteins including GTPase KRas (KRAS), dual specificity mitogen-activated protein kinase kinase 1 (MAP2K1), eukaryotic translation initiation factor 4E (EIF4E), insulin receptor subunit alpha (INSR), V-type protein ATPase catalytic subunit A (ATP6V1A), segment polarity protein disheveled homolog DVL-2, large neutral amino acid transporter small subunit 1 (SLC7A5), and calcium-binding protein 39 (CAB39), which binds and activates STK11/LKB1. We also observed massive up-regulation of amino acid metabolism-related sub-pathways including arginine and proline metabolism, beta-alanine metabolism, and aminoacyl-tRNA biosynthesis, which was also induced in ASNase^{WT}-treated liver. ASNase^{WT} also induced N-glycan biosynthesis in the small intestine.

In conjunction with elevated Wnt signaling, pharmacologic inhibition of glycogen synthase kinase-3 alpha (GSK3A) was reported to re-sensitize ASNase-resistant leukemias to ASNase through inhibition of proteasome activity(*9*). Here, we found notable induction of Wnt signaling pathway in ASNase^{WT}-treated muscle (Supplementary Fig. 18i); the underlying proteins were glycogen synthase kinase-3 beta (GSK3B), catenin beta-1 (CTNNB1), and cAMP-dependent protein kinase catalytic subunit beta (PRKACB). Because our other analyses identified muscle as a targetable vulnerability of ASNase^{WT}, these findings suggest that future efforts to test ASNase against sarcomas should include combination with GSK3A inhibitors.

Despite the inability of ASNase to cross the blood-brain barrier, decreased blood ASN levels can lead to decreased ASN levels in cerebrospinal fluid(*10*). Indeed, ASNase toxicity on the central nervous system is well-documented(*11*). Our data showed up-regulation of several pathways in ASNase^{WT}-treated brain, with "glutamatergic synapse" being the top-ranked category (Supplementary Fig. 18j). This pathway involves glutamate receptors and signaling proteins, including metabotropic glutamate receptor 3 (GRM3) and other synaptic signaling proteins. These observations may offer insight into ASNase-induced CNS toxicity.

The lung, large intestine, and heart did not reveal significant pathway modulation by ASNase (Supplementary Fig. 4, 11, 15). However, NOTCH1 and several ECM components (COL6A2, COL6A6, and FBN1) were increased following ASNase^{WT} treatment in lung (Supplementary Table 15).

Supplementary Discussion

It is worthwhile to briefly review the history of rapid sample preparation and fast MS acquisition methods, as our work builds upon these previously reported advancements.

As described, sample preparation and MS data acquisition are becoming the limiting steps of MS-based proteomics studies, due to the rapid development in data analysis tools(*12-16*). Many different workflows have been developed for specific sample types and experimental goals(*17, 18*). One attempt to address the issue is the In-StageTip method, which facilitates high-throughput preparation of eukaryotic cell samples but requires a custom, 96-well StageTip holder(*19*). Pressure cycling technology (PCT) requires ~3h to process 16 samples in one batch(*20*). Adaptive focused acoustics (AFA) technology for rapid sample processing in FFPE tissue proteomics has shown significant promise(*21*). Another promising approach is a simple and efficient workflow that enables simultaneous preparation of up to 192 cell lysate samples in less than 7 h for proteomics analysis, and this method is also suitable for plasma samples(*22*). Despite these advances, there is still an urgent need for faster sample preparation methods that can keep pace with the latest analytical technologies.

In addition to throughput, proteome coverage is another critical challenge in proteomic research due to the wide range of protein expression levels in cells, ranging from tens to over a million copies per cell. To address this complexity, offline peptide fractionation with strong cation exchange (SCX) chromatography, high-pH C18, or hydrophilic interaction liquid chromatography (HILIC), has traditionally been employed to reduce sample complexity and enhance proteome coverage in MS analyses(*23-25*). Yet, this approach necessitates extensive instrument time and large sample volumes to generate and analyze multiple fractions per sample, limiting its scalability in high-throughput systems biology studies, particularly those with restricted sample availability. Prompted by those limitations, single-shot analyses strategies leveraging improved MS data acquisition speeds and sensitivity are becoming more popular. The BoxCar MS1 profiling method quantifies >10,000 proteins in 100 min using a Q Exactive HF MS with the need of a pre-compiled spectral library(*26*). Another group identified 10,044 proteins in 120 min using DIA-based single-shot proteomics on an Orbitrap Exploris 480 MS coupled with FAIMS(*27*). The Thin-diaPASEF method successfully detected up to 11,698 unique proteins from human cancer cell lines with a 100 min active gradient using timsTOF HT(*28*). Recently, several studies measured ~10,000 identified proteins within one hour using Orbitrap Astral MS(*29-31*).

Leveraging the high scan speed of TripleTOF 6600 mass spectrometer, scanning SWATH (sSWATH) method was reported to enable ultra-fast proteomics with 0.5 to 5-minute chromatographic gradients at high flow rates (800 µL/min). Using this approach, they quantified 1,937, 2,720, and 4,470 proteins from 5 µg of human cell lysate digests with 0.5-, 1-, and 5-minute LC gradients, respectively. Another group optimized a DIA method that identified >5,000 proteins from 1 µg of HEK293T cell digest in a 5-min gradient using an Orbitrap Exploris 480 MS(*32*). Dia-PASEF has also been successfully employed to fast proteomics analysis with 3-min LC gradient, yielding 5,211 identified proteins from 2 µg cell lysates(*33*). The latest progress in the direction of ultra-fast proteomics method development is the identification of approximately 7,000 proteins with a 5-minute LC gradient on Orbitrap Astral.

In addition to advancements in methodology, the dataset generated in this study introduces several novel aspects and represents a valuable resource for related investigations. Specifically: 1) This study is the first to provide a comprehensive multi-organ proteome-wide analysis of the response mechanisms to ASNase. 2) It integrates large-scale proteomics and metabolomics data for ASNase treatment, offering more detailed and robust evidence at two distinct but interconnected biomolecular levels. 3) While most previous research has focused on the basal levels of ASNS in relation to ASNase efficacy, our dataset provides insights into the quantitative dynamics following drug treatment. 4) Previous studies have primarily examined ASNase treatment for within one or two days. In contrast, our data offer evidence of prolonged drug treatment (up to 8 days), presenting a new perspective on the long-term effects of ASNase.

Online methods

Materials

Water (LC–MS grade, Optima, Cat. No. 10509404), acetonitrile (LC–MS grade, Optima, Cat. No. 10001334), and formic acid (LC–MS grade, Thermo Scientific Pierce, Cat. No. 13454279) were purchased from Fisher Chemicals. HeLa protein digest standard (Thermo Scientific Pierce, Cat. No. 88328) and yeast digest standard (Thermo Scientific Pierce, Cat. No. A47951) were purchased from Thermo Scientific. MassPREP E. coli digest standard (Cat. No. 186003196) was purchased from Waters. Sequence grade trypsin (Cat. No. V5113) were purchased from Promega.

Mouse treatment and tissue preparation

The research complies with all relevant ethical regulations: MD Anderson Cancer Center IACUC-approved mouse protocol 00001658-RN02. NSG mice were treated with PBS (vehicle), 20,000 U/kg $ASNase^{WT}$ (Spectrila®) qd for 8 d, or 20,000 U/kg $ASNase^{Q59L}$ qd for 8 d. We previously found the selected doses of $ASNase^{WT}$ and $ASNase^{Q59L}$ to be curative and ineffective, respectively, against a mouse model of ALL(*34*). *Escherichia coli* L-asparaginase II (ASNase) recombinant proteins were produced as described previously(*34, 35*). Treatments were administered intraperitoneally (IP) immediately above the hind leg. Treatment volume was 0.1 mL. Biological samples were collected at t = 0, 1, 3, 5, 8 d (n=3 mice per time point per treatment group). Prior to tissue collection, each mouse was euthanized using a CO2 chamber. The abdominal cavity was opened and perfused with 50 mL pre-cooled phosphate buffered saline. A total of 507 organs were dissected, snap-frozen in liquid nitrogen, and stored at −80°C.

Protein extraction and digestion

10 mg of each tissue sample was resuspended in ice-cold protein extraction buffer containing 4 M urea and 50 mM NH_4HCO_3. Homogenization was performed using a ceramic bead kit (Bertin Technologies Cat. No.CK28-R) with an automated homogenizer (Precellys 24 with Cryolys adapter, Bertin Technologies) with 2 × 10 s pulses at 5,000 rpm. Homogenates were clarified by centrifugation for 10 min at 10,000 g at 4°C, and protein concentration was determined by the BCA method. Proteins in the solution were denatured by boiling at 95°C for 5 min.

For standard sample preparation workflow, 20 µg protein was diluted to 50 µL with 50 mM NH_4HCO_3. Samples were digested by adding 1 µL 400 ng/µL trypsin (Promega) and incubated at 37°C overnight unless otherwise specified. Samples were acidified with formic acid at ~0.1% (v/v) final concentration by adding 0.5 µL 10% formic acid in water and centrifuged at 10,000 g for 10 min at 4°C. The supernatant was desalted using BioPureSPN Mini PROTO 300 C18 column (The Nest Group, Cat. No. HUM S18V), dried in vacuum and stored at -80°C until analysis.

For high-throughput sample preparation method, 20 µg of protein samples were diluted to 50 µL by adding 50 mM NH4HCO3 in the 96 AFA-TUBE TPX plate (Covaris, Cat. No. 520291) and then add 1 µL 400 ng/µL trypsin (Promega). The sample solutions were incubated with sonication at 37 °C for 4 hours using R230 Focused-Ultrasonicator (Covaris, Cat. No. 500620). Digested samples in 96-well plates were acidified with formic acid at ~1% (v/v) final concentration by adding 0.5 µL 10% formic acid in water and transferred to Evotip Pure 96-tip racks (Evosep, Cat. No. EV2013) for desalting. The desalted peptide samples were transferred to the Thermo Scientific™ SureSTART™ Level 2 WebSeal™ 96-Well Microtiter Plates (Thermo Scientific, Cat. No. 60180-P210B), dried in vacuum and stored at -80 °C until analysis.

LC–MS/MS analysis

LC–MS/MS analysis were performed using Orbitrap Astral mass spectrometer coupled with Vanquish Neo UHPLC system (Thermo Fisher Scientific). The vacuum dried peptide samples were resuspended with 0.1% of formic acid. Peptides were separated using an Evosep endurance

column (Evosep, Cat. No. EV1107, 150 µm × 4 cm) at a flow rate of 5 µL/min. Peptides were chromatographically separated using a linear gradient of solvent B (0.1% formic acid in ACN) and solvent A (0.1% formic acid in water). Linear gradients were as follows: from 10% to 38% of solvent B 1.8 min, 38% to 100% of solvent B from 1.8 to 1.9 min, 100% B from 1.9 to 2 min. For the original DIA method on the Orbitrap Astral MS, MS1 spectra were collected in the Orbitrap every 0.6 s at a resolution of 240,000. The full scan range was 380-980 m/z unless otherwise specified. The MS1 normalized AGC target was set to 500% with a maximum injection time of 5 ms. DIA MS2 scans were acquired in the Astral analyzer over a range of 380-980 m/z with a normalized AGC target of 500% and a maximum injection time of 3.5 ms and an HCD collision energy setting of 25%. Window placement optimization was turned on. The isolation window was set at 2 Th without window overlap. For the optimized DIA method, scan range was changed to 495-745 m/z. Isolation window was set at 1 Th without window overlap. The maximum injection time of MS2 was set at 2.5 ms.

MS data analysis

Raw files from DIA experiments were analyzed in DIA-NN 1.8.1(*12*). The spectral library was generated from a mouse reference database (UniProt 2024 release, 21,709 sequences) allowing N-term M excision and 1 missed cleavage. The DIA-NN search included the following settings: Protein inference = 'Genes', Neural network classifier = 'Single-pass mode', Quantification strategy = 'Robust LC (high precision)', Cross-run normalization = 'RT-dependent', Library Generation = 'Smart Profiling' and Speed and RAM usage = 'Optimal results'. Mass accuracy and MS1 accuracy were set to 0 for automatic inference. 'No share spectra', 'Heuristic protein inference' and 'MBR' were checked. The output results from DIA-NN were filtered for Q.Value <=0.01 and PG.Qvalue <=0.01. DIA-NN R package was used for protein quantitation using MaxLFQ algorithm.

Analysis of metabolites

Metabolites profiling was conducted on snap-frozen tissue samples by ultra-high-resolution mass spectrometry. Approximately 20–30 mg of each sample was pulverized in liquid nitrogen and then homogenized with Precellys Tissue Homogenizer.

Metabolites were extracted using ice-cold 0.1% ammonium hydroxide in an 80/20 (v/v) methanol/water solution. The extracts were then centrifuged at 17,000 g for 5 minutes at 4°C, and the supernatants were transferred to clean tubes. The solvents were evaporated under nitrogen to dryness. The dried extracts were reconstituted in deionized water, and 5 µL was injected for analysis by ion chromatography (IC)-mass spectrometry (MS). IC mobile phase A (MPA) was water, and mobile phase B (MPB) was water containing 100 mM KOH. The analysis was performed using a Thermo Scientific Dionex ICS-5000+ capillary IC system with a Thermo IonPac AS11 column (4 µm particle size, 250 × 2 mm). The column compartment was maintained at 30°C, and the autosampler tray was kept at 4°C. The IC flow rate was 350 µL/min with the following gradient conditions: starting at 1 mM KOH, increasing to 35 mM over 25 minutes, further increasing to 99 mM over 39 minutes, and holding at 99 mM for 10 minutes. To enhance desolvation for better sensitivity, methanol was delivered via an external pump and mixed with the post-column eluent using a low dead volume mixing tee. Data acquisition was performed with a Thermo Orbitrap Fusion Tribrid Mass Spectrometer in ESI negative ionization mode with a resolution of 240,000.

For amino acid analysis, samples were extracted using 1 mL of ice-cold 90/10 (v/v) acetonitrile/water containing 0.1% formic acid. The extracts were centrifuged at 17,000g for 5 min at 4°C, and the supernatants were transferred to clean tubes. The solvent was evaporated under nitrogen to dryness. The dried extracts were reconstituted in 90/10 acetonitrile/water with 1%

formic acid, and 10 µL was injected for analysis by liquid chromatography (LC)-MS. LC mobile phase A (MPA; weak) was acetonitrile containing 1% formic acid, and mobile phase B (MPB; strong) was water containing 50 mM ammonium formate. The analysis was preformed using Thermo Vanquish LC system equipped with an Imtakt Intrada Amino Acid column (3 µm particle size, 150 × 2.1 mm), maintained at 30°C. The autosampler tray was kept to 4°C. The flow rate was 300 µL/min. The gradient conditions were as follows: initial 15% MPB, increasing to 30% MPB at 20 min, further increasing to 95% MPB at 30 min, holding at 95% MPB for 10 min, and then returning to the initial conditions for equilibration over 10 min. The total run time was 50 min. Data acquisition was performed with a Thermo Orbitrap Fusion Tribrid mass spectrometer in ESI-positive ionization mode at a resolution of 240,000. Raw data files were analyzed using Thermo Trace Finder software. Peaks with a signal-to-noise ratio <3 were considered undetected.

References

1. L. L. Miller, C. G. Bly, M. L. Watson, W. F. Bale, The Dominant Role of the Liver in Plasma Protein Synthesis - a Direct Study of the Isolated Perfused Rat Liver with the Aid of Lysine-Epsilon C-14. *J Exp Med* **94**, 431-453 (1951).
2. I. M. Michelozzi *et al.*, Acute myeloid leukaemia niche regulates response to L-asparaginase. *Br J Haematol* **186**, 420-430 (2019).
3. L. Deng *et al.*, p53-mediated control of aspartate-asparagine homeostasis dictates LKB1 activity and modulates cell survival. *Nat Commun* **11**, 1755 (2020).
4. A. Agrawal *et al.*, WikiPathways 2024: next generation pathway database. *Nucleic Acids Res* **52**, D679-D689 (2024).
5. M. Yu *et al.*, L-asparaginase inhibits invasive and angiogenic activity and induces autophagy in ovarian cancer. *J Cell Mol Med* **16**, 2369-2378 (2012).
6. Y. Zhu, K. Hoshitsuki, C. Fernandez, Asparagine depletion by the antileukemic agent PEGylated asparaginase induces hepatic stellate cell activation and fibrosis. *Journal of Pharmacology and Experimental Therapeutics* **385**, (2023).
7. V. L. Albaugh, K. Mukherjee, A. Barbul, Proline Precursors and Collagen Synthesis: Biochemical Challenges of Nutrient Supplementation and Wound Healing. *J Nutr* **147**, 2011-2017 (2017).
8. M. K. Jena, J. Janjanam, Role of extracellular matrix in breast cancer development: a brief update. *F1000Res* **7**, 274 (2018).
9. L. Hinze *et al.*, Synthetic Lethality of Wnt Pathway Activation and Asparaginase in Drug-Resistant Acute Leukemias. *Cancer Cell* **35**, 664-676 e667 (2019).
10. C. Rizzari *et al.*, Asparagine levels in the cerebrospinal fluid of children with acute lymphoblastic leukemia treated with pegylated-asparaginase in the induction phase of the AIEOP-BFM ALL 2009 study. *Haematologica* **104**, 1812-1821 (2019).
11. M. Y. Hamdan, E. P. Frenkel, R. Bick, L-asparaginase-provoked seizures as singular expression of central nervous toxicity. *Clinical and Applied Thrombosis-Hemostasis* **6**, 234-238 (2000).
12. V. Demichev, C. B. Messner, S. I. Vernardis, K. S. Lilley, M. Ralser, DIA-NN: neural networks and interference correction enable deep proteome coverage in high throughput. *Nature methods* **17**, 41-44 (2020).
13. M. Mann, C. Kumar, W. F. Zeng, M. T. Strauss, Artificial intelligence for proteomics and biomarker discovery. *Cell Syst* **12**, 759-770 (2021).
14. S. Gessulat *et al.*, Prosit: proteome-wide prediction of peptide tandem mass spectra by deep learning. *Nat Methods* **16**, 509-518 (2019).
15. A. Martinez-Val, D. B. Bekker-Jensen, A. Hogrebe, J. V. Olsen, Data Processing and Analysis for DIA-Based Phosphoproteomics Using Spectronaut. *Proteomics Data Analysis* **2361**, 95-107 (2021).
16. R. Lou *et al.*, Benchmarking commonly used software suites and analysis workflows for DIA proteomics and phosphoproteomics. *Nat Commun* **14**, 94 (2023).
17. A. Shevchenko, H. Tomas, J. Havlis, J. V. Olsen, M. Mann, In-gel digestion for mass spectrometric characterization of proteins and proteomes. *Nat Protoc* **1**, 2856-2860 (2006).
18. J. R. Wisniewski, A. Zougman, N. Nagaraj, M. Mann, Universal sample preparation method for proteome analysis. *Nat Methods* **6**, 359-362 (2009).
19. N. A. Kulak, G. Pichler, I. Paron, N. Nagaraj, M. Mann, Minimal, encapsulated proteomic-sample processing applied to copy-number estimation in eukaryotic cells. *Nat Methods* **11**, 319-324 (2014).
20. X. Cai *et al.*, High-throughput proteomic sample preparation using pressure cycling technology. *Nat Protoc* **17**, 2307-2325 (2022).

326 21. G. P. Pujari *et al.*, A High-Throughput Workflow for FFPE Tissue Proteomics. *J Am Soc Mass*
327 *Spectrom* **34**, 1225-1229 (2023).
328 22. A. H. Kverneland *et al.*, Fully Automated Workflow for Integrated Sample Digestion and Evotip
329 Loading Enabling High-Throughput Clinical Proteomics. *Mol Cell Proteomics* **23**, 100790 (2024).
330 23. J. Adachi *et al.*, Improved Proteome and Phosphoproteome Analysis on a Cation Exchanger by a
331 Combined Acid and Salt Gradient. *Anal Chem* **88**, 7899-7903 (2016).
332 24. Y. Wang *et al.*, Reversed-phase chromatography with multiple fraction concatenation strategy for
333 proteome profiling of human MCF10A cells. *Proteomics* **11**, 2019-2026 (2011).
334 25. K. Horie *et al.*, Hydrophilic interaction chromatography using a meter-scale monolithic silica
335 capillary column for proteomics LC-MS. *Anal Chem* **86**, 3817-3824 (2014).
336 26. F. Meier, P. E. Geyer, S. Virreira Winter, J. Cox, M. Mann, BoxCar acquisition method enables
337 single-shot proteomics at a depth of 10,000 proteins in 100 minutes. *Nat Methods* **15**, 440-448
338 (2018).
339 27. Y. Kawashima *et al.*, Single-Shot 10K Proteome Approach: Over 10,000 Protein Identifications by
340 Data-Independent Acquisition-Based Single-Shot Proteomics with Ion Mobility Spectrometry. *J*
341 *Proteome Res* **21**, 1418-1427 (2022).
342 28. R. Konno *et al.*, Ultra-deep proteomics by Thin-diaPASEF with a 60-cm long column system. *bioRxiv*,
343 2024.2004.2026.591246 (2024).
344 29. L. R. Serrano *et al.*, The One Hour Human Proteome. *Mol Cell Proteomics* **23**, 100760 (2024).
345 30. U. H. Guzman *et al.*, Ultra-fast label-free quantification and comprehensive proteome coverage
346 with narrow-window data-independent acquisition. *Nat Biotechnol*, (2024).
347 31. H. I. Stewart *et al.*, Parallelized Acquisition of Orbitrap and Astral Analyzers Enables High-
348 Throughput Quantitative Analysis. *Anal Chem* **95**, 15656-15664 (2023).
349 32. M. Ishikawa *et al.*, Optimization of Ultrafast Proteomics Using an LC-Quadrupole-Orbitrap Mass
350 Spectrometer with Data-Independent Acquisition. *J Proteome Res* **21**, 2085-2093 (2022).
351 33. L. Szyrwiel, C. Gille, M. Mulleder, V. Demichev, M. Ralser, Fast proteomics with dia-PASEF and
352 analytical flow-rate chromatography. *Proteomics* **24**, e2300100 (2024).
353 34. W. K. Chan *et al.*, Glutaminase Activity of L-Asparaginase Contributes to Durable Preclinical
354 Activity against Acute Lymphoblastic Leukemia. *Mol Cancer Ther* **18**, 1587-1592 (2019).
355 35. W. K. Chan *et al.*, The glutaminase activity of L-asparaginase is not required for anticancer activity
356 against ASNS-negative cells. *Blood* **123**, 3596-3606 (2014).

357

Supplementary figure legends

Supplementary Fig. 1 a, Comparison of the number of identified protein groups between this study and a reported cutting-edge result of MS methods with one-minute LC gradient. **b**, Comparison of the number of identified protein groups between this study and a reported cutting-edge result of MS methods with two-minute LC gradient. **c,** The number of peptides identified using standard and high-throughput sample preparation workflows from brain, kidney, and lung, respectively. **d,** Overview of the average number of peptides identified in 13 mouse tissues.

Supplementary Fig. 2, **a,** Illustration of the binding proteins for four amino acids (ASN, ASP, GLN, and GLU) retrieved from the BioGRID online database (http://thebiogrid.org). **b,** Heatmap overview of the dynamic changes in protein levels of the binding proteins for ASN, ASP, GLN, and GLU following ASNase^{WT} or ASNase^{Q59L} treatment across all the tested tissues. Protein expression levels following ASNase^{WT} or ASNase^{Q59L} treatment were compared to PBS-treated controls, with the Log2 fold change values presented.

Supplementary Fig. 3, **a-d**, Volcano plots showing differential protein expression levels in SQWAT tissue following ASNase^{WT} treatment at 1d (**a**), 3d (**b**), 5d (**c**), and 8d (**d**). The x-axis represents the Log2 fold changes in protein expression between ASNase^{WT} and PBS-treated controls, while the y-axis indicates the -Log10 of the p-value. Proteins with a fold change greater than 2 and a p-value less than 0.05 are highlighted as significantly upregulated (red) or downregulated (blue). Upregulated or downregulated protein numbers are shown. **e-h**, Similar volcano plots showing differential protein expression levels in SQWAT tissue following ASNase^{Q59L} treatment at 1 day (**e**), 3 days (**f**), 5 days (**g**), and 8 days (**h**). **i**,**j**, KEGG pathway analysis of the upregulated (**i**) or downregulated (**j**) proteins following ASNase^{WT} treatment in the SQWAT tissue. **k**,**l**, KEGG pathway analysis of the upregulated (**k**) or downregulated (**l**) proteins following ASNase^{Q59L} treatment in the SQWAT tissue.

Supplementary Fig. 4, **a-d**, Volcano plots showing differential protein expression levels in lung tissue following ASNase^{WT} treatment at 1d (**a**), 3d (**b**), 5d (**c**), and 8d (**d**). The x-axis represents the Log2 fold changes in protein expression between ASNase^{WT} and PBS-treated controls, while the y-axis indicates the -Log10 of the p-value. Proteins with a fold change greater than 2 and a p-value less than 0.05 are highlighted as significantly upregulated (red) or downregulated (blue). Upregulated or downregulated protein numbers are shown. **e-h**, Similar volcano plots showing differential protein expression levels in lung tissue following ASNase^{Q59L} treatment at 1 day (**e**), 3 days (**f**), 5 days (**g**), and 8 days (**h**). **i**,**j**, KEGG pathway analysis of the upregulated (**i**) or downregulated (**j**) proteins following ASNase^{WT} treatment in the lung tissue. **k**,**l**, KEGG pathway analysis of the upregulated (**k**) or downregulated (**l**) proteins following ASNase^{Q59L} treatment in the lung tissue.

Supplementary Fig. 5, **a-d**, Volcano plots showing differential protein expression levels in spleen tissue following ASNase^{WT} treatment at 1d (**a**), 3d (**b**), 5d (**c**), and 8d (**d**). The x-axis represents the Log2 fold changes in protein expression between ASNase^{WT} and PBS-treated controls, while the y-axis indicates the -Log10 of the p-value. Proteins with a fold change greater than 2 and a p-value less than 0.05 are highlighted as significantly upregulated (red) or downregulated (blue). Upregulated or downregulated protein numbers are shown. **e-h**, Similar volcano plots showing differential protein expression levels in spleen tissue following ASNase^{Q59L} treatment at 1 day (**e**), 3 days (**f**), 5 days (**g**), and 8 days (**h**). **i**,**j**, KEGG pathway analysis of the upregulated (**i**) or downregulated (**j**) proteins following ASNase^{WT} treatment in the spleen tissue. **k**,**l**, KEGG pathway analysis of the upregulated (**k**) or downregulated (**l**) proteins following ASNase^{Q59L} treatment in the spleen tissue.

Supplementary Fig. 6, **a-d**, Volcano plots showing differential protein expression levels in liver tissue following ASNase^{WT} treatment at 1d (**a**), 3d (**b**), 5d (**c**), and 8d (**d**). The x-axis represents the Log2 fold changes in protein expression between ASNase^{WT} and PBS-treated controls, while the y-axis indicates the -Log10 of the p-value. Proteins with a fold change greater than 2 and a p-value less than 0.05 are highlighted as significantly upregulated (red) or downregulated (blue). Upregulated or downregulated protein numbers are shown. **e-h**, Similar volcano plots showing differential protein expression levels in liver tissue following ASNase^{Q59L} treatment at 1 day (**e**), 3 days (**f**), 5 days (**g**), and 8 days (**h**). **i**,**j**, KEGG pathway analysis of the upregulated (**i**) or downregulated (**j**) proteins following ASNase^{WT} treatment in the liver tissue. **k**,**l**, KEGG pathway analysis of the upregulated (**k**) or downregulated (**l**) proteins following ASNase^{Q59L} treatment in the liver tissue.

Supplementary Fig. 7, **a-d**, Volcano plots showing differential protein expression levels in brain tissue following ASNase^{WT} treatment at 1d (**a**), 3d (**b**), 5d (**c**), and 8d (**d**). The x-axis represents the Log2 fold changes in protein expression between ASNase^{WT} and PBS-treated controls, while the y-axis indicates the -Log10 of the p-value. Proteins with a fold change greater than 2 and a p-value less than 0.05 are highlighted as significantly upregulated (red) or downregulated (blue). Upregulated or downregulated protein numbers are shown. **e-h**, Similar volcano plots showing differential protein expression levels in brain tissue following ASNase^{Q59L} treatment at 1 day (**e**), 3 days (**f**), 5 days (**g**), and 8 days (**h**). **i**,**j**, KEGG pathway analysis of the upregulated (**i**) or downregulated (**j**) proteins following ASNase^{WT} treatment in the brain tissue. **k**,**l**, KEGG pathway analysis of the upregulated (**k**) or downregulated (**l**) proteins following ASNase^{Q59L} treatment in the brain tissue.

Supplementary Fig. 8, **a-d**, Volcano plots showing differential protein expression levels in bone marrow tissue following ASNase^{WT} treatment at 1d (**a**), 3d (**b**), 5d (**c**), and 8d (**d**). The x-axis represents the Log2 fold changes in protein expression between ASNase^{WT} and PBS-treated controls, while the y-axis indicates the -Log10 of the p-value. Proteins with a fold change greater than 2 and a p-value less than 0.05 are highlighted as significantly upregulated (red) or downregulated (blue). Upregulated or downregulated protein numbers are shown. **e-h**, Similar volcano plots showing differential protein expression levels in bone marrow tissue following ASNase^{Q59L} treatment at 1 day (**e**), 3 days (**f**), 5 days (**g**), and 8 days (**h**). **i**,**j**, KEGG pathway analysis of the upregulated (**i**) or downregulated (**j**) proteins following ASNase^{WT} treatment in the bone marrow tissue. **k**,**l**, KEGG pathway analysis of the upregulated (**k**) or downregulated (**l**) proteins following ASNase^{Q59L} treatment in the bone marrow tissue.

Supplementary Fig. 9, **a-d**, Volcano plots showing differential protein expression levels in kidney tissue following ASNase^{WT} treatment at 1d (**a**), 3d (**b**), 5d (**c**), and 8d (**d**). The x-axis represents the Log2 fold changes in protein expression between ASNase^{WT} and PBS-treated controls, while the y-axis indicates the -Log10 of the p-value. Proteins with a fold change greater than 2 and a p-value less than 0.05 are highlighted as significantly upregulated (red) or downregulated (blue). Upregulated or downregulated protein numbers are shown. **e-h**, Similar volcano plots showing differential protein expression levels in kidney tissue following ASNase^{Q59L} treatment at 1 day (**e**), 3 days (**f**), 5 days (**g**), and 8 days (**h**). **i**,**j**, KEGG pathway analysis of the upregulated (**i**) or downregulated (**j**) proteins following ASNase^{WT} treatment in the kidney tissue. **k**,**l**, KEGG pathway analysis of the upregulated (**k**) or downregulated (**l**) proteins following ASNase^{Q59L} treatment in the kidney tissue.

Supplementary Fig. 10, **a-d**, Volcano plots showing differential protein expression levels in small intestine tissue following ASNase^{WT} treatment at 1d (**a**), 3d (**b**), 5d (**c**), and 8d (**d**). The x-axis represents the Log2 fold changes in protein expression between ASNase^{WT} and PBS-treated controls, while the y-axis indicates the -Log10 of the p-value. Proteins with a fold change greater

than 2 and a p-value less than 0.05 are highlighted as significantly upregulated (red) or downregulated (blue). Upregulated or downregulated protein numbers are shown. **e-h**, Similar volcano plots showing differential protein expression levels in small intestine tissue following ASNase^{Q59L} treatment at 1 day (**e**), 3 days (**f**), 5 days (**g**), and 8 days (**h**). **i**,**j**, KEGG pathway analysis of the upregulated (**i**) or downregulated (**j**) proteins following ASNase^{WT} treatment in the small intestine tissue. **k**,**l**, KEGG pathway analysis of the upregulated (**k**) or downregulated (**l**) proteins following ASNase^{Q59L} treatment in the small intestine tissue.

Supplementary Fig. 11, **a-d**, Volcano plots showing differential protein expression levels in large intestine tissue following ASNase^{WT} treatment at 1d (**a**), 3d (**b**), 5d (**c**), and 8d (**d**). The x-axis represents the Log2 fold changes in protein expression between ASNase^{WT} and PBS-treated controls, while the y-axis indicates the -Log10 of the p-value. Proteins with a fold change greater than 2 and a p-value less than 0.05 are highlighted as significantly upregulated (red) or downregulated (blue). Upregulated or downregulated protein numbers are shown. **e-h**, Similar volcano plots showing differential protein expression levels in large intestine tissue following ASNase^{Q59L} treatment at 1 day (**e**), 3 days (**f**), 5 days (**g**), and 8 days (**h**). **i**,**j**, KEGG pathway analysis of the upregulated (**i**) or downregulated (**j**) proteins following ASNase^{WT} treatment in the large intestine tissue. **k**,**l**, KEGG pathway analysis of the upregulated (**k**) or downregulated (**l**) proteins following ASNase^{Q59L} treatment in the large intestine tissue.

Supplementary Fig.12, **a-d**, Volcano plots showing differential protein expression levels in muscle tissue following ASNase^{WT} treatment at 1d (**a**), 3d (**b**), 5d (**c**), and 8d (**d**). The x-axis represents the Log2 fold changes in protein expression between ASNase^{WT} and PBS-treated controls, while the y-axis indicates the -Log10 of the p-value. Proteins with a fold change greater than 2 and a p-value less than 0.05 are highlighted as significantly upregulated (red) or downregulated (blue). Upregulated or downregulated protein numbers are shown. **e-h**, Similar volcano plots showing differential protein expression levels in muscle tissue following ASNase^{Q59L} treatment at 1 day (**e**), 3 days (**f**), 5 days (**g**), and 8 days (**h**). **i**,**j**, KEGG pathway analysis of the upregulated (**i**) or downregulated (**j**) proteins following ASNase^{WT} treatment in the muscle tissue. **k**,**l**, KEGG pathway analysis of the upregulated (**k**) or downregulated (**l**) proteins following ASNase^{Q59L} treatment in the muscle tissue.

Supplementary Fig.13, **a-d**, Volcano plots showing differential protein expression levels in GAT tissue following ASNase^{WT} treatment at 1d (**a**), 3d (**b**), 5d (**c**), and 8d (**d**). The x-axis represents the Log2 fold changes in protein expression between ASNase^{WT} and PBS-treated controls, while the y-axis indicates the -Log10 of the p-value. Proteins with a fold change greater than 2 and a p-value less than 0.05 are highlighted as significantly upregulated (red) or downregulated (blue). Upregulated or downregulated protein numbers are shown. **e-h**, Similar volcano plots showing differential protein expression levels in GAT tissue following ASNase^{Q59L} treatment at 1 day (**e**), 3 days (**f**), 5 days (**g**), and 8 days (**h**). **i**,**j**, KEGG pathway analysis of the upregulated (**i**) or downregulated (**j**) proteins following ASNase^{WT} treatment in the GAT tissue. **k**,**l**, KEGG pathway analysis of the upregulated (**k**) or downregulated (**l**) proteins following ASNase^{Q59L} treatment in the GAT tissue.

Supplementary Fig.14, **a-d**, Volcano plots showing differential protein expression levels in stomach tissue following ASNase^{WT} treatment at 1d (**a**), 3d (**b**), 5d (**c**), and 8d (**d**). The x-axis represents the Log2 fold changes in protein expression between ASNase^{WT} and PBS-treated controls, while the y-axis indicates the -Log10 of the p-value. Proteins with a fold change greater than 2 and a p-value less than 0.05 are highlighted as significantly upregulated (red) or downregulated (blue). Upregulated or downregulated protein numbers are shown. **e-h**, Similar volcano plots showing differential protein expression levels in stomach tissue following ASNase^{Q59L} treatment at 1 day (**e**), 3 days (**f**), 5 days (**g**), and 8 days (**h**). **i**,**j**, KEGG pathway

501 analysis of the upregulated (**i**) or downregulated (**j**) proteins following ASNase^{WT} treatment in the
502 stomach tissue. **k**,**l**, KEGG pathway analysis of the upregulated (**k**) or downregulated (**l**) proteins
503 following ASNase^{Q59L} treatment in the stomach tissue.

504 **Supplementary Fig.15**, **a-d**, Volcano plots showing differential protein expression levels in heart
505 tissue following ASNase^{WT} treatment at 1d (**a**), 3d (**b**), 5d (**c**), and 8d (**d**). The x-axis represents
506 the Log2 fold changes in protein expression between ASNase^{WT} and PBS-treated controls, while
507 the y-axis indicates the -Log10 of the p-value. Proteins with a fold change greater than 2 and a p-
508 value less than 0.05 are highlighted as significantly upregulated (red) or downregulated (blue).
509 Upregulated or downregulated protein numbers are shown. **e-h**, Similar volcano plots showing
510 differential protein expression levels in heart tissue following ASNase^{Q59L} treatment at 1 day (**e**),
511 3 days (**f**), 5 days (**g**), and 8 days (**h**). **i**,**j**, KEGG pathway analysis of the upregulated (**i**) or
512 downregulated (**j**) proteins following ASNase^{WT} treatment in the heart tissue. **k**,**l**, KEGG pathway
513 analysis of the upregulated (**k**) or downregulated (**l**) proteins following ASNase^{Q59L} treatment in
514 the heart tissue.

515 **Supplementary Fig. 16**, **a,** The dynamic regulation of indicated amino acid levels following 1, 3,
516 5, 8 days treatment with ASNase^{WT} or ASNase^{Q59L} treatment in the spleen. **b,** The dynamic
517 regulation of indicated amino acid levels following 1, 3, 5, 8 days treatment with ASNase^{WT} or
518 ASNase^{Q59L} treatment across all tested tissues.

519 **Supplementary Fig. 17**, **a**, Proteins that were upregulated or downregulated in the spleen
520 following ASNase^{WT} treatment were categorized. A heatmap was used to provide a global
521 overview of the dynamic changes in these proteins across all tested tissues. **b**, An enlarged view
522 of (**a**) highlighted proteins involved in lysosome, glutathione metabolism, ferroptosis, DNA
523 replication, ribosome and translation, and mitochondria.

524 **Supplementary Fig. 18**, **Landscape of tissue specific dysregulation pathways following**
525 **ASNase^{WT} treatment**

526 **a,** Proteins involved in the up-regulated ribosomal proteins and aminoacyl-tRNA biosynthesis in
527 the liver. **b,** Proteins involved in the up-regulated proteins involved in AMPK signaling pathway
528 and lysosomal cysteine proteases in the bone marrow. **c,** Proteins involved in the up-regulated
529 proteins involved in the PPRP signaling pathway and the ubiquitin mediated proteolysis in the
530 SWQAT. **d,** Proteins involved in the up-regulated proteins involved in PI3K-AKT signaling
531 pathway in the GAT. **e,** Proteins involved in the up-regulated proteins involved in the ECM-
532 receptor interaction and focal adhesion in multiple tissues including liver, lung, spleen, stomach,
533 and GAT. For visualization, the maximal log2 ratios (ASNase^{WT} vs PBS) from liver, lung, spleen,
534 stomach, or GAT were adopted for the heatmaps. **f,** Proteins involved in the up-regulated proteins
535 involved in ROS and oxidative phosphorylation pathway in the stomach. **g,** Proteins involved in
536 the up-regulated proteins involved in biosynthesis of amino acids pathway, biosynthesis of
537 unsaturated fatty acids pathway, and glutathione metabolism pathway in the kidney. **h,** Proteins
538 involved in the up-regulated proteins involved in mTOR signaling pathway, beta-Alanine
539 metabolism pathway, arginine and proline metabolism pathway and N-glycan biosynthesis
540 pathway in the small intestine. **j,** Proteins involved in the up-regulated proteins involved in
541 glutamatergic synapse and oxytocin signaling pathway in the brain. The maximal log2 ratios
542 (ASNase^{WT} vs PBS) from indicated tissues were adopted for the heatmaps unless otherwise
543 specified.

544 **Supplementary Fig. 19**, **a**, The MS intensity of 4-hydroxyproline in the liver under different
545 treatment conditions.

546

547 **Supplementary Table 1**, Protein groups and peptides identified using Evosep-Astral and Neo-
548 EV1107-Astral methods.

549 **Supplementary Table 2**, Protein groups and peptides identified using different MS2 maximum
550 injection time (IT) from 1 to 3.5 ms.

551 **Supplementary Table 3**, Protein groups and peptides identified using different mass ranges.

552 **Supplementary Table 4**, Protein groups and peptides identified using different isolation windows
553 from 0.8 to 2 Da.

554 **Supplementary Table 5**, Protein groups and peptides identified using different AGC values from
555 100 to 600.

556 **Supplementary Table 6**, Evaluation of the ultra-fast nDIA method with one to five minutes LC
557 gradients.

558 **Supplementary Table 7**, Evaluation of the quantitative performance of the ultra-fast nDIA method
559 with three-species samples mixed in various ratios.

560 **Supplementary Table 8**, Comparison of the protein and peptide identifications using different
561 digestion durations from 30 min to 15 h. To check the missed cleavage percentage, up to three
562 missed cleavage sites were allowed for this analysis.

563 **Supplementary Table 9**, Protein groups and peptides identified using the standard and high-
564 throughput sample preparation workflows.

565 **Supplementary Table 10**, Proteins identified in the large-scale mouse tissue proteomics datasets
566 including 507 tissue samples. P-values were calculated using student's t-test.

567 **Supplementary Table 11,** Differentially regulated proteins in each tissue following treatment of
568 ASNase for 1 to 8 days. For each protein, the fold change of the median intensity from ASNase
569 treated and PBS treated sample groups was calculated. Only proteins with a fold change >2 or
570 <0.5 and p-value <0.05 were selected as differential proteins.

571 **Supplementary Table 12,** Number of shared tissues for differential proteins. The differential
572 proteins identified in different time points (1 day, 3 days, 5 days, and 8 days) were merged for
573 each tissue type. The number of shared tissues means certain proteins were identified to be
574 differentially regulated in a certain number of tissues.

575 **Supplementary Table 13,** Functional clustering analysis of the differentially regulated proteins in
576 the SQWAT according to the online database DAVID (https://david.ncifcrf.gov/).

577 **Supplementary Table 14,** Functional clustering analysis of the differentially regulated proteins in
578 the GAT.

579 **Supplementary Table 15,** Functional clustering analysis of the differentially regulated proteins in
580 the lung.

581 **Supplementary Table 16,** Functional clustering analysis of the differentially regulated proteins in
582 the spleen.

583 **Supplementary Table 17,** Functional clustering analysis of the differentially regulated proteins in
584 the stomach.

585 **Supplementary Table 18,** Functional clustering analysis of the differentially regulated proteins in
586 the small intestine.

587 **Supplementary Table 19,** Functional clustering analysis of the differentially regulated proteins in
588 the large intestine.

589 **Supplementary Table 20,** Functional clustering analysis of the differentially regulated proteins in
590 the liver.

591 **Supplementary Table 21,** Functional clustering analysis of the differentially regulated proteins in
592 the kidney.

593 **Supplementary Table 22,** Functional clustering analysis of the differentially regulated proteins in
594 the heart.

595 **Supplementary Table 23,** Functional clustering analysis of the differentially regulated proteins in
596 the muscle.

597 **Supplementary Table 24,** Functional clustering analysis of the differentially regulated proteins in
598 the brain.

599 **Supplementary Table 25,** Functional clustering analysis of the differentially regulated proteins in
600 the bone marrow.

601 **Supplementary Table 26,** Metabolomics analysis of amino acid in the tissues.

602 **Supplementary Table 27,** Metabolomics analysis of polar metabolites in the tissues.
603

Supplementary Figure 1

Comparison with reported cutting-edge results of methods with one-minute and two-minute LC gradients

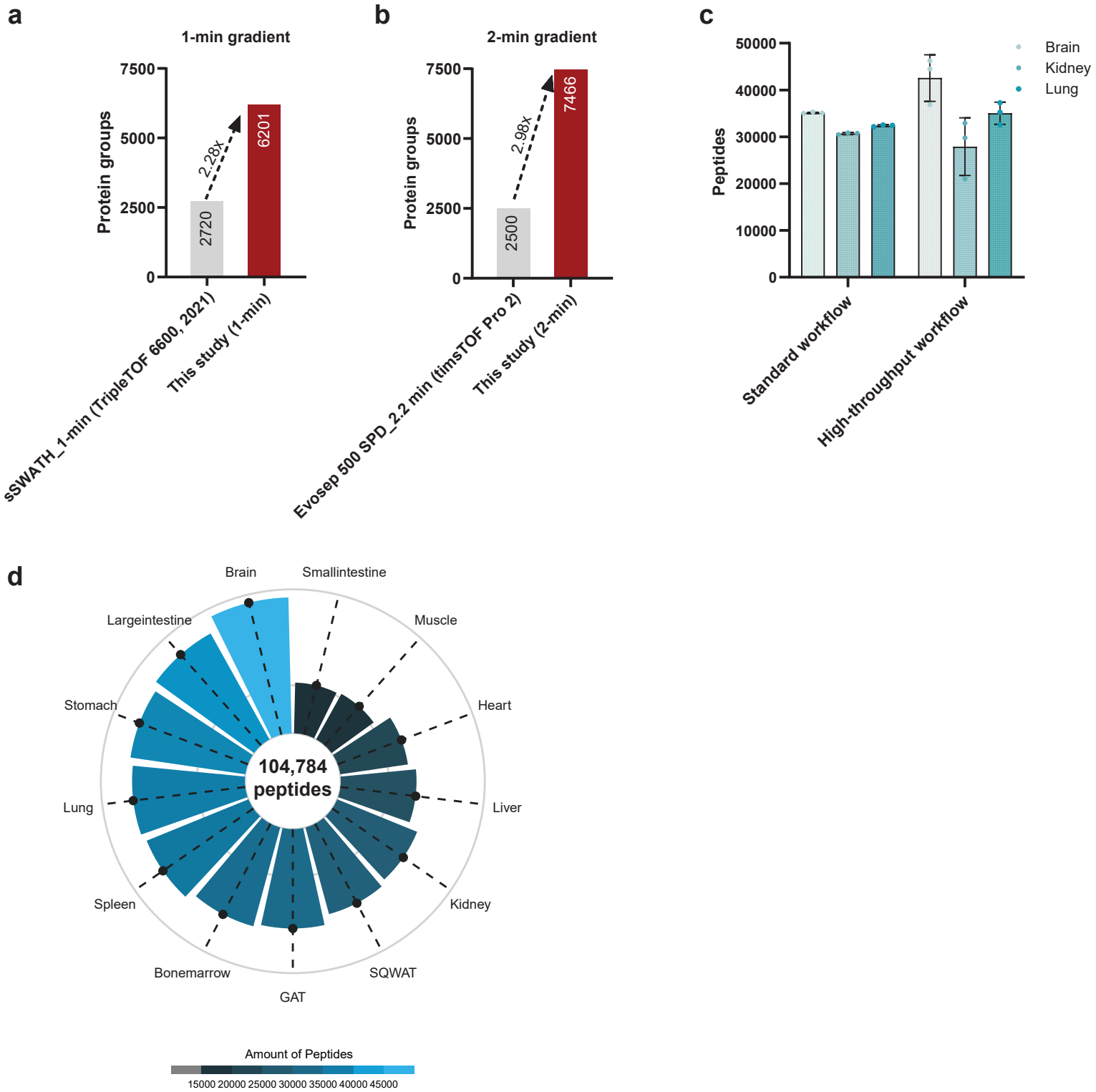

Supplementary Figure 2

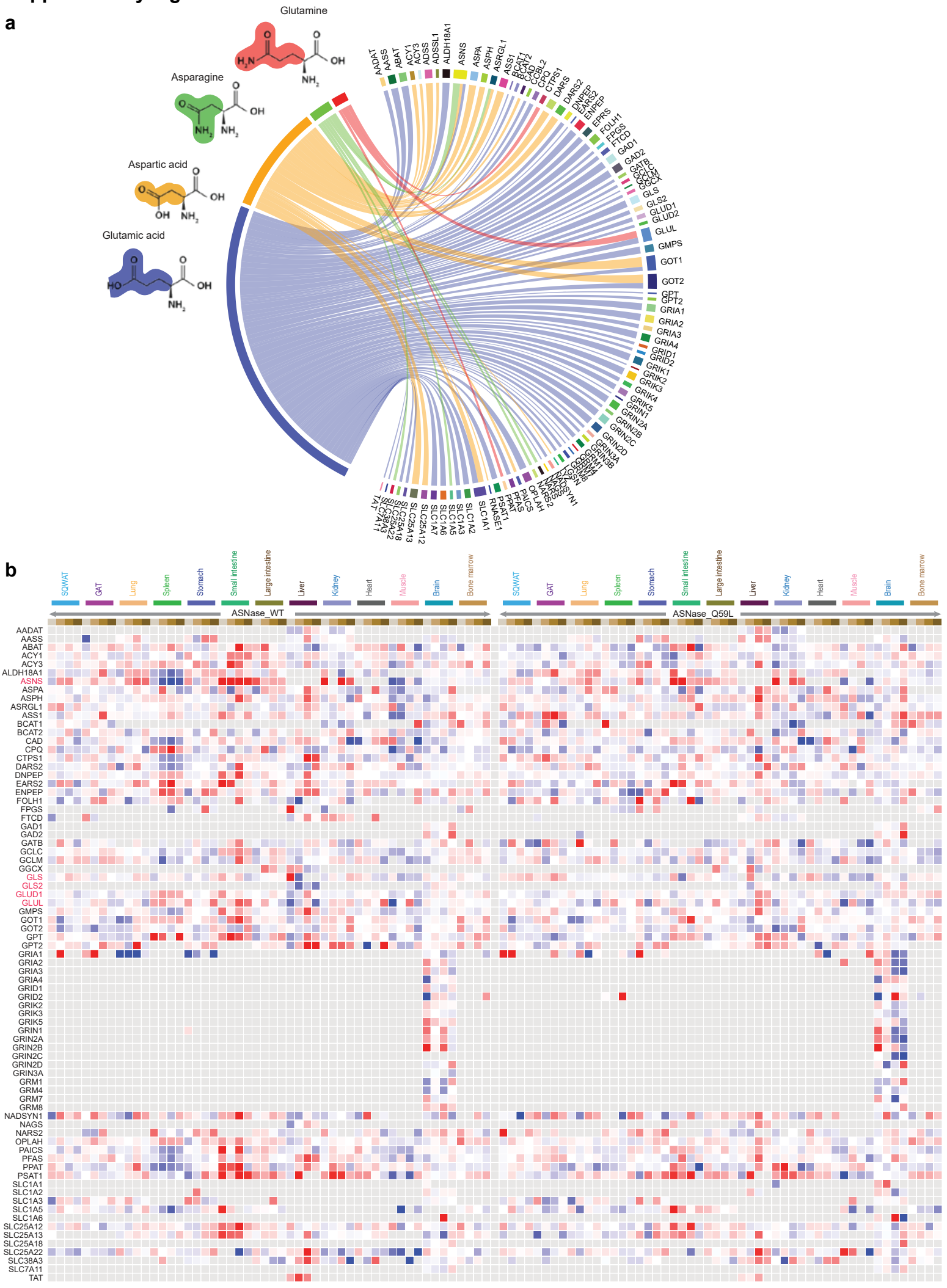

Supplementary Figure 3

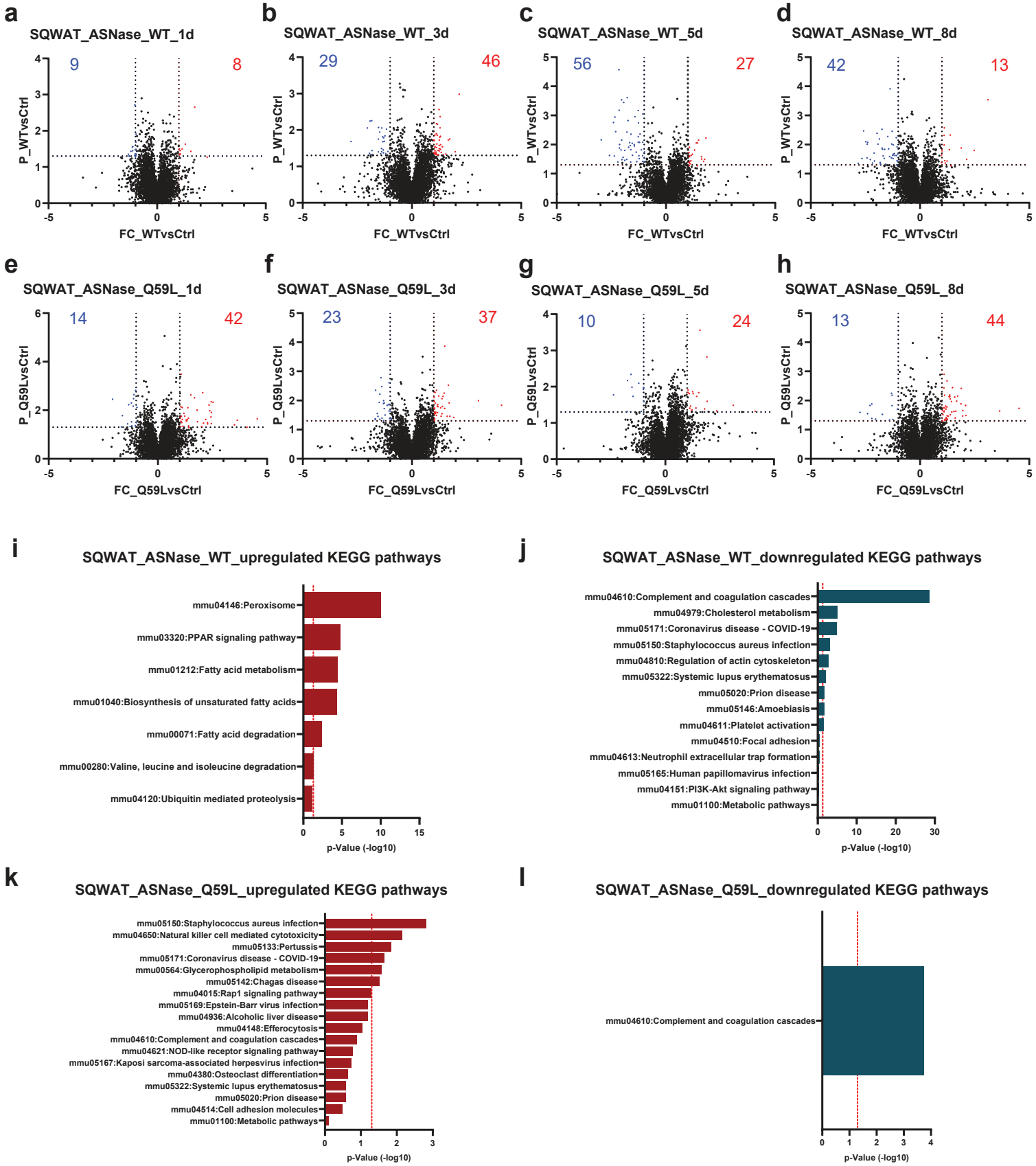

Supplementary Figure 4

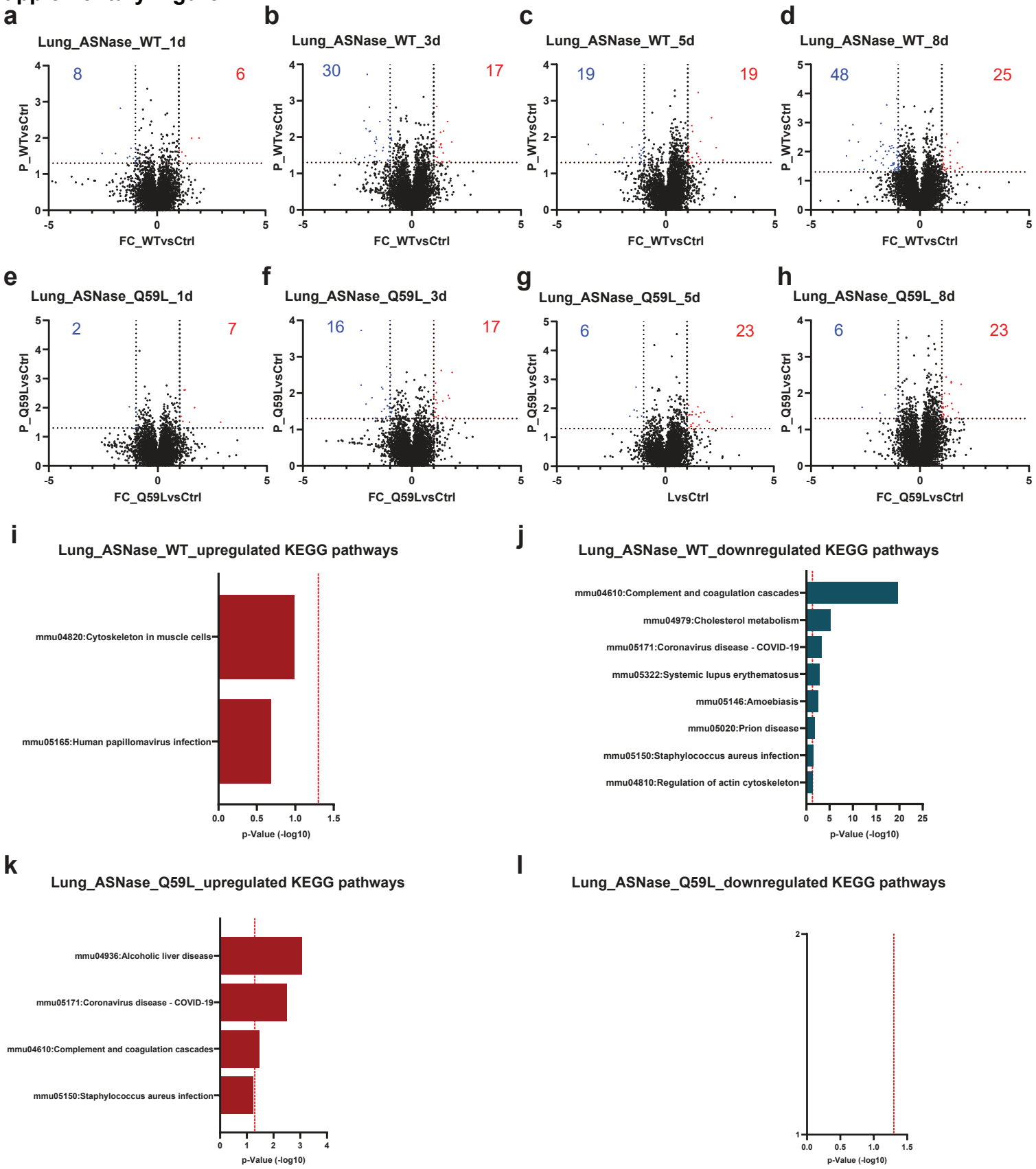

Supplementary Figure 5

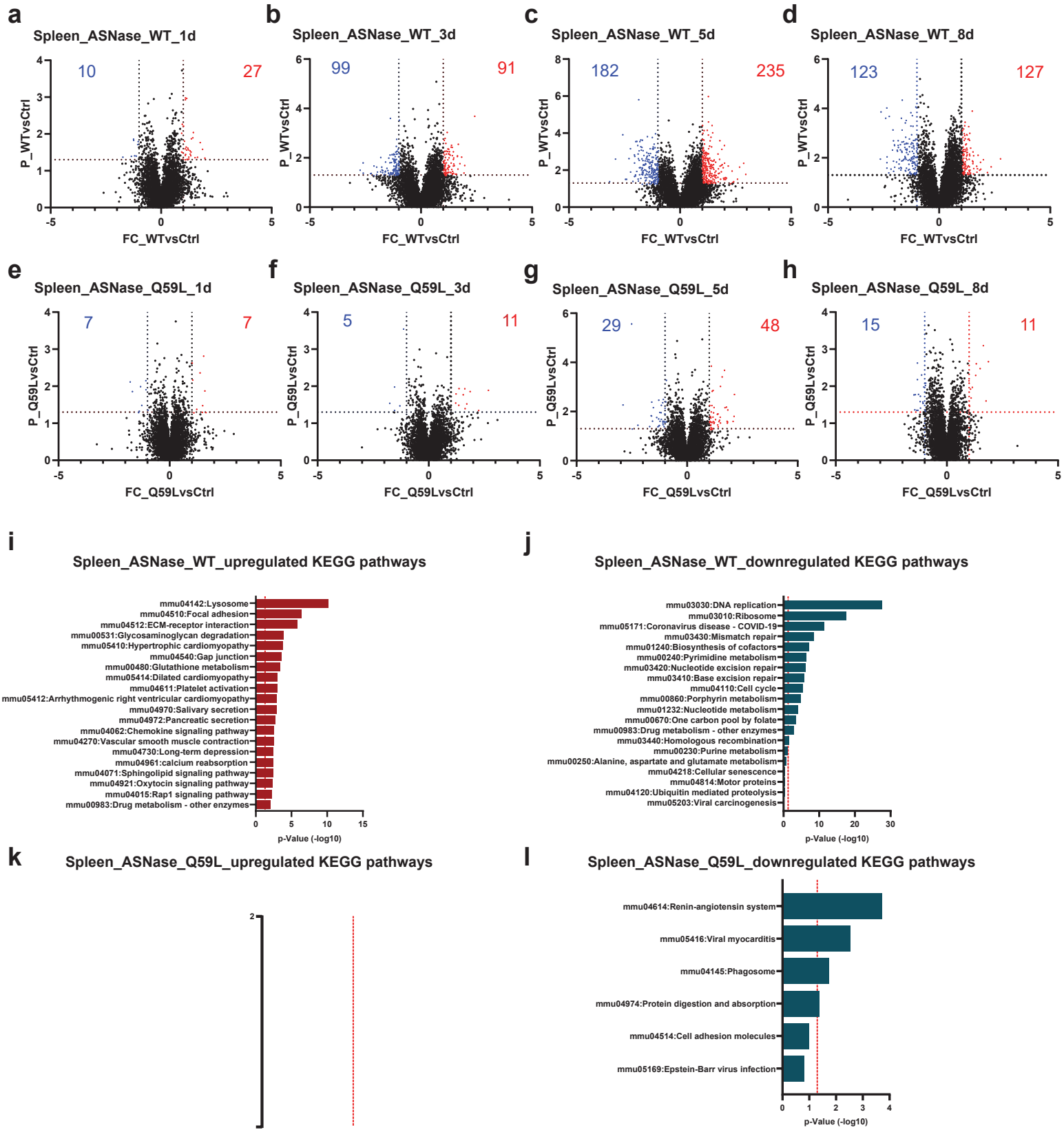

Supplementary Figure 6

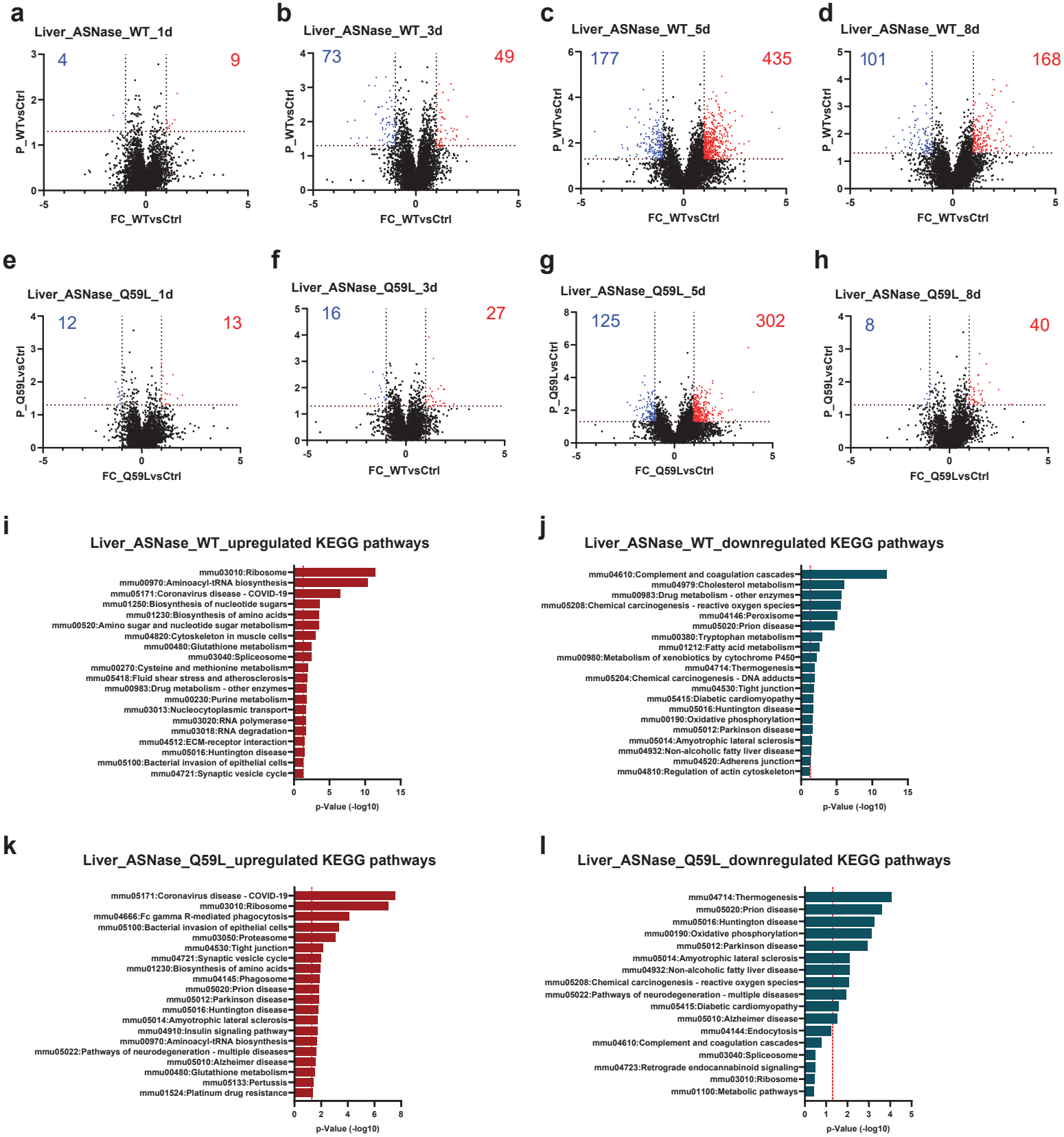

Supplementary Figure 7

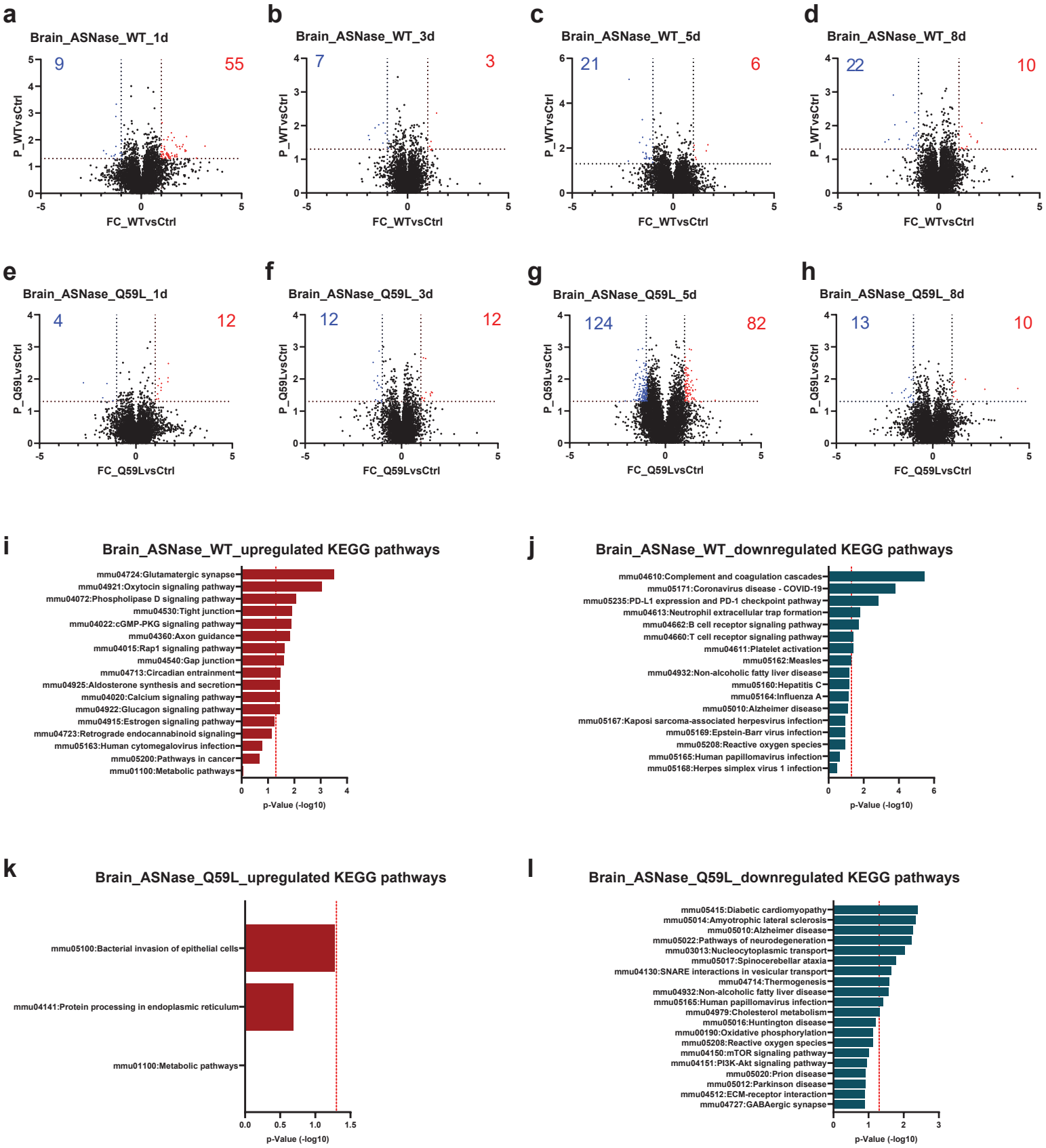

Supplementary Figure 8

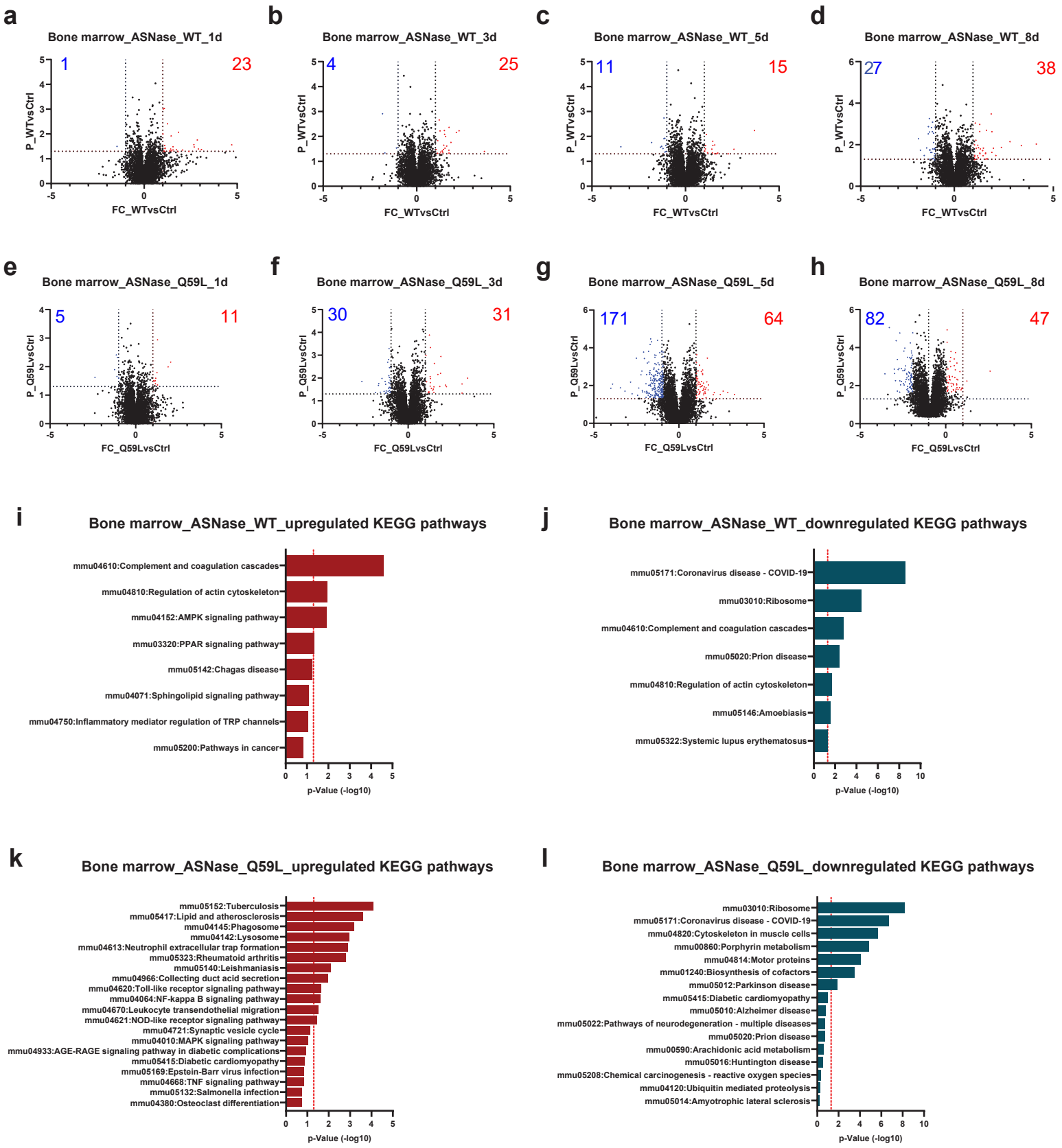

Supplementary Figure 9

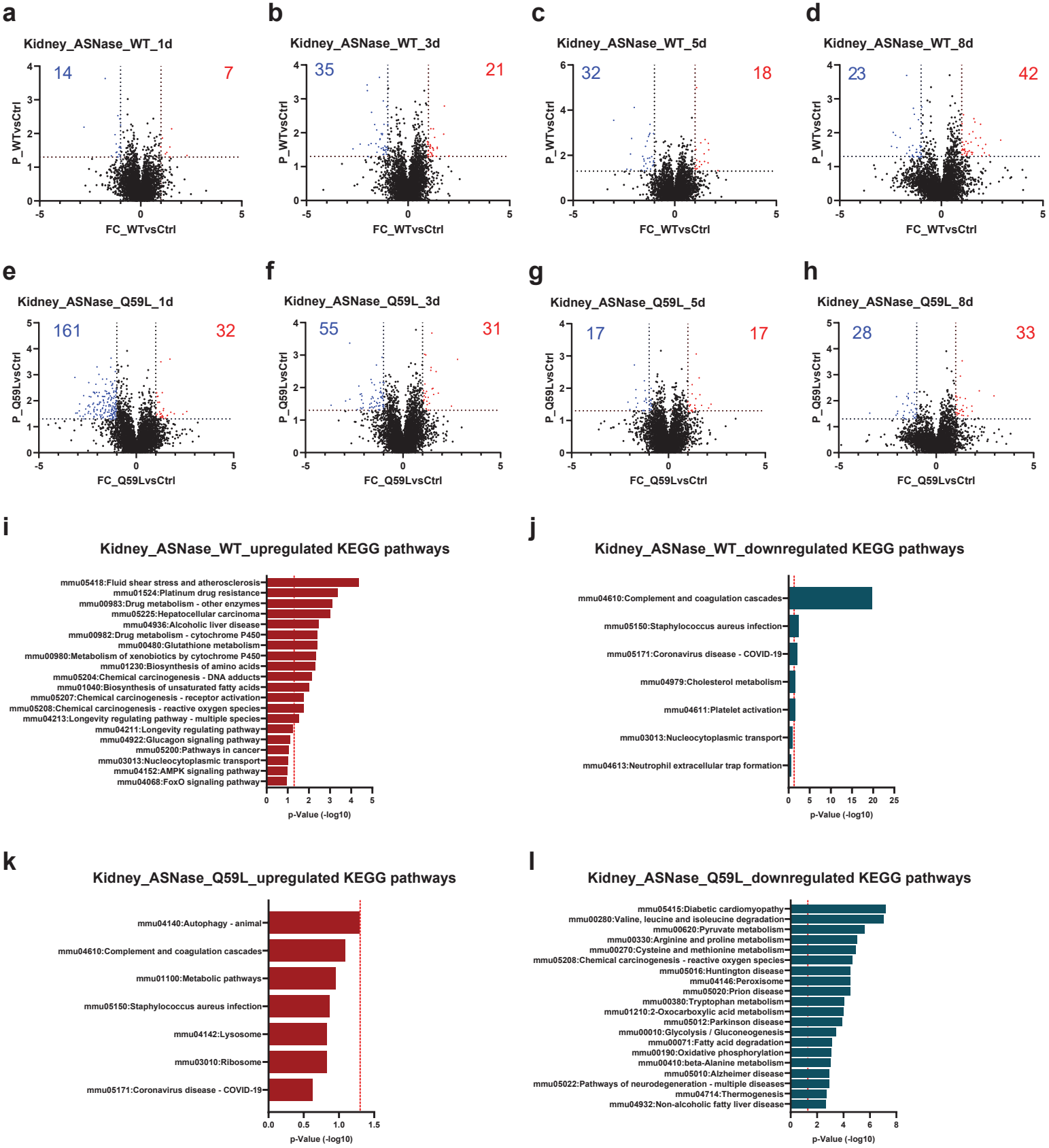

Supplementary Figure 10

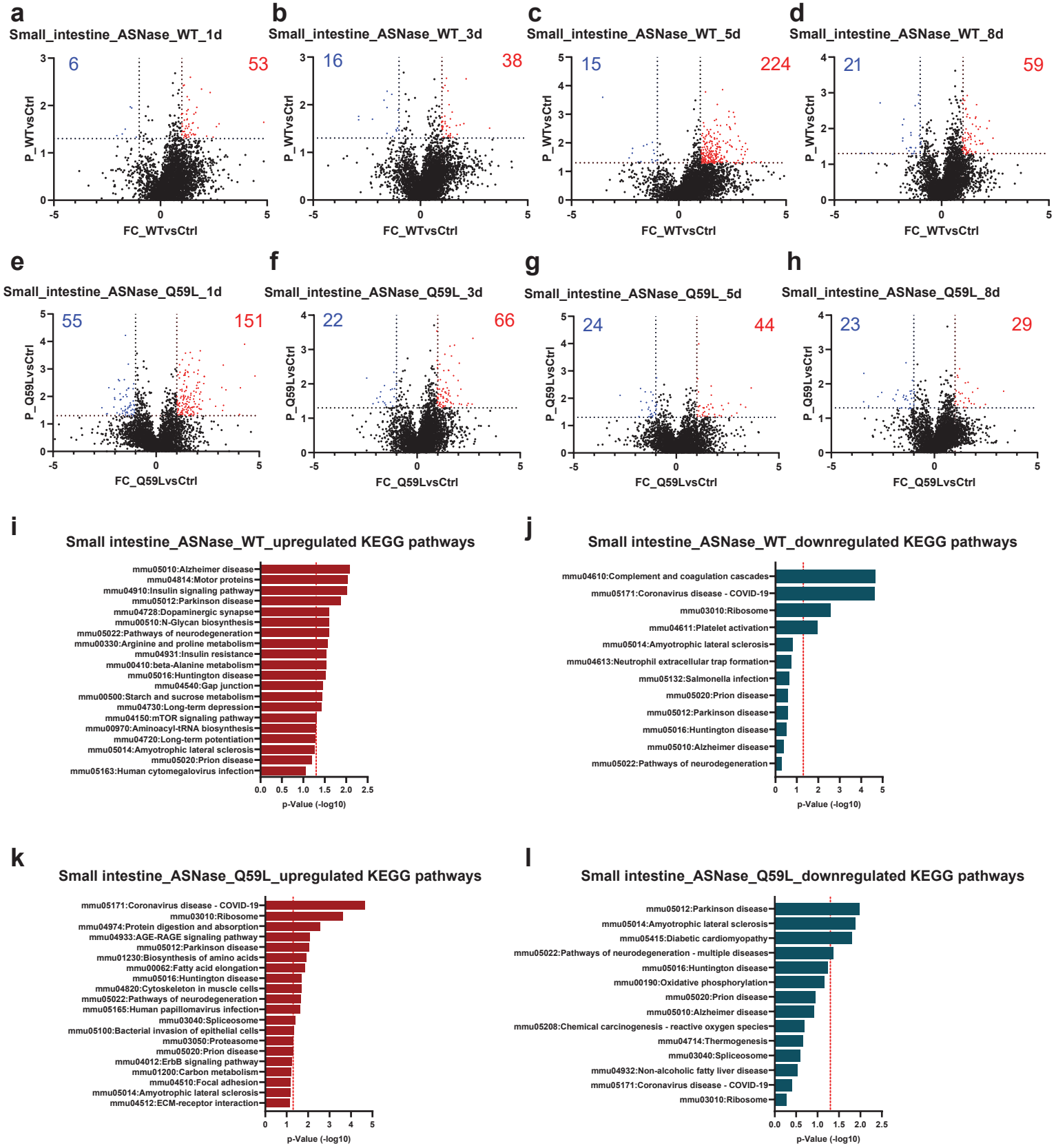

Supplementary Figure 11

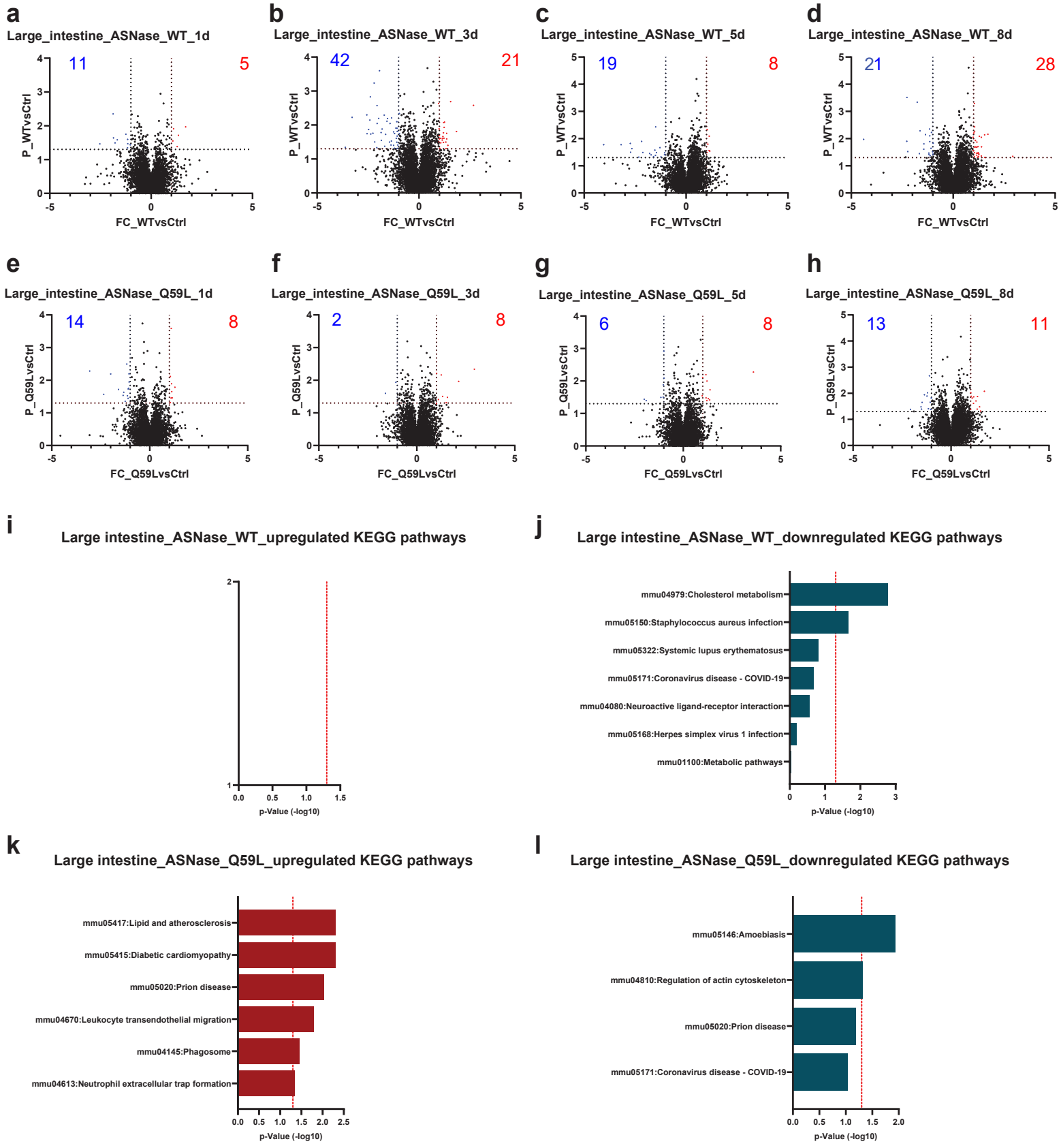

Supplementary Figure 12

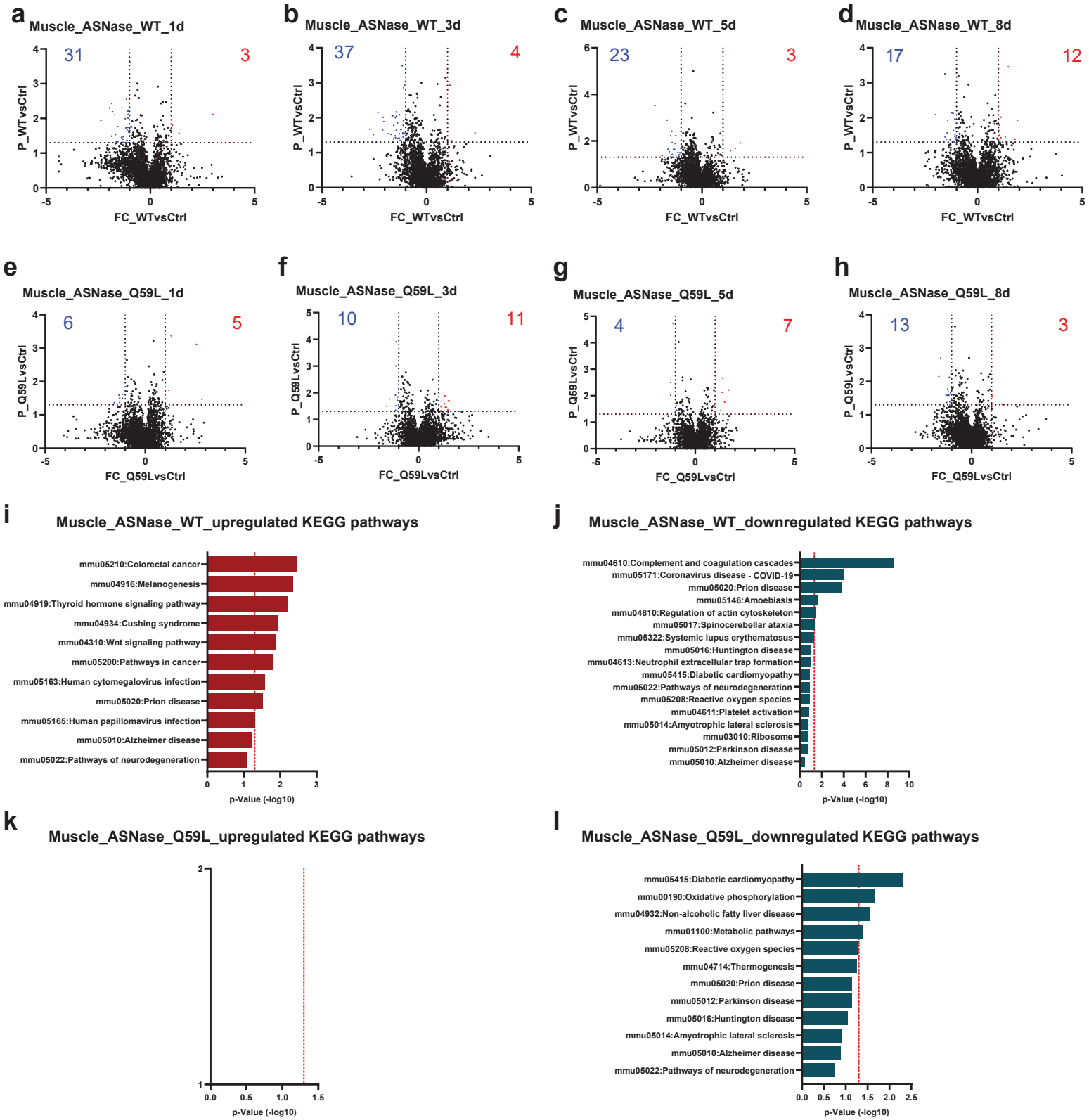

Supplementary Figure 13

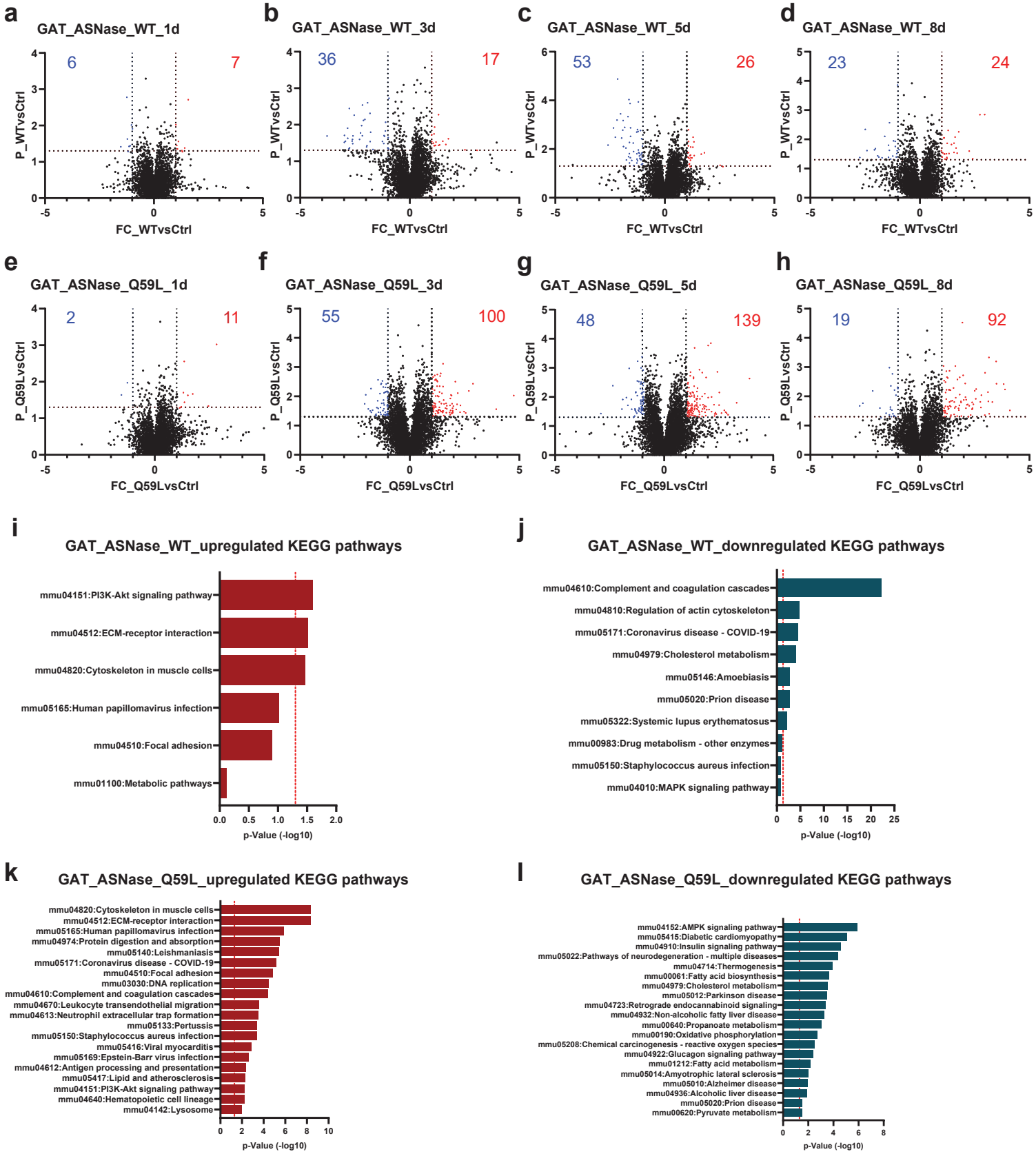

Supplementary Figure 14

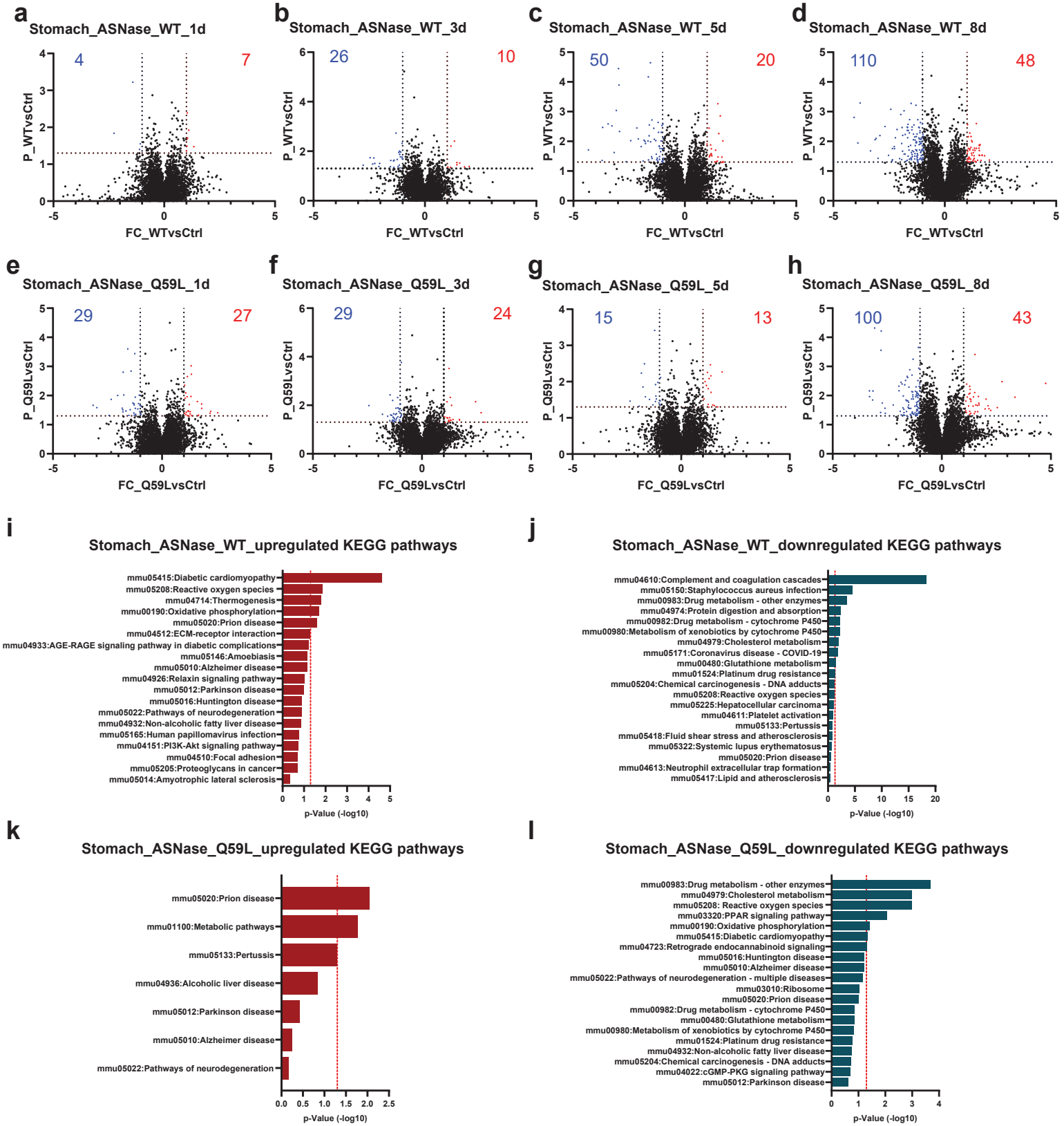

Supplementary Figure 15

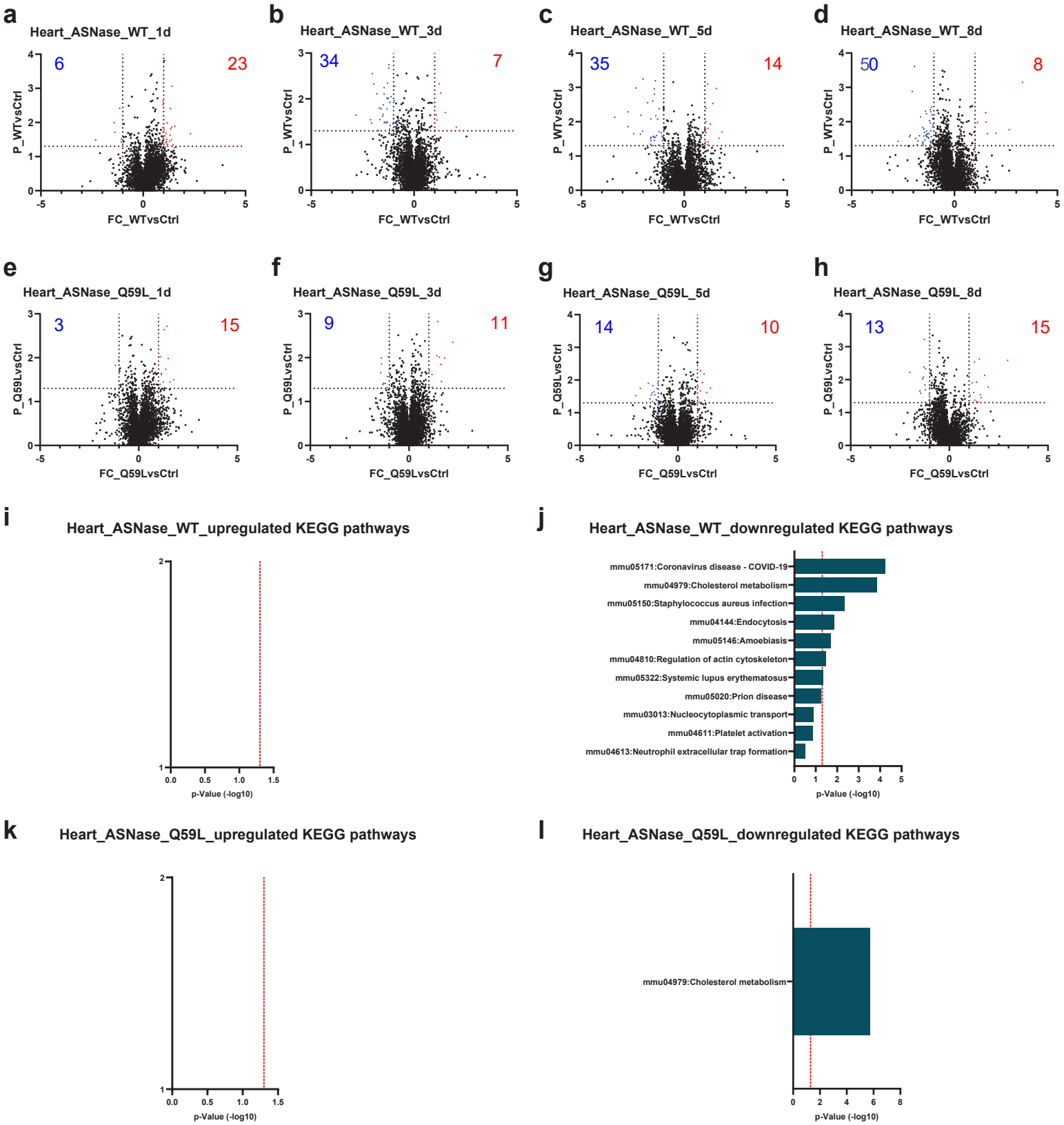

Supplementary Figure 16

a

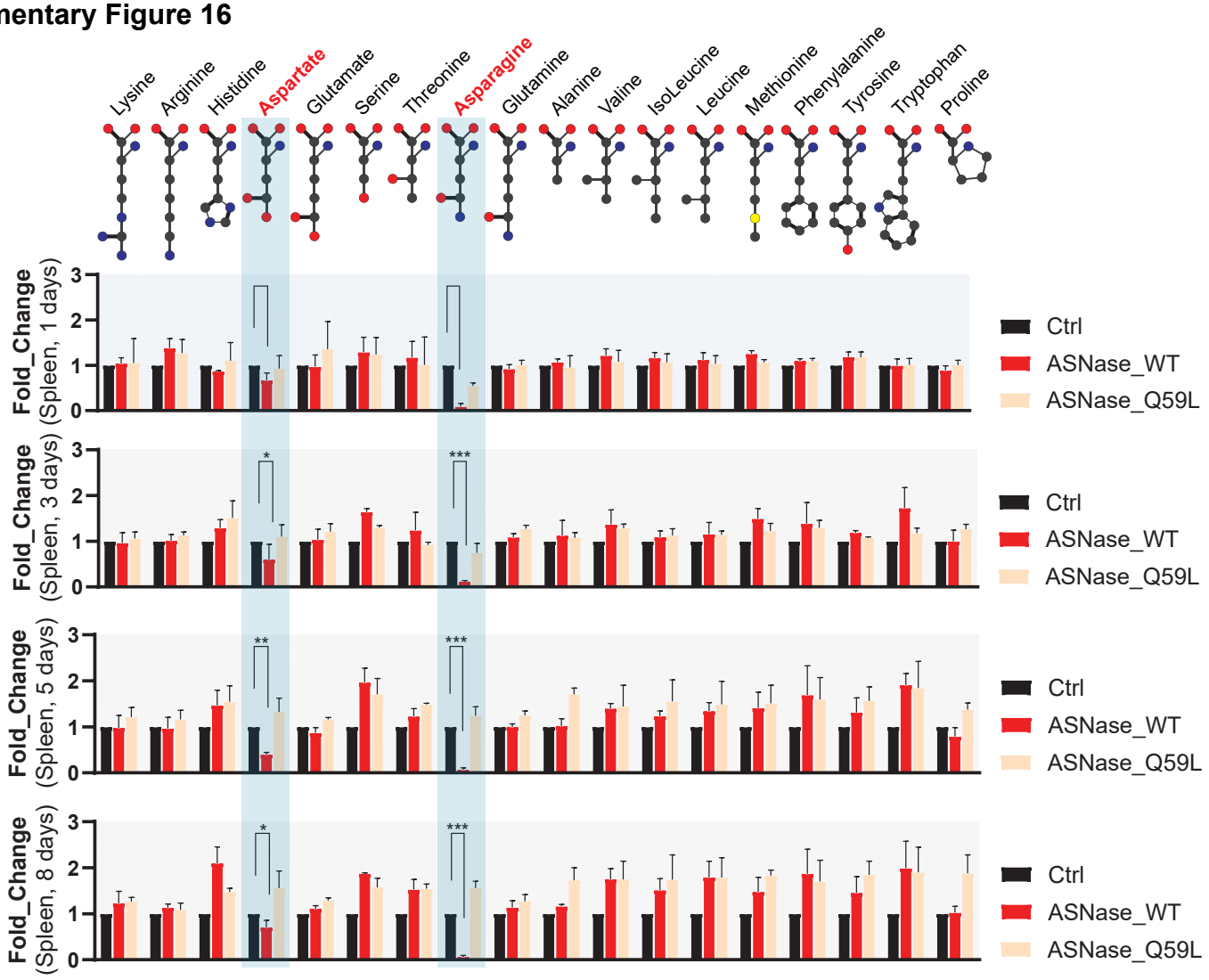

b

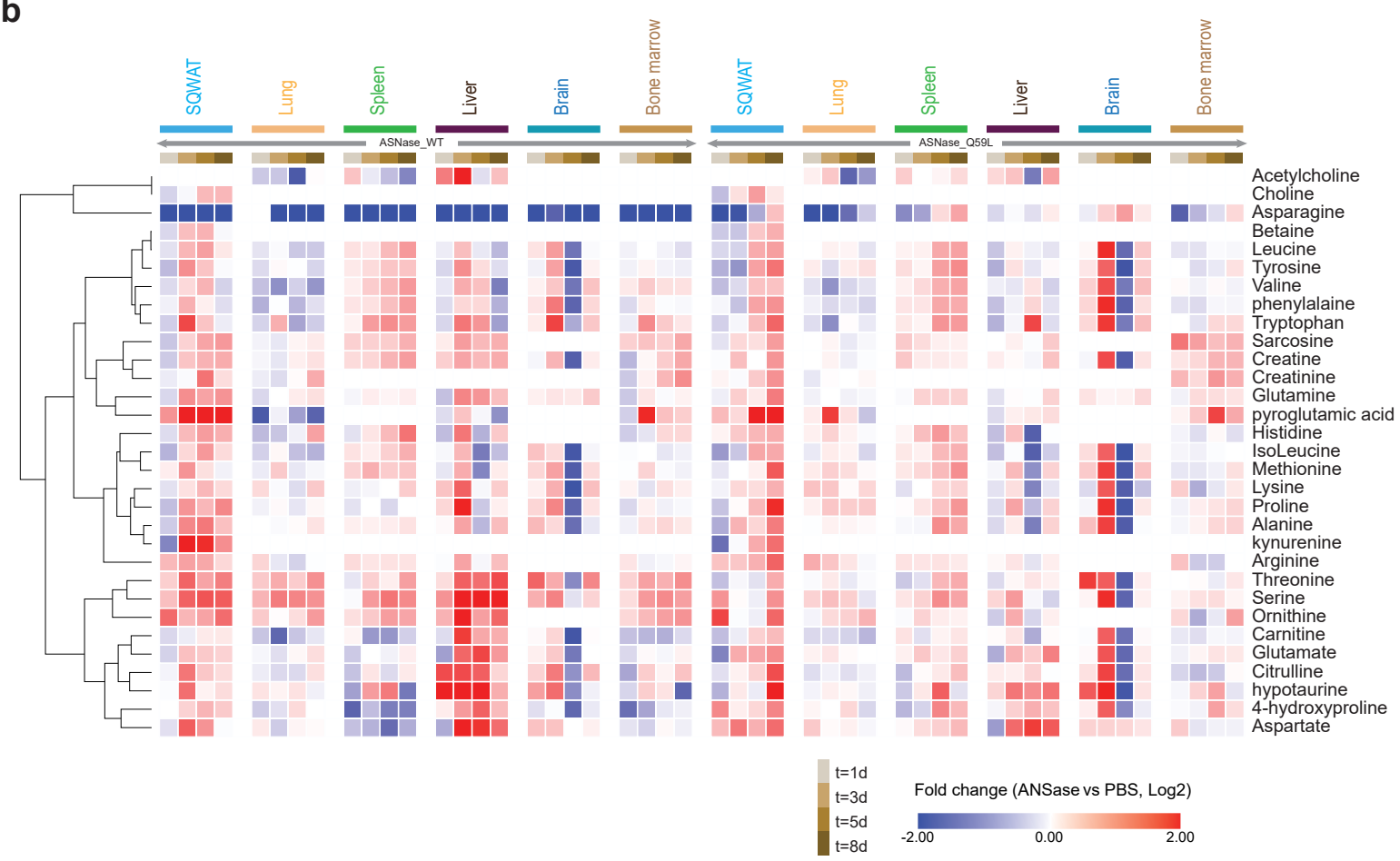

Supplementary Fig. 17

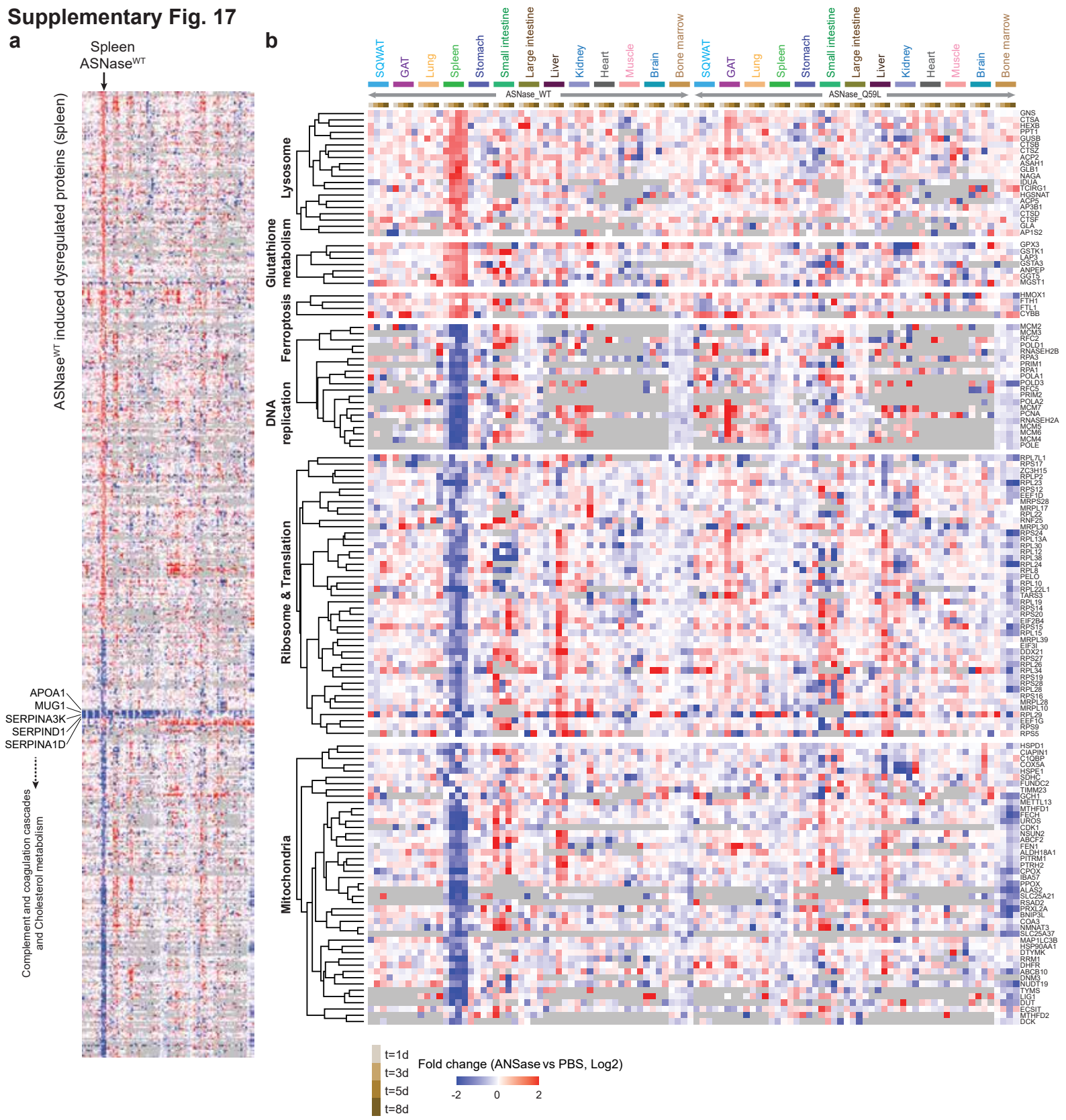

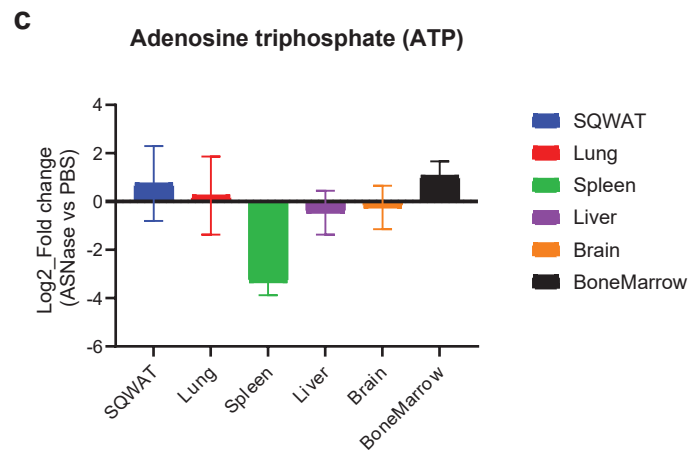

Supplementary Figure 18

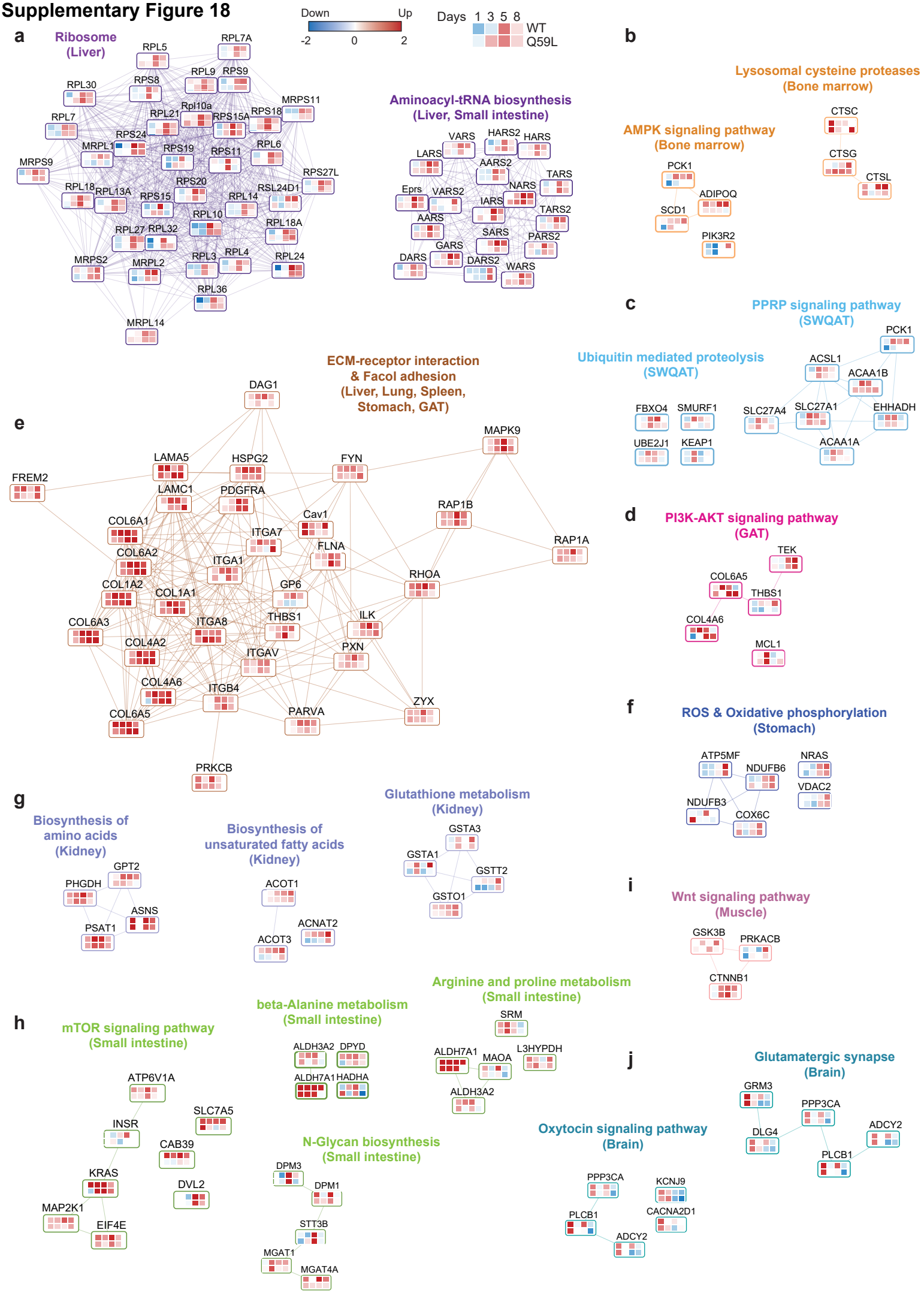

Supplementary Figure 19
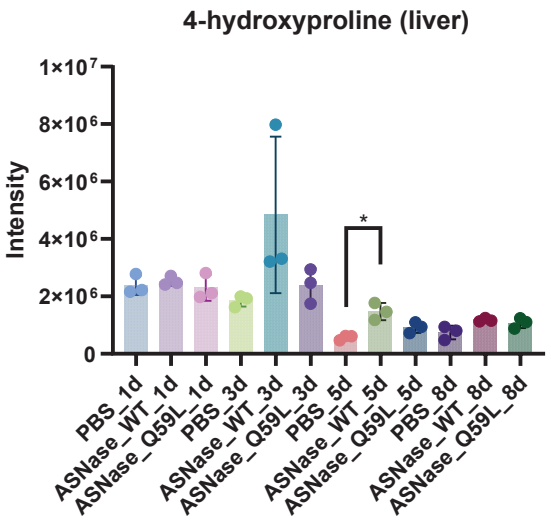
a